Andreas Steinegger, BSc

Thermally Activated Delayed Fluorescence Dyes as New Indicators for Optical Sensors

MASTER'S THESIS

to achieve the university degree of

Master of Science

Master's degree programme: Chemistry

submitted to

Graz University of Technology

Supervisor

Ass. Prof. kand. Sergey Borisov

Institute of Analytical Chemistry and Food Chemistry

Graz, November, 2016

Abstract

In this work a series of dyes of two classes of purely organic TADF emitters (bis-(diarylamino)-anthraquinones and tetracarbazolyl dicyanobenzenes), known from OLED industry, with varying photophysical properties was synthesized. The obtained dyes were thoroughly characterized for their applicability for optical sensing. The dyes were immobilized into polystyrene and the resulting sensor foils were investigated for their suitability for oxygen sensing. The sensors display good oxygen sensitivity, but are poorly suitable for oxygen sensing due to their high temperature cross sensitivity. Incorporated into an oxygen impermeable poly(vinylidene chloride-*co*-acrylonitrile) matrix, the dyes represent high sensitivity temperature probes with negligible oxygen cross sensitivity and feature characteristics ranking among the most sensitive temperature probes reported.

Kurzfassung

In dieser Arbeit wurde ein Reihe von zwei aus der OLED Branche bekannten Klassen an rein organischen TADF Farbstoffen (Bis-(diarylamino)-anthraquinones und Tetracarbazolyl-dicyanobenzene) mit variierenden photophysikalischen Eigenschaften synthetisiert. Die hergestellten Farbstoffe wurden auf ihre Verwendbarkeit für die optische Sensorik charakterisiert. Mit den Farbstoffen wurden Polystyrolsensorfolien hergestellt, die dann auf ihre Eignung zur Sauerstoffbestimmung untersucht wurden. Abgesehen von der erzielten, guten Sauerstoffsensitivität, eignen sich die hergestellten Sensoren nur wenig zur Sauerstoffmessung, weil die untersuchte Temperaturquerempfindlichkeit äußerst hoch ausfiel. Nach der Immobilisierung der Farbstoffe in einer Sauerstoff impermeablen Polymermatrix weisen sie eine hohe Temperatursensitivität mit vernachlässigbarer Sauerstoffquerempfindlichkeit auf. Im Vergleich mit der Literatur, finden sich die hergestellten Sensoren im Bereich der empfindlichsten bisher bekannten Repräsentanten wieder.

AFFIDAVIT

I declare that I have authored this thesis independently, that I have not used other than the declared sources/resources, and that I have explicitly indicated all material which has been quoted either literally or by content from the sources used. The text document uploaded to TUGRAZonline is identical to the present master's thesis.

EIDESSTATTLICHE ERKLÄRUNG

Ich erkläre an Eides statt, dass ich die vorliegende Arbeit selbstständig verfasst, andere als die angegebenen Quellen/Hilfsmittel nicht benutzt, und die den benutzten Quellen wörtlich und inhaltlich entnommenen Stellen als solche kenntlich gemacht habe. Das in TUGRAZonline hochgeladene Textdokument ist mit der vorliegenden Masterarbeit identisch.

Datum/Date   Unterschrift/Signature

Danksagung

An allererster Stelle möchte ich mich bei dir, Ingo, dafür bedanken, dass du mich in deine wundervolle Arbeitsgruppe aufgenommen hast und stets darauf bedacht warst ein gutes Arbeitsklima zu wahren. Seit meinen Anfängen als Oompa Loompa fühle ich mich an deinem Institut richtig wohl.

Sergey, neben meiner Hochachtung vor dir als Wissenschaftler, bin ich dir auch zutiefst dankbar für deine wunderbare, unterstützende Betreuung. Bei jedem Problem kamen von dir unzählige neue Ideen und Lösungsvorschläge, die mir wieder Mut für meine Arbeit machten.

Ganz herzlich möchte ich mich auch bei dir, Roland, bedanken, für das Messen "meiner" Kristallstruktur und deine Hilfestellung bei der NMR-Spektreninterpretation.

Ein großes Dankeschön an die gesamte Arbeitsgruppe, fixe und nicht fixe Besetzung, ihr seid eine geile Gruppe, die ich auch meine Freunde schimpfen möchte.

Meli, Danke, für all die Erfahrungen, die ich bei dir während meiner Bachelorarbeit sammeln durfte und damit auch für das gute Fundament, dass du mir für mein weiteres Studium geschaffen hast.

Stefan, bei dir muss ich mich für das lehrreichste Labor während meines Masterstudiums bedanken und für die fachliche Unterstützung, die du mir seither gibst.

Berni, David, Christoph und Peter, euch möchte ich für eure Unterstützung am Institut danken, für die unzähligen, mehr oder weniger sinnvollen Fragen, die ihr mir beantwortet habt, und vor allem aber, dass ihr mich in Momenten, in denen mich die Motivation verlassen hatte, wieder aufgebaut habt.

Vielen Dank, auch an die jungen Wilden, Irene, Tanja, Nici, Maxi, Philipp, Schuh und Fips (vl. etwas weniger jung), für die schönen Stunden, die ich mit euch im und außerhalb des Labors verbringen durfte.

Ich darf mich auch glücklich schätzen, dass mich einige meiner Freunde von zuhause, Nici, Luise, Nussi und vor allem Lu, auch auf meinem Weg in Graz begleitet haben.

Anna, Beate, Vale, ihr im Besonderen, habt meine Studienzeit versüßt und mit eurer Freundschaft bereichert.

Calciumboy Luki, mit dir möchte weiterhin ein Büro teilen und am Institut alt werden, Danke!

Meinen Eltern und meinen Geschwistern danke ich dafür, dass sie mich bei all meinen Entscheidungen unterstützt haben und mir bewusst gemacht haben, wo im Leben meine Prioritäten liegen.

Milanka, meine Liebespartnerin, wenn ich alles erwähnen würde, für das ich mich bei dir Bedanken möchte, würde das hier den Rahmen sprengen. Danke für alles und schön, dass es dich gibt!

Andreas Steinegger, BSc   Graz, November, 2016

Contents

1 Introduction

In 1961 delayed fluorescence produced from thermal activation is said to be discovered and described for the first time[1] in eosin, a purely organic material, by Parker and Hatchard[2]. F. Perrin, however, observed something what he called "alpha phosphorescence" already in 1924[3] and described "delayed fluorescence" in 1929[4].

Since then not very much attention has been paid to this phenomenon the most remarkable exceptions to be the study of acridine yellow incorporated into a rigid saccharide matrix for optical thermometry[4], the finding of new compound classes exhibiting TADF (Cu(I)-complexes[5], anthraquinones[6], thioketones[7], and etc.), and the use of fullerenes displaying TADF for oxygen and temperature sensing[8, 9].

This has only changed in 2009 when it was first attempted to use TADF materials for the preparation of organic light emitting diodes (OLEDs) by Endo et. al.[10], being the start of a now flourishing research area. However the ongoing research focuses on the application of TADF materials as OLEDs, especially metal-free compounds due to financial and ecological reasons, maybe unjustifiedly neglecting application beyond OLEDs as their suitability for optical sensing, more precisely time-resolved fluorescence microscopy, has been demonstrated as well[11].

In this thesis two different classes of purely organic TADF emitters (carbazole substituted dicyanobenzens[12] and anthraquinone based intramolecular charge-transfer compounds[13]) are examined for their applicability for optical oxygen and temperature sensing, two analytical key parameters in many areas of industry and research, due to their ease of synthesis from commercially available precursors and the simple tunability of their photophysical properties by varying the substituents[13].

2 Theoretical Background

2.1 Luminescence

This chapter is based on references [3, 14–16], others will be cited independently.
The term luminescence refers to the emission of photons during the de-excitation process or so called relaxation of electronically excited states of any substance to a lower lying ground state according to the rules of the MO-theory. An atom or a group of atoms serving as an unit during light emission is called luminophore. The types of luminescence are distinguished according to their mode of excitation (origin of the energy used for excitation) and the nature of the excited state (singlet and triplet state).

2.1.1 Modes of Excitation

Depending on how the excitation of the luminophore from its electronic ground state to its excited states happens, the various types of luminescence are classified:

Photoluminescence: by absorption of light

Radioluminescence: excitation through ionizing radiation such as x-rays, alpha- and beta particles and gamma rays

Cathodoluminescence: excitation through electron beams

Electroluminescence: an electric field provides the energy for excitation

Thermoluminescence: excitation via release of stored energy by heating from a metastable state

Chemiluminescence: generation of an excited species via a chemical reaction

Bioluminescence: generation of an excited species via a biochemical reaction

and other ...

Absorption of Light

Light seen as an electromagnetic wave can be imagined mapping a time dependent electric and magnetic force field into its surrounding about its direction of propagation, having a certain frequency of oscillation. Electrons as charged particles and magnetic dipoles may interact with the mentioned oscillating electric field of light (the magnetic interaction is negligible).

For an interaction between light and the electrons of a molecule to take place, meaning the absorption of a photon by the molecule, these oscillations have to be "on resonance", thus equation 2.1

$$\Delta E = h\nu \tag{2.1}$$

has to be satisfied. ΔE refers to the energy gap between two electronic states, being the initial and final state of the substance, before and after the absorption, h is the Planck constant. ν denotes the frequency of the electromagnetic wave and typically corresponds to light of the UV and Vis region.

Considering polyatomic molecules the transitions (between two electronic states) from an orbital of a molecule in the ground state to an higher lying unoccupied orbital are classified according to the involved orbitals (e.g. $n \to \pi^*$). These transitions vary in their energy corresponding to gap between the energy levels and usually are in the following order:

$$n \to \pi^* < \pi \to \pi^* < n \to \sigma^* < \sigma \to \pi^* < \sigma \to \sigma^*$$

In absorption and fluorescence spectroscopy the transitions of interest are those between the highest occupied molecular orbital (HOMO) and the lowest unoccupied molecular orbital (LUMO), being the transition of smallest energy.

However not all transitions may be "allowed", what actually means that they occur at significantly lower probability, a probability that depends on a measure called transition moment which itself is a product of three factors (actually integrals) or so to say, selection rules:

Spin or multiplicity factor: only transitions between states of the same multiplicity are allowed (singlet-singlet, triplet-triplet). However, depending on the degree of the spin-orbit coupling the wavefunction of the state of a given multiplicity also contains some small part of the wavefunction of the other multiplicity, therefore making spin forbidden transitions possible.

Symmetry factor: depends on the symmetry and the overlap of the given orbitals. Symmetry forbidden transitions can become possible due to effects molecular vibrations on symmetry.

Franck-Condon factor: the overlap integral of the nuclear vibration functions of the two involved states, describing how similar the nuclear vibration functions of the two states are, apart from orthonormal functions never becomes zero.

The intensity of absorption and emission and therefore the oscillator strength, a measure for describing the ability to absorb light considering the molecule as an oscillating dipole, is proportional to the square of this transition moment. The experimental description of the ability of a molecule to absorb light in a given solvent is the molar absorption coefficient ε, which is also connected to the oscillator strength via the integral of the absorption bands. The molar absorption coefficient for a given wavelength can be determined via the absorbance of a sample given that it follows the Beer-Lambert Law 2.2:

$$A(\lambda) = log\frac{I_\lambda^0}{I_\lambda} = \varepsilon(\lambda)lc \tag{2.2}$$

A being the absorbance at a given wavelength, c the concentration of the absorbing species, l the optical path length of the sample, I_λ^0 and I_λ the intensities at a given wavelength of the light beam entering and leaving the sample, respectively.

2.1.2 Franck-Condon Principle

In quantum mechanics the Born-Oppenheimer-Approximation is used to simplify the wavefunction of a molecule by separately looking at the electron and nuclei component. This is possible due to much faster motion of the electrons (e.g. excitation in the magnitude of 10^{-15} s) than the movement of the nuclei (molecular vibrations typically within the range of 10^{-10}- 10^{-12} s), from the perspective of the electrons the nuclei are at least a thousand times slower. Therefore processes of electrons can be assumed with static positions of the nuclei, only introducing a negligible er-
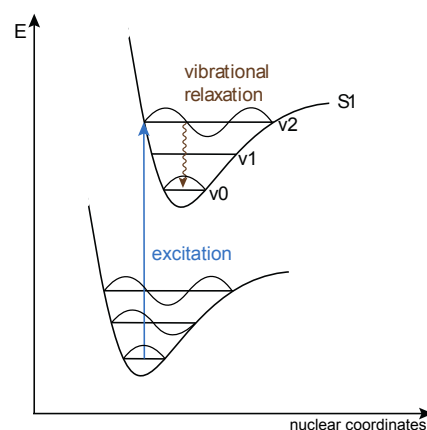

Figure 2.1: A simplified depiction (no potential area) of the electronic states and the corresponding vibrational states as a Morse-Function.

ror.

This is also the basis of the Franck-Condon principle, which assumes that an electronic transition happens without changes in the positions of the nuclei. Considering molecules at room temperature, most of the molecules are in the lowest vibrational level, at equilibrium. Due to the excitation, however, the electron distribution is altered, therefore the potential area depending on the nuclear coordinates is different at given nuclear coordinates as depicted in figure 2.1. This means that the conformation of the molecule in vibrational equilibrium in its electronic ground state does not correspond to the conformation of the molecule in vibrational equilibrium in its electronically excited state.

To sum up, electronic excitation typically occurs from the vibrational ground state in the electronic ground state into a excited vibrational state of the excited electronic state. The finally occupied vibrational state of the excited electronic state depends on the already mentioned Franck-Condon factor. Qualitatively spoken, the finally occupied vibrational state is the one that most resembles the initial vibrational state in term of vibrational wavefunction.

2.1.3 De-excitation processes and pathways

Once in the excited state a molecule or an electron has a variety of possible de-excitation pathways to eventually return to the ground state or being transformed into another species, as depicted in figure 2.2.
A few selected ones, relevant for further discussion are now dealt with in more detail, also illustrated in the Perrin-Jablonski diagram in figure 2.3.
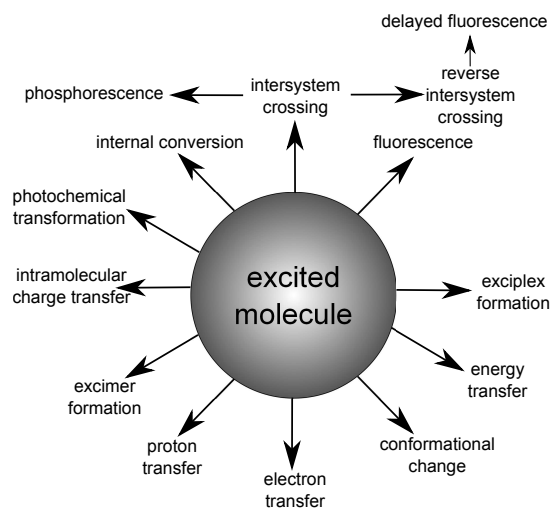

Figure 2.2: The de-excitation pathways possible for an excited molecule.

Internal Conversion (IC)

One of the non-radiative de-excitation pathways is the internal conversion, which is an isoenergetic transition from the vibrational ground state in an electronically excited state to a highly vibrationally excited state of the next lower electronic state(e.g. S_2
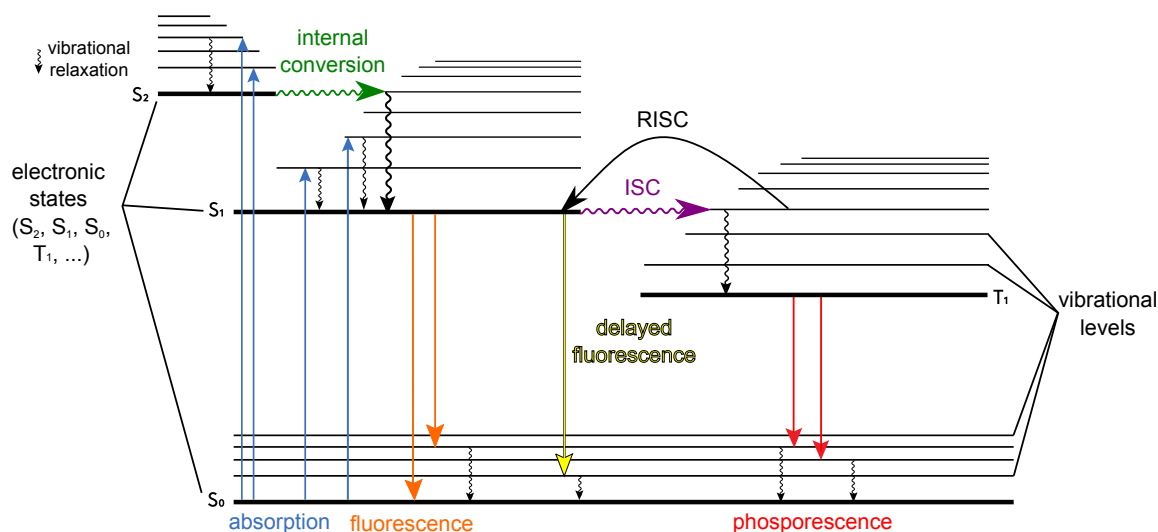
Figure 2.3: The Perrin-Jablonski diagram illustrates the processes that occur in a luminophore between absorption and emission of light.

to S_1, S_1 to S_0) with the same spin multiplicity, depicted in figure 2.4. This internal conversion, usually taking around 10^{-11} to 10^{-9} s, is followed by the vibrational relaxation, meaning the return vibrationally highly excited molecule into its vibrational ground state, with the vibrational relaxation taking 10^{-12} to 10^{-10} s. The efficiency of the internal conversion increases with decreasing energy gap between the two involved electronic states. Therefore starting from S_2 internal conversion is the predominant transition, whereas starting from S_1, due to its much larger energy gap to S_0, internal conversion is competing with fluorescence and intersystem crossing.
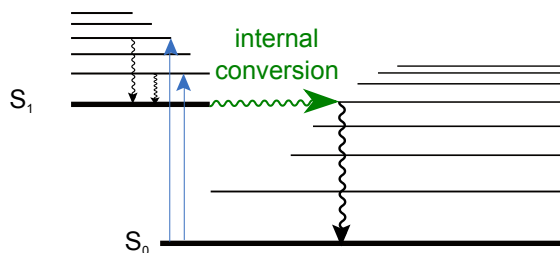
Figure 2.4: The illustration of IC using the Perrin-Jablonski diagram.

Fluorescence

The emission of photons during the transition between two singlet states, apart from a few exceptions generally from the S_1 to the S_0 state, is called fluorescence, depicted as orange lines in figure 2.5. The emission of the photon itself is with 10^{-15} s as fast as the absorption of the photon, however, before the photon is emitted, the molecule

stays a certain time in its excited state (typically 10^{-10}-10^{-7} s), before returning to a more or less vibrationally excited state of the electronic ground state. Due to the vibrational relaxation in S_1 and the transition of the molecule into some, not necessarily the ground vibrational level, there is a reduction of the energy gap between the final and initial states of the transition, therefore a shift of wavelength between the absorbed and emitted photons is observed, the so called Stokes shift. However, it is also possible, that photons higher of energy than the absorbed ones are emitted. This can happen, when a molecule is not in the vibrational ground state before the absorption of a photon, which can happen due to energy distribution according to Boltzmann.
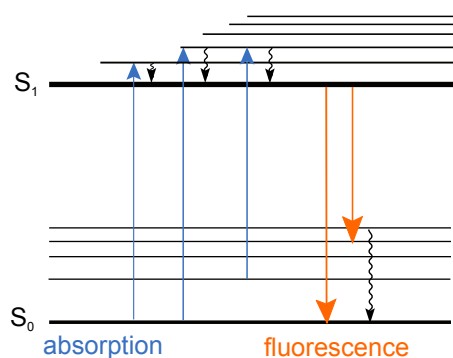

Figure 2.5: The illustration of fluorescence using the Perrin-Jablonski diagram.

Intersystem Crossing (ISC)

Another possibility for a non-radiative transition is the isoenergetic transition between two vibrational levels of different spin multiplicity, namely S_1 and T_1, followed by the vibrational relaxation to the vibrational ground state of T_1, as depicted in figure 2.6. This is always only an intermediate step during de-excitation, as it does not return the molecule into its electronic ground state. As mentioned before intersystem crossing can compete with other de-excitation pathways from S_1 as with a time scale from 10^{-7} to 10^{-9} s is similiarly fast fluorescence and IC. Principially this transition is forbidden, as it results in a reversal of spin of the excited electron, but it is rendered possible by the fact, that the actual wavefunction of the singlet state, also contains some small part of a triplet wavefunction due to spin-orbit coupling. An increasing spin-orbit coupling, for example through heavy atoms, increases the probability for ISC.

Phosphorescence

After ISC has produced a molecule in the excited triplet state, a radiative de-excitation process accompanied by a spin reversal called phosphorescence can happen, as illustrated
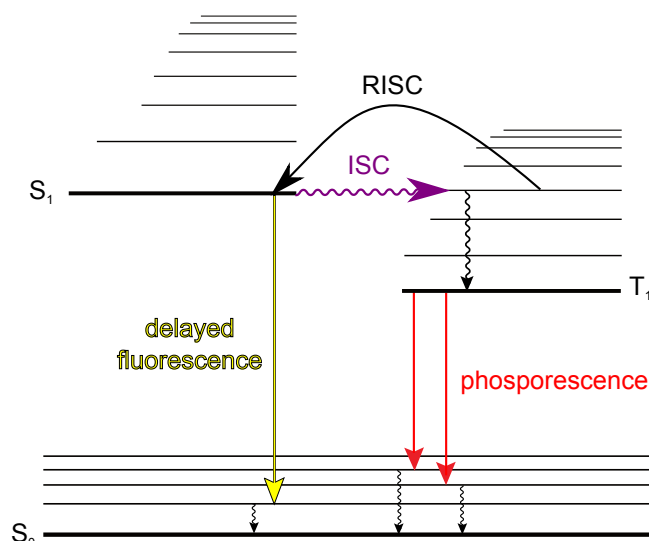
Figure 2.6: The illustration of ISC and subsequent processes using the Perrin-Jablonski diagram.

in figure 2.6. Again, this transition is spin forbidden, but is rendered possible due to spin orbit coupling. The emitted photons of this process are of even lower energy, as the triplet state is lower in energy than the singlet state, therefore phosphorescence bands are shifted to longer wavelengths. However, phosphorescence is competing with reverse intersystem crossing and intersystem crossing with subsequent vibrational relaxation, both of which are favoured by increasing temperature and in solution. On the contrary phosphorescence is favoured by low temperatures and rigid media, reducing the amount of collisions favouring ISC. The emission of a photon is again fast with a time scale of 10^{-15}, however in phosphorescence the time the molecule stays in the triplet state is much longer, with lifetimes from 10^{-6} up to minutes at low temperatures.

Reverse Intersystem Crossing (RISC) and Delayed Fluorescence

As depicted in figure 2.6 a molecule in the excited triplet T_1 state can return to the excited singlet state S_1 via thermal activation. Provided that, the energy gap between these two states is small enough, sufficient thermal energy is provided and the lifetime of triplet state is long enough. Therefore this transition is highly temperature dependent. Returned to the S_1 state, the molecule has all options for further processes, such as IC or fluorescence.

The fluorescence occurring after RISC is called delayed fluorescence as its characteristics apart from its spectral properties differ from previously described fluorescence, having, caused by the RISC, a high temperature dependency and a much prolonged lifetime. To specify, this type of de-excitation process is called thermally activated delayed fluorescence

(TADF) or E-type delayed fluorescence, as it was first discovered in eosin.

However there is also a second type of delayed fluorescence called P-type after the molecule pyrene, where this process was observed the first time. In contrast to TADF, P-type delayed fluorescence is not the subsequent process to RISC, but to a process referred to as triplet-triplet annihilation (TTA).

TTA can occur in concentrated solutions, when the collision of two molecules in the T_1 state provides enough energy for one of them to return into the S_1 state, the other one returns to the ground state S_0. This process again leads to delayed fluorescence, but with different characteristics from TADF, as it has a quadratic dependence with excitation light intensity and a decay time constant half the lifetime of the triplet state in dilute solution.

2.1.4 Lifetimes

After promotion to an excited state by a short pulse of light a molecule has different options for de-excitation, generally radiative and non-radiative processes. Radiative transitions, however, do not occur immediately after the molecule reached the excited state, but it stays some time in this state, the lifetime being a measure for this time span. The kinetics of de-excitation processes are described by simple first order kinetics 2.3:

$$-\frac{d[A^*]}{dt} = (k_r + k_{nr})[A^*] \tag{2.3}$$

where $[A^*]$ is the concentration of molecules in the excited state, k_r and k_{nr} are the rate constants for radiate and non-radiative deactivation respectively. k_{nr} is consisting of k_{IC} and k_{ISC} for intersystem crossing. Integration over dt and $[A^*]_0$ being the concentration of excited molecules at time 0 leads to following equation 2.4:

$$[A^*] = [A^*]_0 exp(\frac{t}{\tau}) \tag{2.4}$$

where instead of the rate constants the lifetime for the excited singlet or triplet state τ is used and given by equation 2.5:

$$\tau = \frac{1}{k_r + k_{nr}} \tag{2.5}$$

The measured fluorescence or phosphorescence intensity at any given time is now proportional to the corresponding concentration of molecules in the excited state given by 2.4. Considering this equation, it can be seen, that the luminescence intensity decreases

according to a single exponential function and that the lifetime corresponds to the time span it takes for intensity to decrease to $\frac{1}{e}$ of the initial value, in other words, for 63% ($1-\frac{1}{e}$) of the molecules to de-excite.

2.1.5 Quantum Yields

As mentioned before, in the excited state the various de-excitation processes for the molecule to take are competing. The share of each process now depends on the ratio of the rate constant of the monitored process to the sum of rate constants of all occurring processes and is called quantum yield for a given process. In other words, the quantum yield for a process is the fraction of excited molecules that take this certain process during their de-excitation pathway as given by equation , e.g. for fluorescence this is the ratio of emitted photons to absorbed photons.

$$\Phi_F = \frac{k_r^S}{k_r^S + k_{nr}^S} = k_r^S \tau_S \tag{2.6}$$

$$\Phi_{ISC} = \frac{k_{ISC}}{k_r^S + k_{nr}^S} = k_{ISC} \tau_S \tag{2.7}$$

$$\Phi_P = \frac{k_r^T}{k_r^T + k_{nr}^T} \Phi_{ISC} \tag{2.8}$$

Quantum yields are affected by interactions with other molecules, such as formation of ground-state complexes or collisional quenching, and other parameters like: temperature, pH, polarity, viscosity and hydrogen bonding, often with parameter mutually influencing each other. Non-radiative processes related to thermal agitation, like collisions, vibrations and rotations, become more efficient with rising temperature as thermal agitation increases.

2.1.6 Luminescence Quenching

The decrease in luminescence intensity by various intermolecular photophysical processes is called quenching. Some of these processes being responsible for quenching are collision with either a heavy atom or a paramagnetic species, electron transfer, proton transfer, energy transfer and excimer or exciplex formation. During these processes the excited molecules are not permanently, chemically altered, but just de-excited. The molecule involved in the de-excitation of the excited molecule M* is called quencher Q and also can be the molecule itsself, through formation of excimers (excited dimers).

A more general approach, depicted in figure 2.7 divides the quenching processes in those decreasing luminescence by preventing the formation of an excited molecule that can luminesce, called static quenching and in those where a collision is involved in the de-excitation of the excited molecule (dynamic quenching).
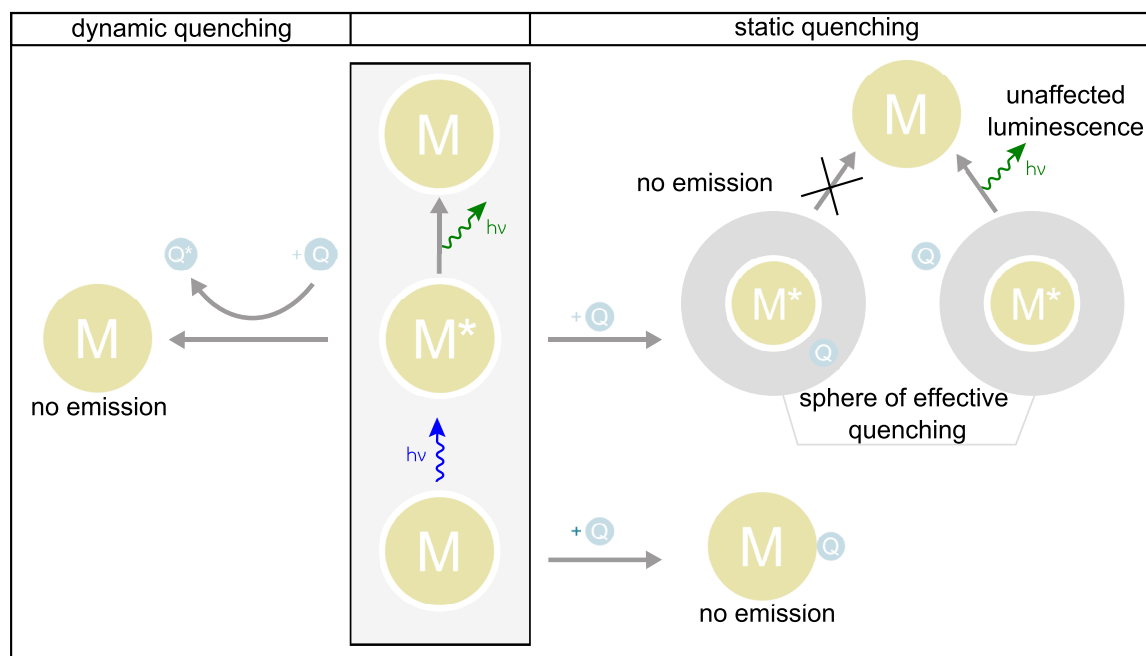

Figure 2.7: Illustration of dynamic and static quenching.

Static Quenching

For static quenching two possible mechanism can be distinguished, either there is a sphere of effective quenching, illustrated in the upper right part of figure 2.7 or the quencher forms a ground-state non-fluorescent complex, depicted in the lower right part of figure 2.7. Considering a luminophore in its excited state and a quencher in viscous media or rigid matrices, Perrin proposed a model, in which luminescence is quenched by the quencher if it is inside a certain active sphere of the excited molecule. Outside the effective quenching sphere the quencher has no effect on the luminescence. Unlike the later mentioned Stern-Volmer equation, there is no linear relationship between the ratio of intensities I_0/I (I_0 Intensity withouth quencher, I Intensity at given quencher concentration) and the quencher concentration.

The other possibility is the formation of a non-fluorescent complex of the molecule in its ground state and the quencher according to given equilibrium:

$$M + Q \rightleftharpoons MQ$$
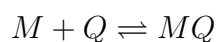
As the molecule in its excited state is not effected, this type of quenching has no influence on the excited-state lifetime. A quantitative description for the luminescence intensites depending on the quencher concentration is here given by a relationship similar to the Stern-Volmer equation:

$$\frac{I_0}{I} = 1 + K_S[Q] \tag{2.9}$$

K_S being the stability constant for the quencher-luminophore complex, I_0/I the ratio of intensities without and with a given quencher concentration, respectively and $[Q]$ the quencher concentration.

Dynamic Quenching

In the case of collisional quenching the luminophore in its excited state is de-excited to the ground state by a diffusive encounter with the quenching molecule, depicted in the left half of figure 2.7. During the excited lifetime mutual approach of the excited molecule and the quencher is possible and can lead to a collision causing de-excitation, provided that the lifetime is long enough and the surrounding media is not too viscous. This process is therefore diffusion controlled. In contrast to static quenching, dynamic quenching has both an influence on luminescence intensity and lifetime. The commonly used description for dynamic quenching is given by the Stern-Volmer relation:

$$\frac{\Phi_0}{\Phi} = \frac{I_0}{I} = 1 + k_q \tau_0[Q] = 1 + K_{SV}[Q] \tag{2.10}$$

with k_q being the quenching rate constant and K_{SV} the Stern-Volmer constant.

In microheterogeneous systems that do not possess a single exponential decay a downward curvature is often introduced into the Stern-Volmer-Plot (I_0/I vs. [Q]). These microheterogeneous system often occur after the incorporation of the luminophore into polymer matrices. For these conditions a modified Stern-Volmer relation was developed practicable for decay curves with up to 4 exponentials[17]. However, usually the relation is used with two exponentials, then being called two-site model, assuming two different environments for the luminophore with unlike quenching characteristics, given by:

$$\frac{I}{I_0} = \frac{f}{1 + K_{SV}^1[Q]} + \frac{1 - f}{1 + K_{SV}^2[Q]} \tag{2.11}$$

where K_{SV}^1 and K_{SV}^2 are Stern-Volmer constants for the two sites. Although involving some simplifications, the model generally gives valid results for luminophores incorporated into polymers[17].

2.2 Optical Oxygen Sensors

Optical oxygen sensors are chemical sensors using transduction (the conversion of information into an useful analytical signal[18]) based on optical phenomena, which result from the interaction of an analyte with a receptor part. The term chemical sensor refers to a miniuarized device that is capable of reversibly and continuously measuring the concentration of a specific analyte. The device typically consists of two characteristic components, a receptor, responsible for recognition, and a transducer part[18, 19]. The optical phenomena that can be used are: absorbance, reflectance, luminescence, refractive index, optothermal effect and light scattering[19]. In the subsequent discussion only luminescence-based oxygen sensors are treated.

2.2.1 Principles

The sensing of oxygen is based on the quenching of luminescence of an indicator dye, as depicted in figure 2.8. The dye is usually incorporated into an oxygen-permeable polymer matrix. The ground state of molecular oxygen is a triplet state, but can be brought into one of two low lying singlet states via energy transfer during a collision from an excited luminophore in the singlet or triplet state, which itself returns to the ground state. This process was already mentioned as collisional or dynamic quenching and is diffusion-limited, resulting in a decrease of luminescence lifetime and intensity. The sensitivity towards quenching by oxygen can be attributed to two parameters, the lifetime of the luminophore (the longer, the more time molecular oxygen has to collide with the excited luminophore) and the oxygen permeability of the polymer matrix, cf. table 2.1, it is incorporated into.
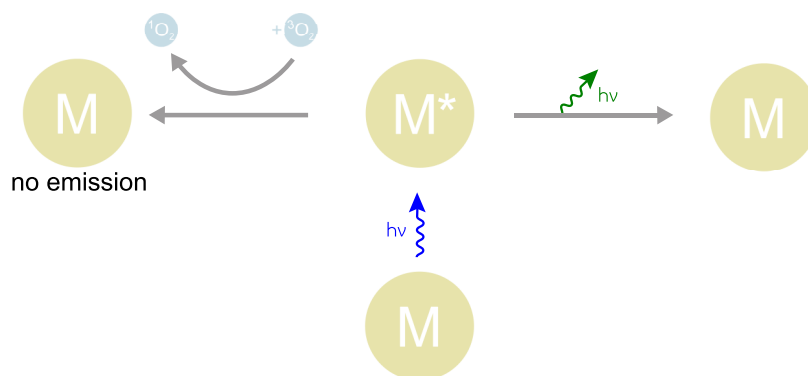

Figure 2.8: Illustration of dynamic quenching by molecular oxygen.

Table 2.1: Oxygen permeabilities, given via the permeability coefficient P, of polymers used in oxygen sensing and others[20].

Polymer	P x 10^{13} $[\frac{cm^3(STP)*cm}{cm^2sPa}]$
Cellulose acetate	0.585
Cellulose acetobutyrate	3.56
Ethylcellulose	11
Poly(dimethylsiloxane)	695
Poly(methylmethaacrylate)	0.116
Poly(vinyl chloride)	0.034
Polystyrene	2
Polytetrafluorethylene	3.2
PE HDPE	0.3
PE LDPE	2.2
Poly(vinylidenchloride)	0.00383
Polyacrylonitrile	0.00015

2.2.2 Sensing Methodologies

As luminescence intensity and lifetime are affected by oxygen quenching, several options exist on how to measure the oxygen concentration. The most direct, but also most vulnerable method is the direct measurement of the luminescence intensity. Dye concentration, photobleaching, scattering, fluctuations in light source intensity and others[21], are influencing the measurement, therefore resulting in a less reliable method.

Methods eliminating some of these problems, are based on ratiometric measurements, where a second dye, unqenchable by oxygen, with a distinct emission spectrum, is incorporated into the same matrix. Instead of the sole measurement of the luminescence intensity of a dye, the ratio of intensities of the two dyes is determined. Nevertheless drifts due to leaching and photobleaching are not compensated for.

The other property affected by oxygen, the luminescence lifetime, can be measured either in time domain or in frequency domain, but both do not suffer from the major drawbacks of the intensity based methods. Using the time domain method, the luminophore is excited with pulse of light and then the time dependent decay is measured. The lifetime can now be calculated from the received decay.
The other variant is based on exciting the luminophore with a intensity modulated light, called frequency domain method, causing an also intensity modulated luminescence, but which has as certain delay in time relative to the excitation. This delay can be measured

as a phase shift ϕ, as illustrated in figure 2.9, and can be used to determine the lifetime τ via equation 2.12:

$$\tau = \frac{tan\varphi}{2\pi f} \tag{2.12}$$

with f being the modulation frequency of the exciting light.
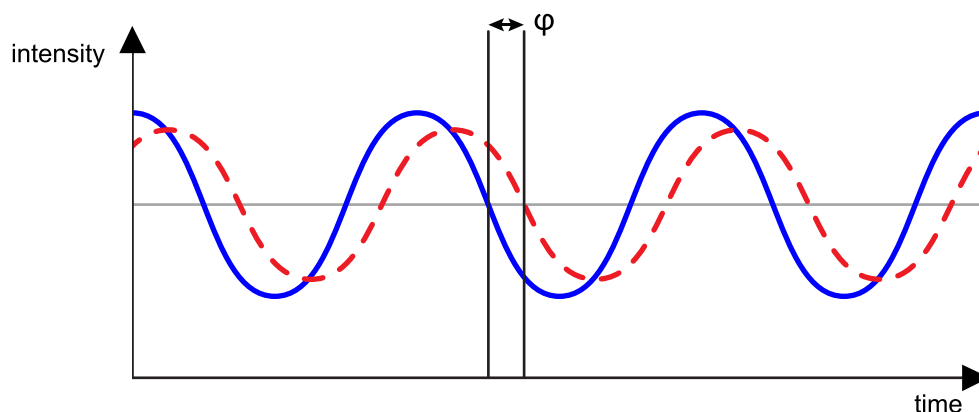

Figure 2.9: Illustration of the phase shift recieved in the frequency domain method.

2.2.3 Luminescence-based Indicators

Luminescence based oxygen sensors are to date the most prevalent sensors used[21] and the first work was done by Kautsky and Hirsch already in the early 1930's[22]. Since then a large number of indicators has been synthesized. Many lost its importance (e.g. polycyclic aromatic hydrocarbons) due to the development of more advanced indicators, but two groups of dyes have been of enduring popularity, transition metal polypyridyl complexes and metalloporphyrins. The latter being the most popular group of indicators[21, 23].
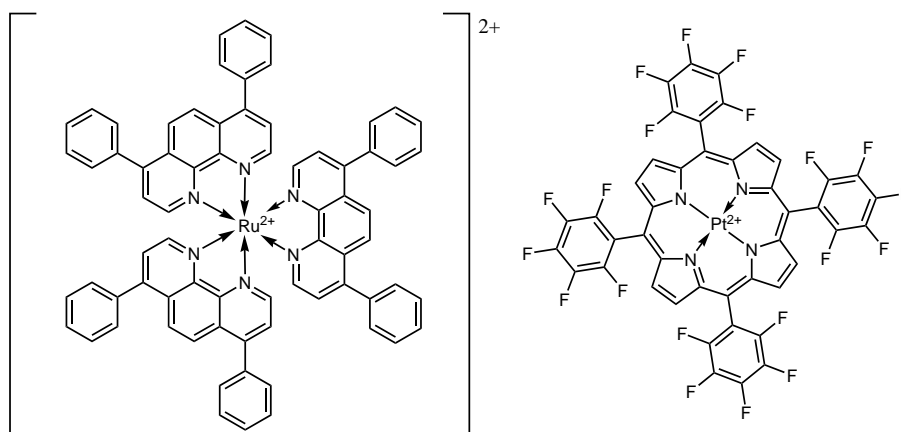
Figure 2.10: Two representatives, $[Ru(dpp)_3]^{2+}$ and PtTFPP, for trans metal polypyridyl complexes and metalloporphyrins, respectively.

Transition Metal Polypyridyl Complexes

The transition metal polypyridyl complexes, usually Ru(II) and Os(II) are used, are in general characterised by a large Stoke's shift, rather short lifetimes, mediocre molar absorption coefficients, good photostability and suffer from considerable thermal quenching. Although these characteristics are merely average, their ease of preparation made them quite popular[21, 23]. One representative with above-average characteristics is [Ru(dpp)$_3$]$^{2+}$, depicted in figure 2.10, possessing a comparatively long lifetime (6.4 µs) and relatively high brightness (Φ=0.3)[21].

Metalloporphyrins

Metalloporphyrins are generally used with Pt(II) and Pd(II) as central atoms, characterised by strong phosphorescence at room temperature, a large Stoke's shift and high molar absorption coefficients[21]. The inherently long lifetime of these complexes can be tuned over a wide range from micro to milliseconds by using the appropriate central atom, Pt(II) for the µs range and Pd(II) for the ms range, and via variation of the substitution. Prominent representatives for this group are platinum tetrakis(pentafluorophenyl)porphyrin (PtTFPP), with its structure shown in 2.10 and platinum tetraphenyltetrabenzoporphyrin (PtTPTBP) as an NIR oxygen indicator[21], with its structure shown in figure 2.11.
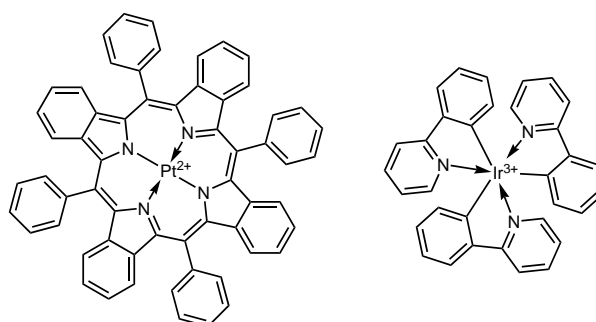
Figure 2.11: Structures of PtTPTBP and [Ir(ppy)$_3$], respectively.

Cyclometallated Complexes

Another class of indicators are cyclometalled Ir(III) and Pt(II) complexes, with a representative structure, nameley of [Ir(ppy)$_3$], shown in figure 2.11. These complexes have large Stokes' shift, are quite photostable and possess a high quantum yield. However in contrast to the metalloporphyrins, lack high molar absorption coefficients[21]. This drawback has been overcome by the cyclometallation of iridium with coumarins, showing more efficent absorption and strong phosporescence[21].

2.3 Optical Temperature Sensors

Optical temperature sensors are among a variety of methods or principles to measure temperature, a diversity that emphasises the importance of this key parameter in all kinds of science. To visualise this, a few types of thermometers shall be mentioned, like liquid-in-glass thermometers based on the thermal expansion, thermometer using the expansion of solids (dilatation and bimetallic thermometers), manometric thermometers (measuring pressure as a function of temperature, e.g. vapour pressure, constant volume of gas), thermoelectric thermometers based on the Seebeck effect, resistance thermometers based upon the dependance of the resistance of a metal conductor upon temperature or the thermometers based on the strong temperature dependent behaviour of seminconductors (e.g. thermistors[NTC, PTC type])[24].

Depending on the desired application each method has it advantages and drawbacks, but most of them lack the possibility to be miniaturized (with a few remarkable exceptions, e.g. thermocouple for intracellular measurement[25] and carbon nano tube based nanothermometers[26]), being suitable for a measurement with spatial resolution smaller than 10 µm[27]. This is no issue for optical sensing based on luminescence being able to be incorporated into the sample to be studied and enabling even imaging in cells[27–29]. General requirements for temperature probes are good sensitivity, low spectral interferences with intrinsic color or fluorescence of samples, good photostability, and high brightness[27]. Below optical temperature sensors based on luminescence will be discussed in more detail.

2.3.1 Principles

Generally all luminophores and luminescent material exhibit temperature dependent emission characteristics[27]. This can be attributed to increasing efficiency of non-radiative de-excitation pathways and increasing thermal agitation. The collisions with surrounding molecules provide additional energy for transitions and at the same time provide an energy sink for energy to dissipate. Non-radiative transitions occur, when vibrational levels of different electronic states overlap or with the concept of potential energy surfaces (the energy of a system depicted as a function of its nuclear coordinates), can occur at intersections of the potential energy surfaces of the two electronic states[16, 30]. Through thermal energy the electrons within the excited states are excited to vibrational levels that fit for these transitions[27]. Empirically the rate constant for these transitions seems to be composed of two parts, one temperature independent, attributed to the zero point motion, the other can be imagined as a part for the transitions that require an activation

energy[16]. Therefore the rate constant for non-radiative transitions is related to the temperature via the Arrhenius equation[27]:

$$k_{nr} \sim e^{\frac{-\Delta E}{kT}} \tag{2.13}$$

with ΔE being the energy difference between the vibrational ground state of the excited state and the overlap point to a possible non-radiative decay state and k, the Boltzmann constant.

As k_{nr} is present in equations 2.5 and 2.6, it has influence both on luminescence lifetime and quantum yield, respectively.

2.3.2 Sensing Methodologies

The sensing methodologies for temperature sensors are analogous to those for oxygen sensors, but with the measurement of anisotropy, an additional method is possible. As mentioned before, the transition moment characterises the transition between an initial and a final state. It can be imagined as a transient dipole resulting from the displacement of electron density during the transition, and may be drawn as an vector[3]. The absorption of (polarized) light now depends on this vector, if its parallel to the eletric vector of the incident light, absorption is likely to occur. The probability of the absorption is proportional to the square of the scalar product of the two vectors, being maximum when they are parallel, decreasing to zero if they are perpendicular[3]. The same is true for emission, therefore, when excited with polarized light, also polarized light is emitted. The luminophores in solution, however, now rotate during the lifetime of their excited state, with rotation increasing with rising temperature. Due to the rotation, the luminophore will lose emission light intensity of its initial polarization, resulting in a temperature dependent measure called anisotropy r, given by equation 2.14, which is normalized by the total intensity[27].

$$r = \frac{I_{\parallel} - I_{\perp}}{I_{\parallel} + 2I_{\perp}} \tag{2.14}$$

where $I_{\parallel}$ and $I_{\perp}$ are the intensities with the emission polarizer being parallel or perpendicular to the polarization of the incident light.

2.3.3 Molecular Probes

The category of luminescent molecular probes can be classified into organic compounds, metal-ligand complexes and lanthanide complex based probes[27].

Organic Compounds

The emission characteristics of luminophores always depend on temperature to some extent, however, only a few display desirable properties or have been characterised for their qualities as temperature indicators.

Rhodamine and derivatives, a representative structure in figure 2.12 on the left, displaying high brightness and good temperature dependency of their fluorescence from 273 to 373 K. They have been used in microfluidics, placed in cells and used for preparation of planar sensor foils[27, 31]. A dye having a different sensing principle is dipyren-1-yl(2,4,6-triisopropylphenyl)borane (figure 2.12, right structure), which upon rising temperature shows luminescence colorimetric change that is due to a shift of the thermal equilibrium between a local excited state and a twisted intramolecular charge transfer state[32]. Also delayed fluorescence can be used for optical thermometry as shown by Fister *et al.*[4], who incorporated acridine yellow (figure 2.12, middle structure) in to a rigid saccharide glass and studied its temperature dependent properties looking at the triplet state lifetime and the intensity ratio of TADF and phosphorescence. By incorporation of C_{70} fullerene into polymer films with perylene as internal reference an optical thermometer also based on TADF could be developed by Baleizão *et al.*[9].
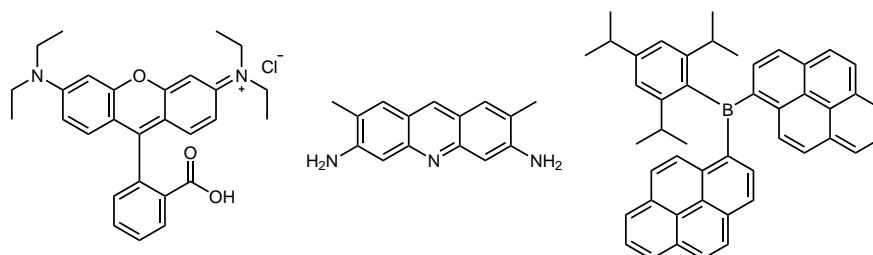
Figure 2.12: Structures of Rhodamine B, acridine yellow and dipyren-1-yl-(2,4,6-triisopropylphenyl)-borane, respectively.

Metal-ligand Complexes

The group of metal-ligand complexes is often subject to oxygen quenching due to their long lifetimes, various groups of oxygen indicators are also used as temperature probes. This cross sensitivity is overcome by incorporating the dyes in polymers with low oxygen permeability, cf. table 2.1.

The group of polypyridyl complexes incorporated in polyacrylonitrile or poly(vinyledene chloride-*co*-acrylonitrile) are among the typically used temperature probes[27]. Again usually Ru and also Ir are used as central atoms, with one representative Ir(ppy)$_2$(carbac), structure shown in figure 2.13, of particular high sensitivity and a linear relationship

between both its lifetime and intensity and temperature over a wide range[33]. Similarly cyclometallated platinum complexes and platinum porphyrins, structures in figure 2.13, were investigated for sensing temperature when incorporated into a gas blocking polymer[27].

A large group of temperature sensitive metal-ligand complexes are represented by the polynucleic metal complexes, mostly with a Cu(I) center, but also with Au, Ag and Pt central atoms[34, 35], generally displaying thermochromic shifts in their luminescence[27]. These, however, have been less intensively studied for their properties as sensors[27].
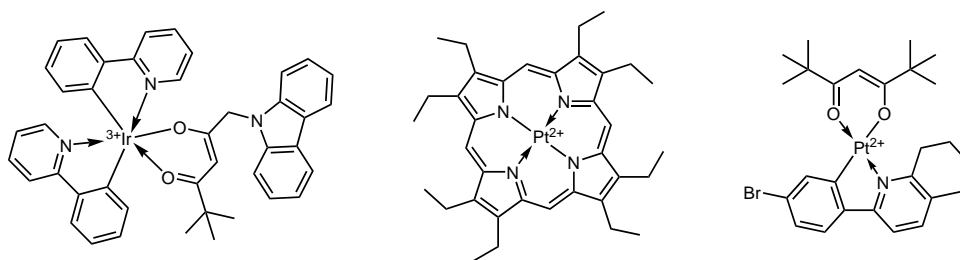
Figure 2.13: Structures of Ir(ppy)$_2$(carbac), platinum(II) octaethylporphyrin and Pt^{II}(Br-thq)(tBuacac), respectively.

Lanthanide Complexes

The lanthanide containing chelate complexes are another group of commonly used temperature probes. Generally Eu(III) and Tb(III) ions, the latter resulting in longer lifetimes, are used with various β-diketonate ligand and other additional (e.g. dipyrazoltriazine) ligands, representative structures depicted in structure 2.14. The excitation maximum can be shifted via adjusting the size of the conjugated π-electron systems of the ligands, cf. Eu(TTA)$_3$, Eu(TTA)$_3$(dbpt) (dbpt = 4-(4,6-di(1H-indazol-1-yl)-1,3,5-triazin-2-yl)-N,N-diethylaniline) and Eu(D2)$_3$phen (D2=1-(phenanthren-3-yl)-3-(phenanthren-9-yl)propane-1,3-dione), but generally lies within a range of 350 - 450 nm[27, 36]. Another concept used, but still involving β-diketonates, is the introduction of the lanthanide ions into coordination polymer frameworks, resulting in improved thermosensing performance[37].

2.3.4 Nanomaterials

Beside molecular temperature probes, nanomaterials also display temperature dependent properties enabling their use as thermosensors. Among the nanomaterials a few groups can be distinguished: quantum dots, metal clusters, nanoparticles and nano gels[27].
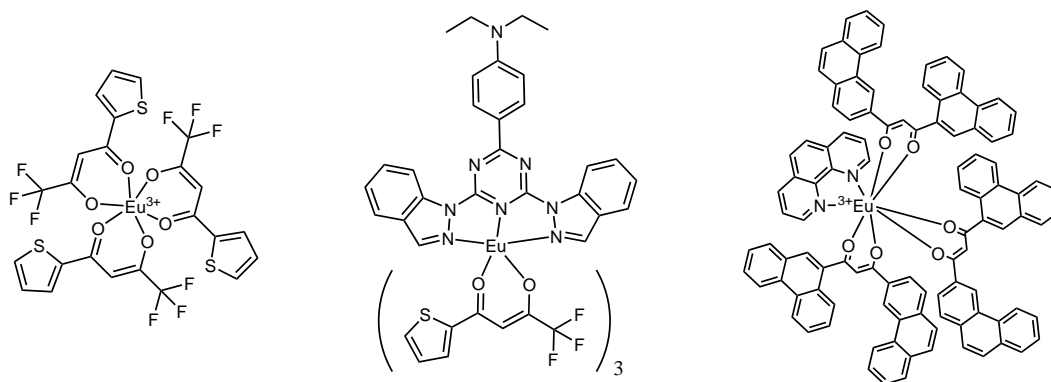
Figure 2.14: Structures of Eu(TTA)$_3$, Eu(TTA)$_3$(dbpt) and Eu(D2)$_3$phen, respectively.

Quantum Dots: semi-conductor nanocrystals, behaving like artificial atoms with discrete energy levels and its properties strongly depending on its size. Also the energy gap between the energy levels can be adjusted, becoming smaller with increasing size[38]. Therefore the optical properties can be easily tuned. They generally possess high quantum yields, good photostability and temperature dependent luminescence properties[26, 27, 31]. Usually Cd, Te and Se are used to synthesize various types (e.g. ultrathin films, core-shell) of quantum dots, which can also be immobilized in inert host polymers, but also low toxic quantum dots made of ZnS-$AgInS_2$ have been studied with respect to their temperature sensitivity[27].

Metal Clusters: similar to quantum dots, nano-sized metal clusters with surface capping agents can become luminescent with temperature dependent behaviour, which, however, was less extensively studied[27].

Nanoparticles: Various kinds of nanoparticles can be used for optical temperature sensing, e.g. photon upconverting nanoparticles (lanthanide doped nanocrystals), dye-doped nanoparticles (encapsulation of temperature sensitive dyes into e.g. polymer based nanoparticles) and others[27].

Nanogels: are typically made from several synthetic or biopolymers that have been crosslinked chemically or physically. Poly(N-isopropylacrylamide) was combined with a water sensitive fluorophore and now depending on the temperature, the environment of the fluorophore changes, therefore altering the luminescence properties[31].

2.3.5 Bulk Materials

Bulk materials as the name implies, do not depend on effects causing the properties of nanostructures. Further classification into inorganic (phosphors like (ZnS):Cu),

lanthanide-doped (e.g. $La_{1.92}Eu_{0.08}Zr_2O_7$), upconversion (e.g. $NaYF_4$ doped with Er^{3+}, Yb^{3+} or Tm^{3+}) and polymer based bulk materials (e.g. polydiacetylene) can be done[27].

2.4 Immobilization Matrices

The immobilization matrix serves to encapsulate and therefore immobilize the indicator dye to prevent leaching effects, to keep the concentration of the dye constant, while still providing the analyte access to the indicator[39]. Varying matrix environments influence the properties of the luminophore[39].

The solubility of the indicator in the matrix is a crucial point, a low solubility can result in aggregation or causes migration to more matching environments (e.g. other components of the sensor)[21]. Especially for planar π-extended molecules aggregation is an issue, but can be overcome by introduction of bulky substituents[21].

Sol-gel and polymer materials are the most common used immobilization matrices and shall be discussed briefly[39].

Sol-gel Matrices: Sol-gels are produced via hydrolysis and subsequent polycondensation of tetraalkoxysilanes, by using organically modified sol-gel precursors "ormosils" are produced, displaying improved properties regarding long-term stability, gas permeability and preparation[40].

Polymer Matrices: The most commonly used polymers for sensors among the huge diversity are glassy polymers (e.g. PS, PMMA, PVC, etc.), silicones (e.g. PDMS), fluoropolymers (e.g. poly(2,2,2-trifluoroethylemethacrylate)), hydrogels and cellulose derivatives[23, 39, 40].

2.4.1 Oxygen Sensors

For tuning the sensitivity of an oxygen sensor, the immobilization matrix is one of two key parameters[41]. The property, which is influencing the sensitivity is the oxygen permeability, given as oxygen permeability coefficient. In table 2.2 the permeability coefficients for oxygen in different polymers are shown.

The result of luminescence quenching by oxygen is the generation of reactive singlet oxygen, a strong oxidizing agent, that can lead to photodegradation of the indicator dye and the matrix. In terms of stability the different matrices are varying, generally with sol-gels being more phochemically stable than polymers[39].

Table 2.2: Oxygen permeabilities, given via the permeability coefficient P, of polymers commonly used for oxygen sensors[20].

Polymer	P x 10^{13} [$\frac{cm^3(STP)*cm}{cm^2 sPa}$]
Poly(diemthylsiloxane)	695
Ethylcellulose	11
Cellulose acetobutyrate	3,56
Polystyrene	2
Cellulose acetate	0,585
Poly(methylmethaacrylate)	0,116
Poly(vinyl chloride)	0,034
PET (Mylar A)	0,03

2.4.2 Temperature Sensors

Oxygen permeability is also an issue for temperature sensors, since most of them are sensitive towards oxygen quenching. Therefore oxygen impermeable or less oxygen permeable matrices are used. In table 2.3 commonly used polymers for temperature sensors are shown.

Table 2.3: Oxygen permeabilities, given via the permeability coefficient P, of polymers commonly used for temperature sensors[20].

Polymer	P x 10^{13} [$\frac{cm^3(STP)*cm}{cm^2 sPa}$]
Polyacrylonitrile	0.00015
Poly(styrene-co-acrylonitrile) 14/86	0.00320
Poly(vinylidenchloride) (Saran)	0.00383
Poly(vinyl alcohol)	0.00650
Poly(vinyl chloride)	0.034
Poly(styrene-co-acrylonitrile) 66/34	0.036

2.5 Anthraquinone and Derivatives
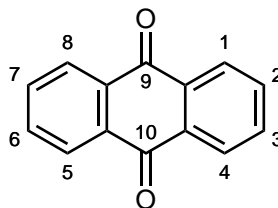
Figure 2.15: Structure of anthraquinone.

In the early 19th century Laurent relatively unnoticedly prepared anthraquinone, structure shown in figure 2.15, or as he called it "anthracenuse" for the first time via oxidation of anthracene with nitric acid [42, 43]. Only after discovery by Graebe and Liebermann, during their investigation of quinones in the 1870s, the new substance was called anthraquinone[42]. Apart from the naming, they also prepared anthraquinone by a procedure, which later became the first commercial method, to be more specific, via the oxidation of anthracene with bichromate and sulphuric acid[42].
Since then anthraquinone has considerably gained importance, due to all the valuable drugs[44] and especially dyestuffs[45] that are based on it, the use as catalyst in wood pulping[43] and production of hydrogen peroxide[46].

2.5.1 Industrial Production

This section is based on references [42, 43], others will be cited independently.
A common, when available, starting material for the production of anthraquinone is anthracene, which is generally isolated from coal tar. Besides anthracene, napthalene and the naphthalene process are gaining importance, since there is a continuous decrease in anthracene production since 1970s and the content of naphthalene in coal tar is with 10 % substantially higher compared to 1.5 % constituted by anthracene[47, 48]. In areas lacking a supply with anthracene anthraquinone is usually produced from phthalic acid anhydride and benzene.

Oxidation of Anthracene with Chromic Acid

The first commercial manufacturing process with its reaction scheme depicted in figure 2.16 is still carried out on industrial scale, as the reacted oxidizing agent, the aqueous Cr(III) sulfate lye is profitably disposed by further processing to tanning agents or electrochemically regenerated. Excess oxidizing agent is reduced with hydrogen sulfite. The received anthraquinone, however, must be carefully washed to remove chromium
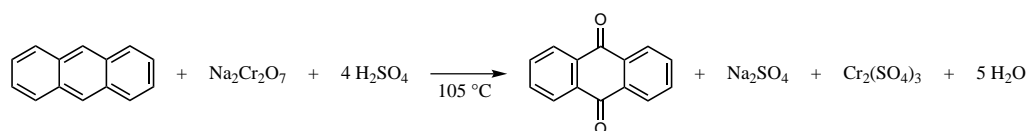
Figure 2.16: Reaction scheme of the oxidation of anthracene to anthraquinone using chromic acid.

salts. Subsequent to purification via recrystallisation from nitrobenzene purities up to 99 % are achieved.

Vapor-Phase Oxidation of Anthracene with Air
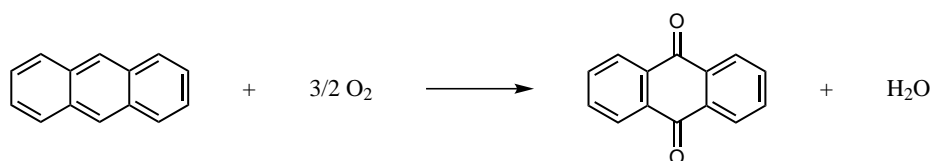
Figure 2.17: Reaction scheme of the vapor-phase oxidation of anthracene with air.

The catalytic vapour-phase oxidation of anthracene (reaction scheme depicted in figure 2.17), first described in 1916, produces anthraquinone with a purity of 99 %, enabling direct further conversion without purification. If at all, only small amounts of easily removable phthalic acid anhydride are formed as a byproduct. In the plants, anthracene is evaporated using a air-water vapour mixture and led into catalytic furnace or contact oven, where the oxidation takes place. The used catalyst shelves were coated with iron vanadate or vanadic acid doped with alkali or alkaline-earth metals. The gas mixture of product, air and steam is then lead through heat exchangers and eventually the formed anthraquinone is deposited in a cold room.

Naphthalene Process and Preparation via the Diels-Alder Reaction

This process, developed by Kawasaki Kasei Chemicals, is based on three steps, depicted in figure 2.18, the oxidation of naphthalene to naphthaquinone, which then is reacted in a Diels-Alder reaction with butadiene to form a tetrahydroanthraquinone which is reacted to the product via oxidation by air. The first step was found during the oxidation of naphthalene to phthalic acid anhydride as a side reaction. Through variation of the catalyst and other parameters the reaction can be shifted towards the formation of naphthaquinone, but still large amounts of phthalic acid anhydride are formed.
A similar method, was developed and used by BASF with its reaction scheme illustrated in 2.19. Here *p*-benzoquinone is reacted with 2 equivalents of butadiene in a double
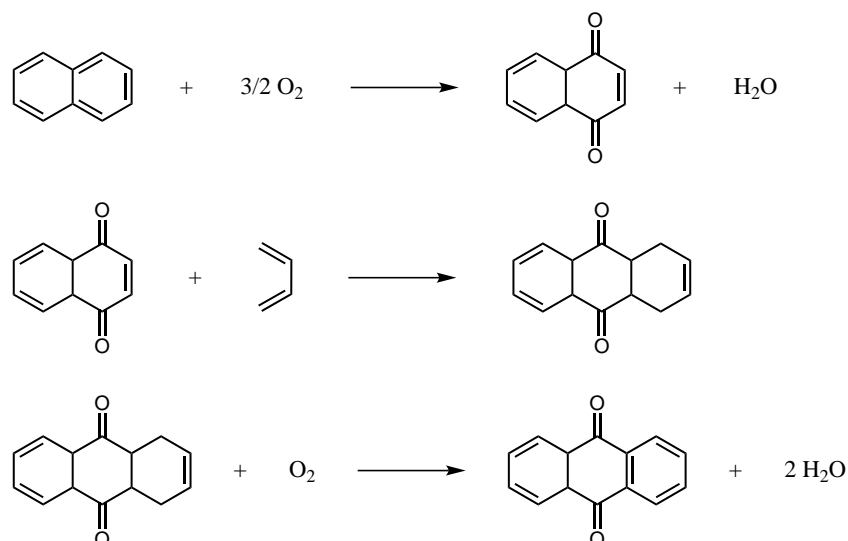
Figure 2.18: Reaction scheme of the production of anthraquinone from naphthalene using Diels-Alder reaction with subsequent oxidation, named naphthalene process.

Diels-Alder reaction and the received octahydroanthraquinone is subsequently oxidized by oxygen and in the presence of alkali to form anthraquinone.
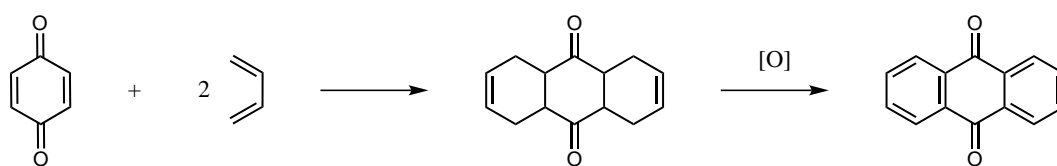
Figure 2.19: Reaction scheme of a procedure similar to the naphthalene process used by BASF, starting from 1,4-benzoquinone.

Friedel-Crafts Reaction - Synthesis from Phthalic Anhydride and Benzene
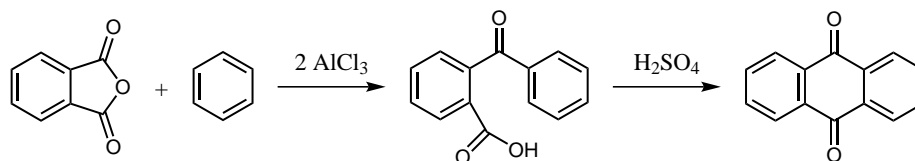
Figure 2.20: Reaction scheme of the preparation of anthraquinone from phthalic acid anhydride and benzene via a Friedel-Crafts reaction and subsequent cyclization by condensation.

The Friedel-Crafts reaction of phthalic acid anhydride and benzene, illustrated in figure 2.20, is the start for one of the two preferred methods, the other one being the vapour-phase oxidation of anthracene, for the preparation of anthraquinone. In this first

reaction step o-benzoylbenzoic acid is formed in high yields and purity, by using two equivalents of aluminium chloride preventing the formation of diphenylphthalide. The subsequent ring closure is usualy done in concentrated sulfuric acid or a weak oleum with almost quantitative yield. The Friedel-Crafts reaction is also used for the production of alkyl, aryl and halogene subsituted anthraquinones[45].

Styrene Process
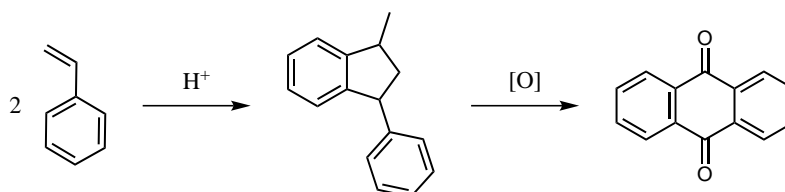
Figure 2.21: Reaction scheme of the preparation of anthraquinone from styrene via acid catalyzed dimerisation and subsequent oxidation.

Another procedure developed by BASF is the styrene process, illustrated in figure 2.21, in which during the first step 1-methyl-3-phenylindane is the reaction product of the acid catalyzed dimerisation of styrene and subsequent cyclization on the same catalyst. The next step is the vapor-phase oxidation of 1-methy-3-phenylindane via air to anthraquinone, here the same catalyst as in the vapor-phase oxidation of anthracene is used. The process only gave moderate to good yields, but styrene is an inexpensive starting material. The pilot however was not continued by BASF due to unforeseen problems.

2.5.2 Main Uses

Around 34000 t of anthraquinone are produces per year (1984), with the half production in Western Europe. Below the main uses are discussed briefly.

Anthraquinone Dyes and Intermediates[45]: The main use of anthraquinone is the use as a starting material for the production of a huge variety of dyes with representatives shown in figure 2.22, which are in fact expensive in production, but display superior properties, in term of color fastness and in the obtainable variety of colours. Regarding the importance they are only surpassed by azo dyes. The main starting reactions from anthraquinone are sulfonation and nitration in the α (1,4,5 or 8) position. β-substituted intermediates are usually prepared via the formation of the core structure from substituted phthalic acid anhydrides and benzene derivatives.
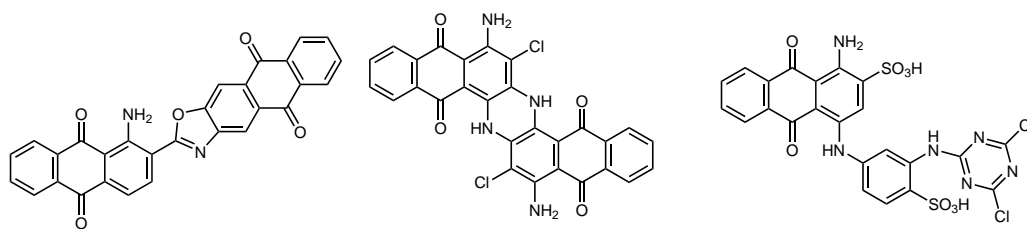
Figure 2.22: Structures of C.I. Vat Red 10 (anthraquinoneazole dye), C.I. Vat Green 11 (benzanthrone dye) and C.I.Reactive Blue 4 (reactive dye), respectively.

Wood Pulping: By addition of 0.03-0.05 % of anthraquinone during the production of pulp, the yield is increased 2.5 - 4 % with a simultaneous reduction of cooking time up to 30 %. Anthraquinone is acting as a redox catalyst, with the intermediate anthrahydroquinone catalysing the alkaline hydrolysis of lignin.

Hydrogen Peroxide Production[46]: The Anthraquinone Process, illustrated in figure 2.23, is the most widely used procedure for the production of hydrogen peroxide. 2-Alkylanthraquinones are hydrogenated with hydrogen in the presence of a catalyst to the corresponding hydroquinones. After removal of the catalyst, which would also catalyse the decomposition of the later produced hydrogen peroxide, the formed hydroquinone is oxidized with oxygen to regenerate the anthraquinone with quantitative formation of hydrogen peroxide. The aqueous crude product is usually received in concentrations from 15-40 wt% and is then purified and concentrated via distillation to final concentrations from 50 - 70 wt%.
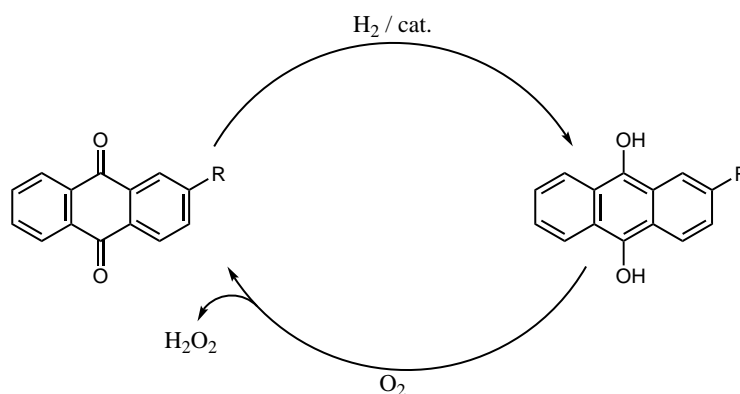
Figure 2.23: Reaction cycle of the Anthraquinone Process.

Drugs[44]: Anthraquinone based structures both of natural and synthetic origin display a variety of pharmacological activities including anticancer (Daunorubicin, Epirubicin [left in figure 2.24], Idarubicin, Mitoxantrone [right in figure 2.24], Pixantrone), antiinflammatory (anti-acne formulation from anthraquinone natural products[49]), antiarthritic (Diacerein),

antifungal (natural product extract with antifungal activity [50]), antibacterial (4,9-dioxo-4,9-dihydro-1*H*-naphtho[2,3-*d*][1,2,3]triazol-3-ium chloride salts [51]), antiviral (sulfonated anthraquinones and other anthraquinone derivatives [52]) and laxative (Aloe vera) effects.
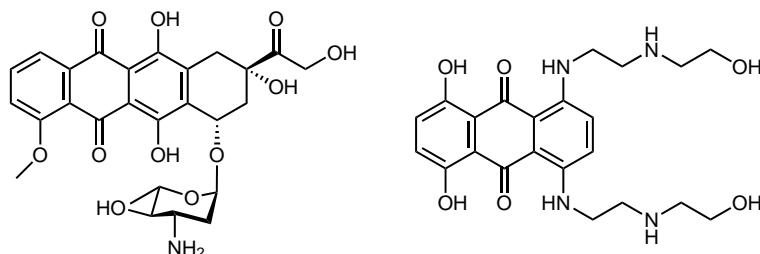
Figure 2.24: Structures of two clinicially approved anti-cancer drugs, Epirubicin and Mitoxantrone, respectively.

2.6 Transition Metal Catalyzed Cross Coupling and Related Reactions

[M]=Fe, Ni, Cu, Pd, Rh, ...
m=Li, Mg, B, Al, Si, Zn, Cu, Zr, Sn, ...
R, R'=C(sp), C(sp^2), (C(sp^3))
X=I, Br, Cl, OTf, ...
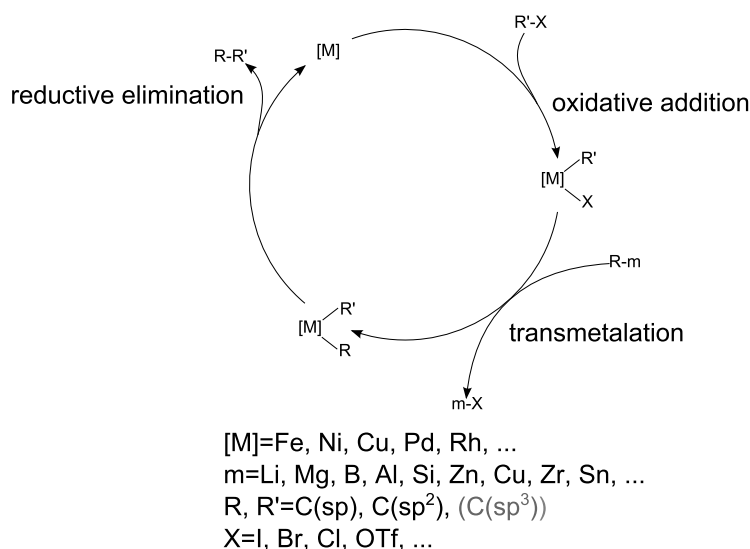
Figure 2.25: Illustration of a very general catalytic cycle of cross coupling reactions.

When considering forming C-C, C-N, C-O, C-S, C-P or C-M bonds, a class of synthetic transformations called "cross-coupling" reactions and related ones are nowadays often the methods of choice, providing an enormously versatile synthetic toolbox for synthetic protocols from natural product synthesis to industrial application[53, 54]. These reactions are done using transition metal catalysts, with Pd and Ni as common central atoms, but

more recently, with economical and ecological issues in mind, Fe is gaining importance in research[55]. Generally the cross-coupling reactions share large parts of their catalytic cycle, however, differ in some details. The reactions considered true "cross coupling" reaction share a sequence of oxidative addition of an organic electrophile (usually a halide or pseudohalide), transmetalation with one of a variety of hard or soft organometallic nucleophiles and reductive elimination of the product, as their catalytic cycle (depicted in figure 2.25), others generate their nucleophiles *in situ* via a base and an active C-H (e.g. Sonogashira) or X-H (e.g. Buchwald-Hartwig) compound[53, 54]. The reactions are generally classified according to the organometallic nucleophiles used, more the specifically the metal contained, c.f. table 2.4.

Below two selected (and during the synthetic part of this thesis applied) cross-coupling

Table 2.4: A selection of cross-coupling reactions named after their inventors[54].

Metal	Name
Li	Murahashi
Mg	Kumada-Tamao, Corriu
B	Suzuki-Miyaura
Al	Nozaki-Oshima, Negishi
Si	Tamao-Kumada, Hiyama-Hatanaka
Zn	Negishi
Cu	Normant
Zr	Negishi
Sn	Migita-Kosugi, Stille

or related reactions are discussed briefly.

2.6.1 Suzuki-Miyaura Coupling

In the Suzuki-Miyaura coupling organoboron compounds are used as organometallic nucleophiles. The organic groups attached to the boron are only weakly nucleophilic, but after addition of a Lewis base and the formation of an "-ate" complex (quarternization of the boron atom by complexation with a negatively charged base) even organoboronic acids and esters, are sufficiently reactive for the transmetalation to other metals[54–56]. However, organoboron reagents have a few distinct advantages, the formed boron by-products are generally easily removed and possess low toxicity, they are often air and water stable and many different reagents are commercially available[55]. Apart from this the reaction is convincing due to its flexibility concerning catalysts, bases, and solvents, allowing control over selectivity and its enormous functional group tolerance[55, 56]. The commonly used organoboron reagents usually belong to one of the following classes

boronic acids, boronic esters, organoboranes, organotrifluoroborate salts (easier purification) and *N*-methyliminodiacetic acid (MIDA) boronates (protected organoboron reagents for iterative couplings[57]) with representatives shown in figure 2.26. There are a few
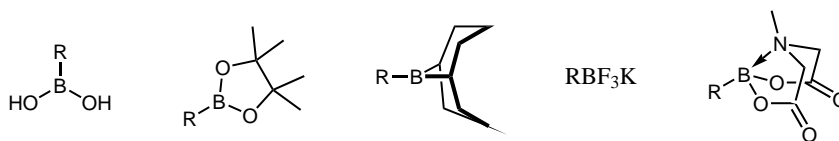
Figure 2.26: General structures of boronic acids, boronic esters, organoboranes, organotrifluoroborate salts and *N*-methyliminodiacetic acid boronates, respectively.

methods for the preparation of the above mentioned reagents (illustrated in figure 2.27)[53, 56]:

Transmetallation: preparation from organometallic reagents and trialkyl borates or haloboranes.

Hydroboration: addition of boranes to alkenes and alkynes.

Coupling Reactions: coupling reaction of diborons with organic halides and pseudohalides (e.g. Miyaura Borylation).

and others: like aromatic C-H borylation, olefin metathesis and cycloaddition reactions.
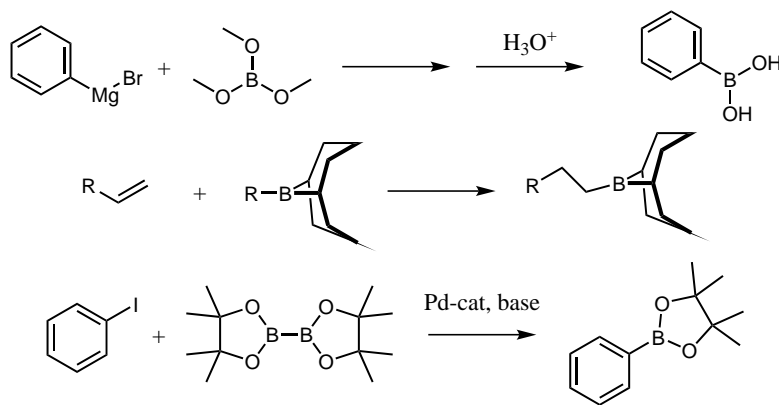
Figure 2.27: Reaction schemes for the transmetallation, hydroboration and coupling reaction methods for preparing organoboron reagents.

The preparation of the organotrifluoroborate salts from boronic acids is usually done by one of two methods, either the harsh variant using HF/KOH or KHF_2 or via KF and tartaric acid[58]. MIDA boronates are usually prepared via one of four generally methods, condensation with MIDA under Dean-Stark conditions, bromoboration of an alkyne and trapping with MIDA, transmetallation of organotrimethylsilanes with BBr_3

and subsequent trapping with the disodium salt of MIDA and via cross-metathesis with vinyl MIDA boronate[57].

2.6.2 Buchwald-Hartwig Amination

The Buchwald-Hartwig amination is the name for the Pd-catalysed formation of an C-N bond between an arylhalide (or sulfonate) and a primary or secondary amine (the reaction with ammonia has not been reported yet [53]). In contrast to genuine cross couplings the catalytic cycle involves four steps, oxidative addition, association of the amine, dehydrohalogenation and reductive elimination as illustrated in figure 2.28, however, the exact order of the individual steps is still under discussion[53]. Since the beginnings a
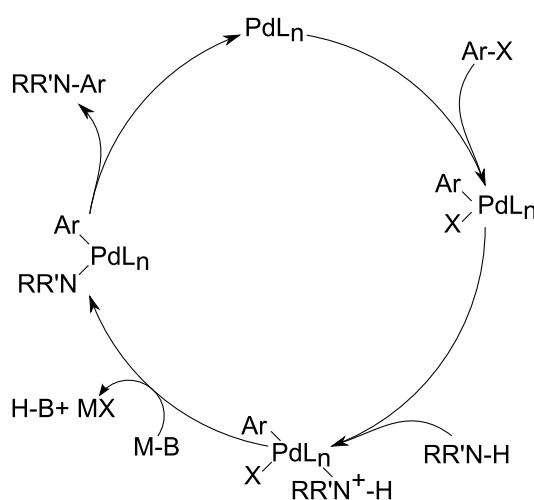
Figure 2.28: Illustration of a possible catalytic cycle for the Buchwald-Hartwig amination.

huge variety of synthetic protocols for this type amination reaction has been reported, reasoned by the much larger diversity in nitrogen reagents and the fact that these species bind much easier (sometimes even more than one at a time) to the central atom of the catalyst than for example organoboron reagents or trialkyltin reagents[53]. Therefore below some parameters of this reaction type shall be discussed briefly.

Catalyst: Generally $Pd_2(dba)_3$ and $Pd(OAc)_2$ are used as precatalysts, the latter requiring reduction to $Pd(0)$. The choice of ligands is crucial for C-N bond forming. Electron rich ligands stabilize the oxidized Pd favouring oxidative addition, bulky ligands the dissociation of additional ligands for forming the active species and also favour reductive elimination, however, too bulky substituents can cause ineffective binding of substrates and precipitation of $Pd(0)$[53]. An example for an excellent ligand concerning activity and stability would be XPhos (2',4',6'-triisopropyl-2-dicyclohexylphosphinobiphenyl).

Base: The base is particularly important for functional group tolerance and reaction rate. Strong bases like NaOtBu provide fast reaction rates, but have limited functional group tolerance. Cs_2CO_3 being a milder much tolerant base, however, it is important to note, that the combination of base and nitrogen nucleophile is responsible for the functional group compatibility[53].

Sovlent: Essential for C-N couplings are deoxygenated solvents as the reactions are air-sensitive. The most common solvent is toluene, but others like DME, dioxane, DMF and NMP have been used to[53].

Reaction Temperatures: Depending especially on the base and other conditions reaction temperatures usually lie within room temperature and 120 °C[53].

3 Material and Methods

3.1 Chemicals

Table 3.1: List of used chemicals

Chemicals	CAS	Supplier
10-Bromo-7*H*-benzo[*c*]carbazole	1698-16-4	TCI
2,6-Dibromoanthraquinone	633-70-5	TCI
2-Bromo-9,9-dimethylfluorene	28320-31-2	TCI
3,6-di-*tert*-butyl-9*H*-carbazole	37500-95-1	TCI
Bis(4-(2-phenylpropan-2-yl)phenyl)amine	10081-67-1	TCI
4-Bromophthalic anhydride	86-90-8	TCI
4-Methyl-*N*-phenylaniline	620-84-8	TCI
(9,9-Diheptyl-9*H*-fluorene-2,7-diyl)diboronic acid	916336-19-1	Frontier Scientific
(9,9-Dimethyl-9*H*-fluoren-2-yl)-boronic acid	333432-28-3	TCI
Aluminium chloride	7446-70-0	Fluka
Bromine	7726-95-6	Aldrich
Diphenylamine	122-39-4	Acros Organics
Morpholine	110-91-8	Sigma Aldrich
N-[4-(9-Phenyl-9*H*-carbazol-3-yl)phenyl]-[1,1'-biphenyl]-4-amine	1160294-96-1	TCI
Pd(PPh$_3$)$_4$	14221-01-3	ABCR
PEPPSI-IPr-Cat	905459-27-0	Sigma Aldrich
Poly(phenylsilsesquioxane)	70131-69-0	ABCR
Polyphosphoric acid	8017-16-1	Aldrich
Potassium carbonate	584-08-7	Roth
Potassium *tert*-butoxide	865-47-4	Sigma Aldrich
Sodium hydride	7646-69-7	Aldrich
Sodium *tert*-butoxide	865-48-5	Sigma Aldrich
Tetrafluorophthalonitrile	1835-65-0	TCI

Table 3.2: List of used polymers

Polymer	CAS	Supplier
Polystyrene, M_W=260.000	9003-53-6	Acros
Polyacrylonitrile, M_W=150.000	25014-41-9	Sigma Aldrich
Poly(vinylidene chloride-*co*-acrylonitrile), 20wt% acrylonitrile content, av. M_n=80.000, av. M_W=125.000	9010-76-8	Scientific Polymer
Poly(styrene-*co*-acrylonitrile), M_W=185.000	9003-54-7	Sigma Aldrich
Ethylcellulose (49% ethoxyl content)	9004-57-3	Sigma Aldrich
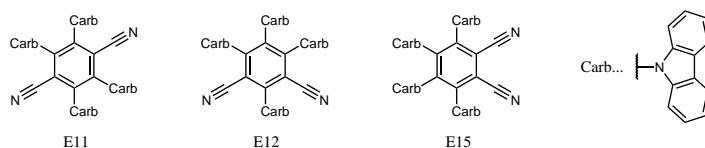
Figure 3.1: Structure of compounds **18**, **19** and **20**.

The dicyanobenzene based dyes E11(**18**), E12(**19**), E15(**20**) depicted in figure 3.1, were synthesized by Wolfgang Jud according to literature [12].
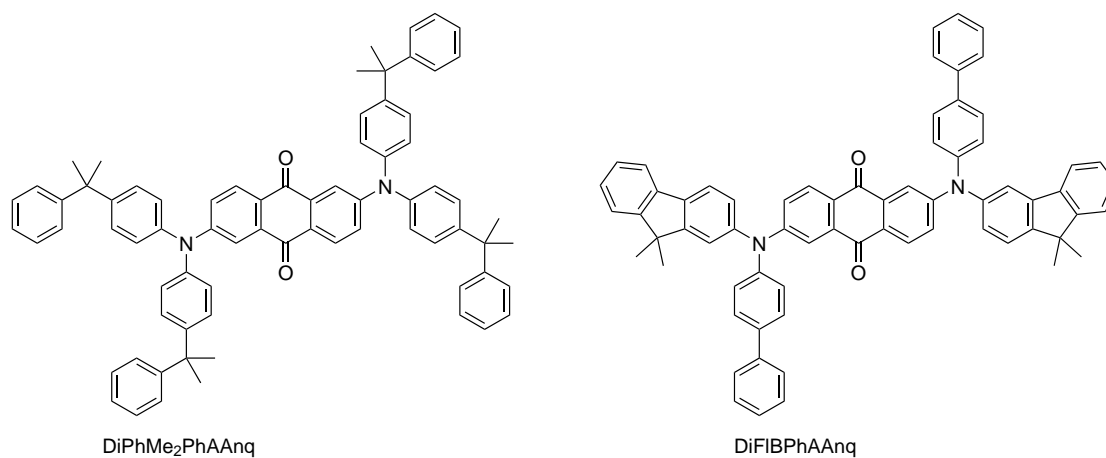
Figure 3.2: Structure of compounds **21**and **22**.

The dyes DiPhMe₂PhAAnq (**21**) and DiFlBPhAAnq (**22**), depicted in figure 3.2, were synthesized by Anna Walcher analogously to literature procedure[13].

3.2 Solvents

Chloroform: was bought from *Roth* and used as recieved.

Cyclohexane: was bought from *VWR Chemicals* and used as recieved.

Dichloromethane: was bought from *VWR Chemicals* and used as recieved.

Ethyl Acetate: was bought from *VWR Chemicals* and used as recieved.

Methanol: was bought from *VWR Chemicals* and used as recieved.

Novec 7200: was bought from *3M* and used as recieved.

Tetrahydrofuran: was bought from *VWR Chemicals* and used as recieved.

Tetrahydrofuran, abs.: stabilizer-free THF was distilled over Na with benzophenone as indicator (blue when dry) and stored over 4 Åmolecular sieve.

Toluene: was bought from *VWR Chemicals* and used as recieved.

Toluene, abs.: the bought toluene was stored over 4 ÅMS (20% m/v) for at least 24 h.

3.3 Chromatography

3.3.1 Thin Layer Chromatography

For thin layer chromatography silica gel plates from *Merck* (*silica gel 60 F$_{254}$ aluminium sheets 20x20*) were used. As detection methods UV – detection, KMnO$_4$ and CAM staining with subsequent developing by hot air stream were used. The UV – detection was carried out at λ=254 and 366 nm.

3.3.2 Flash Column Chromatography

For preparative flash column chromatography silica gel from *Acros Organics* (silica gel, for chromatography 0.035 – 0.070 mm, 60 Å, nitrogen flushed) was used. The amount of silica used, depending on the specific separation problem, was in general the 100 fold of the amount of crude product, for less soluble products the 250 fold amount was used. Column diameter was chosen to give a filling level between 15 and 25 cm. As fraction size, typically half the volume of the used volume silica gel was chosen. The eluent was generally selected to result in a R$_F$-value between 0.15 and 0.3 of the to-be-isolated substance.

3.4 Structural and Chemical Characterization

3.4.1 Nuclear Magnetic Resonance Spectroscopy (NMR)

^{1}H-, ^{13}C- and APT NMR spectra were recorded on a *Bruker AVANCE III* equipped with an autosampler (300.36 MHz-^{1}H-NMR, 75.53 MHz-^{13}C-NMR). The chemical shifts were reported using the residual signal of the used solvent as an internal standard. All of the given ^{13}C- and APT NMR spectra were proton decoupled intending to clear up the spectra. The measured signals were reported as follows: chemical shift δ in ppm (parts per million), number of protons, multiplicity, coupling constant J in Hz, and the proposed assignment. For the multiplicities the following abbreviations were used: s (singlet), d (doublet), t (triplet), q (quartet), m (multiplet), dd (doublet of a doublet).

3.4.2 High Resolution Mass Spectrometry (HRMS)

Mass spectrometry was performed in a positive reflector on a *Micromass TofSpec 2E Time-of-Flight Mass Spectrometer*/on a MALDI-TOF/TOF (Bruker Ultraflex Extreme) by Prof. Dr. Robert Saf's group at the Institute for Chemistry and Technology of Materials, Graz University of Technology. External calibration was done with a suitable mixture of poly(ethyleneglycol)s (PEG). Analysis of data was done with *MassLynx-Software V4.1* from *Waters*.

3.4.3 Crystal Structure Determination

XRD data collection was performed on a *Bruker APEX II diffractometer* with Mo Kα radiation (λ= 0.71073 Å) and a CCD area detector by Prof. Dr. Roland Fischer at the Institute of Anorganic Chemistry, Graz University of Technology.

3.5 Photophysical Characterization

3.5.1 Absorption spectra

Absorption spectra were recorded on a *VARIAN CARY 50 conc*, UV-Vis spectrophotometer by *Varian* or on *Agilent Cary 60 UV-VIS* by *Agilent Technologies*. Measurements were performed at fast scan rate wit baseline correction using the corresponding solvent as blank. *Hellma Analytics 100-OS 10 mm precision* cuvettes made of special optical glass were used.

Molar absorption coefficients were determined by preparing a stock solution of the dye in CHCl$_3$, subsequent dilution in toluene and using Lambert-Beer law for calculation.

3.5.2 Emission and Excitation Spectra

Emission and excitation spectra of the dyes in toluene and the foils were recorded on a *FluoroLog® 3 spectrofluorometer* from *Horiba Scientific* equipped with a *R2658* photomultiplier from *Hamamazu* using *Hellma Analytics 100-OS 10 mm precision* cuvettes or *Hellma 100-QS 10 mm precision* cuvettes with screw-caps and *FluorEssence™* software.

3.5.3 Lifetime Measurement

Lifetimes were determined using single photon counting recorded on *FluoroLog® 3 spectrofluorometer* from *Horiba Scientific* with a *DeltaHub* module controlling a *SpectraLED-390* ($\lambda = 392nm$) and using *DAS-6 Analysis* for data analysis. Data were fitted using a mono- or bi-exponential decay. Average lifetimes were calculated from equation 3.1

$$\tau_{av} = \frac{\sum\limits_{i=1}^{n} B_i T_i^2}{\sum\limits_{i=1}^{n} B_i T_i} \tag{3.1}$$

with B values from a pre-exponential function relating to how much of an emitting species there is (calculated by the data analysis software). The B values are also used to calculate the relative amplitude f, via weighting by the lifetime, equation 3.2.

$$f = \frac{B_i T_i}{\sum\limits_{i=1}^{n} B_i T_i} \tag{3.2}$$

Lifetimes of sensor foils were measured using a custom built flow-through cell and continuous nitrogen purging.

3.5.4 Quantum Yields

Quantum yields were determined using an absolute approach method employing a *Quanta-Φ* integrating sphere-based set-up from *Horiba Scientific* on a *FluoroLog® 3 spectrofluorometer* from *Horiba Scientific* and *FluorEssence™* for data analysis. A neutral density filter characterised by 5% transmission was used (actual transmission spectrum in the appendix, figure 10.43) and the appropriate correction factor (1/transmission) for the chosen wavelength was used for calculation. Quantum Yields in solution requiring anoxic

conditions were measured with cuvettes with screw-caps after degassing the dye solution by purging with Ar for 15 min. The *Quanta-Φ* integrating sphere is not well suited for measuring quantum yields of sensor foils under deoxygenated conditions. Quantum yields were measured at ambient air and the quantum yields requiring anoxic conditions (overall and QY of TADF) were calculated from the received quantum yields and three intensity based measurements at anoxic, ambient air and oxygenated conditions. From the measured intensities, ratios were calculated, which were used to adapt the quantum yields.

$$\Phi_F = \Phi_{air} * \frac{I_{ox}}{I_{air}} \tag{3.3}$$

$$\Phi = \Phi_F * \frac{I_{anoxic}}{I_{ox}} \tag{3.4}$$

$$\Phi_{TADF} = \Phi - \Phi_F \tag{3.5}$$

3.5.5 Oxygen Calibrations

Oxygen calibrations of the sensor films were done by performing intensity based measurements on a *Hitachi-F-7000 spectrofluorometer* in a flow-through cell at a constant temperature of 25 °C established by a *Julabo F12-ED* refrigerated/heating circulator. For producing different oxygen partial pressures a gas-mixing device based on two mass-flow controllers, *Voegtlin red-y smart series*, with a custom built software and nitrogen, compressed air and oxygen as gases were used.

3.5.6 Temperature Dependency

For temperature dependency measurements constant temperature was established by using a *Cary SPV - 1X0 Single Cell Peltier Accessory* peltier element from *Varian* in combination with a *Julabo F12-ED* refrigerated/heating circulator.

3.5.7 Photostability

For the photostability tests, the sensor films were exposed to the irridation of a three LED array (at 11.5 V, P=18 W, $\lambda(Em_{max})$=465nm, spectrum of the emitted light measured with a *Qmini* from *RGB Photonics*, spectrum in the appendix, figure 10.42) equipped with a focussing lens producing a photon flux of 5500 µmol s^{-1} m^{-2} measured by a *LI-250A Light Meter* from *LI-COR Bieosciences*. The sensor foils were placed diagonally in a *Hellma Analytics 100-OS 10 mm precision* cuvette in the focus of the lens. The

decrease of the absorption of the sensor foils was measured as a function of irradiation time.

3.6 Sensor Film Preparation

For knife coating 1 and 3 Mil Wet Film (25 and 75 µm thick) knives from *BYK-Gardner* were used. The prepared dye cocktail were knife coated onto 125 µm biaxially-oriented polyethylene terephthalate foils (*MELINEX 506*) supplied by *Pütz GmbH + Co. Folien KG.*

4 Experimental

4.1 Experiments

4.1.1 2,6-bis([1,1'-biphenyl]-4-yl(4-(9-phenyl-9H-carbazol-3-yl)phenyl)amino)-anthracene-9,10-dione (1)
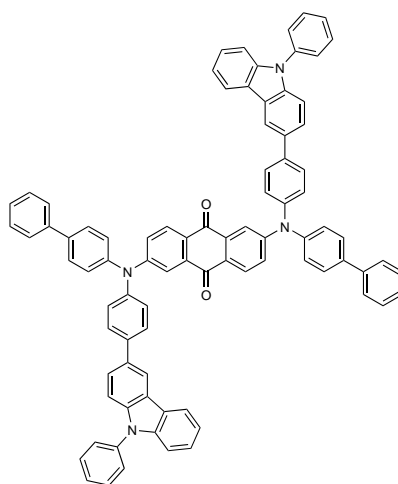
Figure 4.1: Structure of compound **1**

Procedure analogously to: Q. Zhang, H. Kuwabara, W. J. Potscavage, S. Huang, Y. Hatae, T. Shibata, C. Adachi, *Journal of the American Chemical Society* **2014**, *136*, 18070–18081.

50.8 mg of 2,6-dibromoanthraquinone (139 µmol, 1 eq), 40.1 mg (357 µmol, 2.57 eq) potassium *tert*-butoxide, 146.9 mg (302 µmol, 2.18 eq) *N*-[4-(9-Phenyl-9H-carbazol-3-yl)phenyl]-[1,1'-biphenyl]-4-amine and 7.1 mg (10 µmol, 0.08 eq) PEPPSI™-IPr catalyst were placed in a flame dried and Argon flushed 25 mL Schlenk-tube under Ar counterflow. Then the Schlenk-tube was evacuated and Ar-flushed (5 cycles). 5 ml of dry toluene degassed by purging with Ar for 15 min were added to the reagents. After stirring for one minute the orange reaction mixture was placed in a preheated oil bath at 100 °C and

was stirred at 100 °C for 2 h taking on a brown colour. After quantitative conversion monitored by TLC (CH/DCM=1+1) the reaction mixture was allowed to cool to R.T. and precipitated from 25 ml of a mixture of MeOH/H_2O=9+1. The black precipitate was washed with MeOH (3x 20 ml). The crude product was dried at 60 °C in a drying oven overnight and then purified by flash column chromatography (CH/DCM=3+2, R_f=0.17).

Yield: 50 mg (31 %), dark purple solid

$C_{86}H_{56}N_4O_2$ [1177.42 g/mol]

^{1}H-NMR (300.36 MHz, CDCl$_3$): δ 8.38 (d, $^4J_{HH}$ = 1.8 Hz, 2H), 8.20 (d, $^3J_{HH}$ = 7.7 Hz, 2H), 8.12 (d, $^3J_{HH}$ = 8.7 Hz, 2H, Anq), 7.94 (d, $^4J_{HH}$ = 2.5 Hz, 2H, Anq), 7.78 – 7.55 (m, 22H), 7.53 – 7.28 (m, 26H)

APT-NMR (75.53 MHz, CDCl$_3$): δ 182.1 (C_q^{Ar}, C=O, Anq), 153.1, 145.30, 144.5, 141.5, 140.6, 140.5, 139.4, 138.2, 137.8, 135.8, 132.7, 130.4, 129.3, 129.0, 128.8, 128.7, 127.7, 127.5, 127.2, 127.1, 126.8, 126.5, 126.4, 126.3, 125.4, 124.1, 123.9, 123.6, 120.5, 120.2, 118.8, 117.1, 110.3, 110.1 ppm

TLC: R_f=0.17 (CH/DCM=3+2)

MALDI TOF: *m/z*: [M$^+$] calc.: 1176.44, found: 1176.48

ε(toluene, $\lambda_{max}[nm]$\M^{-1}cm^{-1}): 327\92500, 380\37500, 470\23500

4.1.2 3,4,5,6-tetrakis(3,6-di-*tert*-butyl-9*H*-carbazol-9-yl)phthalonitrile

(2)
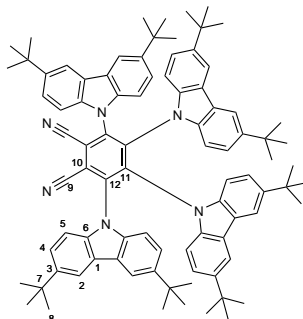
Figure 4.2: Structure of compound **2**

Procedure analogously to: H. Uoyama, K. Goushi, K. Shizu, H. Nomura, C. Adachi, *Nature* **2012**, *492*, 234–238.

In a flame dried and Argon flushed 25 mL Schlenk-tube 103 mg (369 µmol, 4.98 eq) 3,6-di-*tert*-butyl-9*H*-carbazole were dissolved in 3 ml of dry THF under inert conditions. Then 26.5 mg (663 µmol, 8.96 eq) of a 60% NaH dispersion in mineral oil were added to the stirred solution under Ar counterflow giving a cloudy colourless solution. When no more gas evolution could be observed, 14.8 mg (74 µmol, 1 eq) 3,4,5,6-tetrafluorophthalonitrile were added under inert conditions to immediately give an orange/yellow solution. After quantitative conversion detected by TLC (CH+EE=5+1, R_f=0.76, yellow spot) the reaction was stopped by addition of 3 ml brine. Subsequent to phase separation the aqueous layer was extracted with DCM (3x 5 mL) and the pooled organic fractions were dried over Na_2SO_4. The yellow crude product was purified by flash column chromatography (CH/EE=95+5, R_f=0.46) and vacuum sublimation (10 mbar, removal of excess 3,6-di-*tert*-butyl-9*H*-carbazole).

Yield: 30 mg (33 %), intense yellow solid.

$C_{88}H_{96}N_6$ [1237.78 g/mol]

^{1}H-NMR (300.36 MHz, CDCl$_3$):δ 7.59 (d, $^4J_{HH}$ = 2.0 Hz, 4H, 2), 7.23 (d, $^4J_{HH}$ = 2.0 Hz, 4H, 2), 6.94 (dd, $^3J_{HH}$ = 8.5, $^4J_{HH}$= 2.0 Hz, 4H, 4), 6.80 (d, $^3J_{HH}$ = 8.5 Hz, 4H, 4), 6.72 (d, $^3J_{HH}$ = 8.5 Hz, 4H, 5), 6.57 (dd, $^3J_{HH}$ = 8.5, $^4J_{HH}$ = 2.0 Hz, 4H, 5), 1.37 (s,

36H, *tert*-butyl, 8), 1.20 (s, 36H , *tert*-butyl, 8).

APT-NMR (75.53 MHz, CDCl$_3$):δ 144.26 (C$_q^{Ar}$-Carb, 3), 143.89 (C$_q^{Ar}$-Carb, 3), 141.44(C$_q^{Ar}$-core, 12), 139.77 (C$_q^{Ar}$-core, 11), 136.91 (C$_q^{Ar}$-N, 6), 136.32 (C$_q^{Ar}$-N, 6), 124.85 (C$_q^{Ar}$-Carb, 1), 124.53 (C$_q^{Ar}$-Carb, 1), 123.10(C$_t^{Ar}$-Carb, 2), 122.71 123.10 (C$_t^{Ar}$-Carb, 2), 115.99 (C$_t^{Ar}$-Carb, 4), 115.43(C$_t^{Ar}$-Carb, 4), 113.39 (C$_q$, CN, 9), 109.80 (C$_t^{Ar}$-Carb, 5), 109.55 (C$_t^{Ar}$-Carb, 5), 100.13 (C$_q^{Ar}$-CN, 10), 34.72(C$_q$, *tert*-Bu, 7), 34.47(C$_q$, *tert*-Bu, 7), 32.04 (CH$_3$, 8), 31.84 (CH$_3$, 8) ppm

TLC: R$_f$=0.46 (CH/EE=95+5)

MALDI TOF: *m/z*: [M$^+$] calc.: 1237.77, found: 1237.74

ε(toluene, $\lambda_{max}[nm]$\M^{-1}cm^{-1}): 383\24500

4.1.3 (3,6-di-*tert*-butyl-9*H*-fluoren-9-yl)-difluoro-morpholinophthalonitrile (3)
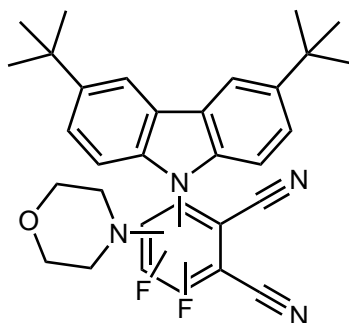
Figure 4.3: Structure of compound **3**

In a flame dried and Ar flushed 15 ml Schlenk-tube 109 mg (390 µmol, 1.05 eq) 3,6-di-*tert*-butyl-9*H*-carbazole were dissolved in 5 ml dry THF under inert conditions. Then 26.1 mg (540 µmol, 1.45 eq) of a 60% NaH dispersion in mineral oil were added to stirred solution under Ar counterflow giving a cloudy colourless solution. When no more gas evolution could be observed, 74.6 mg (373 µmol, 1 eq) of 3,4,5,6-tetrafluorophthalonitrile were addded undert inert conditions to give a intense yellow solution. After quantitative conversion of the phthalonitrile monitored by TLC (CH/EE=5+1), the reaction was

diluted with 5 ml DCM and quenched with 3 ml brine. The aqueous layer was extracted with DCM (3x 5 ml). The combined organic layer was dried over Na_2SO_4 and then the solvent was removed under reduced pressure. Subsequently the solid was dissolved in 15 ml of 1-methyl-2-pyrrolidone and 260 µl (3 mmol, 8 eq) of morpholine were added. The reaction mixture was heated to 100 °C and kept stirring for 30 min. Then the solution was allowed to cool down to room temperature and was then diluted with 30 ml DCM and 15 ml H_2O. The aqueous layer was extracted with DCM(3x 5 ml). After phase separation the solvent of the combined organic layer was removed under reduced pressure. The product mixture was separated by flash column chromatography (CH/EE=95+5, R_f=0.17).

Yield: 17 mg, yellow solid, no exact structure was determined, 1+1 morpholine and carbazole substitution was indicated by NMR and MS.

^{1}H-NMR (300.36 MHz, $CDCl_3$):δ 8.12 (d, $^4J_{HH} = 1.9$ Hz, 2H, Carb-H), 7.50 (dd, $^3J_{HH} = 8.6$, $^4J_{HH} = 1.9$ Hz, 2H, Carb-H), 6.94 (d, $^3J_{HH} = 8.6$ Hz, 2H, Carb-H), 3.28 (t, $^3J_{HH} = 4.7$ Hz, 4H, morpholine: CH_2-O), 2.85 (t, $^3J_{HH} = 3.4$ Hz, 4H, morpholine: CH_2-N), 1.46 (s, 18H, *t*-Bu) ppm. APT-NMR (75.53 MHz, $CDCl_3$):δ 145.13, 137.44, 124.55, 124.29, 117.14, 109.24, 66.55, 49.88, 35.03, 32.08 ppm. (Quarternary carbons of benzene core and nitriles are missing.)
TLC: R_f=0.17 (CH/EE=95+5)

MALDI TOF: *m/z*: [M$^+$] calc.: 526.25, found: 526.27

ε(toluene, $\lambda_{max}[nm]$\M^{-1}cm^{-1}): 366\11000

4.1.4 2,6-bis(diphenylamino)anthracene-9,10-dione (4)
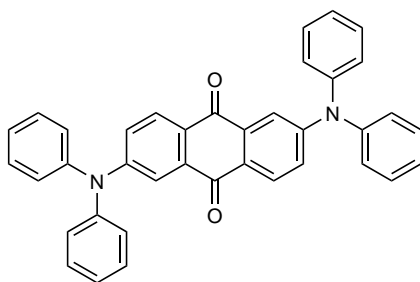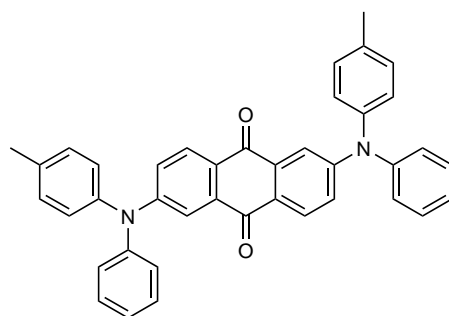

Figure 4.4: Structure of compound **4**

Procedure according to: Q. Zhang, H. Kuwabara, W. J. Potscavage, S. Huang, Y. Hatae, T. Shibata, C. Adachi, *Journal of the American Chemical Society* **2014**, *136*, 18070–18081.

A flame dried and Argon flushed 25 mL Schlenk-tube was charged with 250.4 mg (684 µmol, 1 eq) 2,6-dibromoanthraquinone, 191.8 mg (1.71 mmol, 2.50 eq) potassium *tert*-butoxide, 241.2 mg (1.43 mmol, 2.08 eq) diphenylamine and 22.9 mg PEPPSI™-IPr catalyst (34 µmol, 0.05 eq) under Ar counterflow. Then the Schlenk-tube was evacuated and Ar-flushed (5x cycles). 8 ml of dry toluene degassed by purging with Ar for 15 min were added to the reagents. After stirring for one minute the reaction mixture was placed in a preheated oil bath and was stirred at 100 °C for 2 hours taking on a brown colour. After quantitative conversion monitored by TLC (CH/EE=5+1, R_f(Anq)=0.66) the reaction mixture was allowed to cool to R.T. and precipitated from 50 ml of a mixture of MeOH/H_2O=9+1. After centrifugation, the red precipitate was collected and dried at 60 °C overnight. The crude product was purified by flash column chromatography (CH/DCM=3+1, detection by TLC CH/EE=5+1, R_f=0.51).

Yield: 142 mg (38 %), red solid.

$C_{38}H_{26}N_2O_2$ [542.64 g/mol]

^{1}H-NMR (300.36 MHz, CDCl$_3$):δ 8.02 (d, $^3J_{HH}$ = 8.7 Hz, 2H, Anq), 7.76 (d, $^4J_{HH}$ = 2.6 Hz, 2H, Anq), 7.41 – 7.29 (m, 8H, Ph), 7.23 – 7.13 (m, 14H, Ph + Anq) ppm

APT-NMR (75.53 MHz, CDCl$_3$):δ 182.08 (C_q^{Ar}, C=O, Anq), 153.17C (C_q^{Ar}, Anq-N), 146.06 ($_q$, Ph-N), 135.64 (C_q^{Ar}, Anq), 130.00 (C_t^{Ar}, Ph), 129.15 (C_t^{Ar}, Anq), 126.46 (C_t^{Ar}, Ph), 126.15 ($_q$, Anq), 125.51 (C_t^{Ar}, Ph), 123.38(C_t^{Ar}, Anq), 116.64(C_t^{Ar}, Anq) ppm

TLC: R_f=0.51 (CH/EE=5+1)

ε(toluene, λ_{max}\M^{-1}cm^{-1}): 370\34000, 448\23000

Analytical data are in accordance with those reported.

4.1.5 2,6-bis(bis(4-bromophenyl)amino)anthracene-9,10-dione (5)
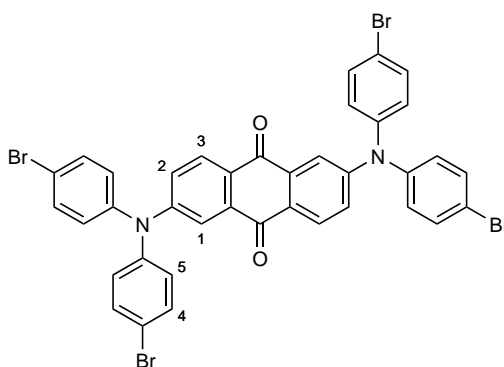
Figure 4.5: Structure of compound **5**

In 25 ml round-bottom flask 35.5 mg **4** (65 µmol, 1 eq) were dissolved in 8 ml of CHCl$_3$ and a catalytic amount of FeCl$_3$ was added. Then 1 ml of a 0.254 M (254 µmol, 3.88 eq) Br$_2$ solution in CHCl$_3$ (130µl Br$_2$ to a final volume of 10 ml) was added drop wise via syringe to the solution. After stirring for 30 min, the reaction mixture was quenched with 5 ml 2 wt% Na$_2$SO$_3$ aqueous solution. Subsequent to phase separation the organic layer was filtered through silica using DCM and the solvent was removed under reduced pressure. The crude product was purified by flash column chromatography (gradient starting with CH/DCM=3+1, detection by TLC CH/EE=5+1, R$_f$=0.64)

Yield: 31 mg (55 %), red solid.

C$_{38}$H$_{22}$Br$_4$N$_2$O$_2$ [858.22 g/mol]

^{1}H-NMR (300.36 MHz, CD$_2$Cl$_2$):δ 8.04 (d, ^{3}J$_{HH}$ = 8.7 Hz, 2H, 3), 7.71 (d, ^{4}J$_{HH}$ = 2.5 Hz, 2H, 1), 7.55 – 7.44 (m, 8H, 4), 7.23 (dd, ^{3}J$_{HH}$ = 8.7,^{4}J$_{HH}$ = 2.5 Hz, 2H, 2),

7.10 – 7.03 (m, 8H, 5)

APT-NMR (75.53 MHz, CD$_2$Cl$_2$): δ 181.97 (C$_q^{Ar}$, C=O, Anq), 171.54 (C$_q$), 145.43 (C$_q$), 139.02 (C$_q$), 138.62 (C$_q$), 133.59 (C$_t^{Ar}$, Ph), 129.58 (C$_t^{Ar}$, Anq, 128.17 (C$_t^{Ar}$, Ph), 124.89 (C$_t^{Ar}$, Anq), 118.90 (C$_q^{Ar}$, Ph-Br), 117.80 (C$_t^{Ar}$, Anq) ppm

TLC: R$_f$=0.64 (CH/EE=5+1)

ε(toluene, λ_{max}\M^{-1}cm^{-1}): 372\30000, 448\20000

4.1.6 6,6'-(9,9-diheptyl-9*H*-fluorene-2,7-diyl)bis(2-bromoanthracene-9,10-dione) (6)
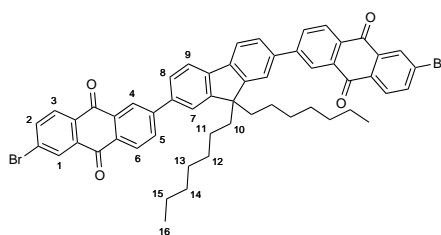
Figure 4.6: Structure of compound **6**

In a flame dried and Ar flushed 25 ml Schlenk-tube 10 ml of a mixture of toluene/THF/H$_2$O = 7+2+1 were degassed by purging with Ar for 10 min. Then 34.4 mg (76 µmol, 1 eq) (9,9-diheptyl-9*H*-fluorene-2,7-diyl)diboronic acid , 85.4 mg (233 µmol, 3.05 eq) 2,6-dibromoanthraquinone and 47.1 mg (341 µmol, 4.46 eq) K$_2$CO$_3$ were added under Ar counterflow. Subsequent to degassing the yellow suspension another 10 min by purging with Ar, it was placed in a preheated oil bath at 80 °C and stirred for 10 min. Then 5 mg (4 µmol, 0.06 eq) PdCl$_2$(amphos)$_2$ were added under Ar counterflow. The reaction mixture was stirred at 80 °C for 17 h until quantitative conversion of the fluorene was detected by TLC (DCM/MeOH=4+1, R$_f$(Fluorene)=0.40). Then the flask was allowed to cool down to room temperature. Afterwards the mixture was diluted with 5 ml H$_2$O and 15 ml EE. After phase separation the organic layer was filtered through silica using DCM/MeOH=4+1. The product mixture was then purified by flash column chromatography (gradient starting with CH/DCM=2+1, detection by TLC CH/DCM=1+1, R$_f$=0.53) and vacuum sublimation to remove residual anthraquinone.

Yield: 7 mg (10 %), yellow solid.

$C_{55}H_{48}Br_2O_4$ [932.79 g/mol]

^{1}H-NMR (300.36 MHz, CDCl$_3$):δ 8.63 (d, $^4J_{HH}$ = 2.0 Hz, 2H, 4), 8.48 (d, $^4J_{HH}$ = 2.0 Hz, 2H, 1), 8.42 (d, $^3J_{HH}$ = 8.1 Hz, 2H, 6), 8.23 (d, $^3J_{HH}$ = 8.3 Hz, 2H, 3), 8.13 (dd, $^3J_{HH}$ = 8.1, $^4J_{HH}$ = 2.0 Hz, 2H, 5), 7.95 (dd, $^3J_{HH}$ = 8.3, $^4J_{HH}$ = 2.0 Hz, 2H, 2), 7.90 (d, $^3J_{HH}$ = 7.9 Hz, 2H, 9), 7.77 (dd, $^3J_{HH}$ = 7.8, $^4J_{HH}$ = 1.7 Hz, 2H, 8), 7.72 (d, $^4J_{HH}$ = 1.7 Hz, 2H, 7), 2.19 – 2.06 (m, 4H, 10), 1.19 – 0.98 (m, 16H, CH$_2$), 0.75 (t, J = 6.9 Hz, 6H, 16), 0.72 – 0.62 (m, 4H, CH$_2$) ppm

TLC: R$_f$=0.53 (CH/DCM=1+1)

4.1.7 6,6'-(9,9-diheptyl-9H-fluorene-2,7-diyl)bis(2-(bis(4-(2-phenylpropan-2-yl)phenyl)amino)anthracene-9,10-dione) (7)
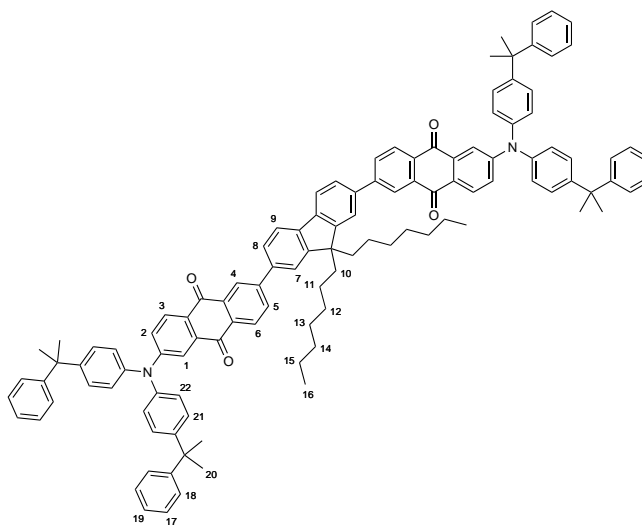
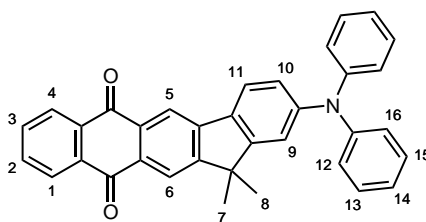**Figure 4.7:** Structure of compound **7**

A flame dried and Ar flushed 10 ml Schlenk-tube was charged with 7 mg (8 µmol, 1 eq) **6**, 3 mg (27 µmol, 3.35 ←eq) potassium *tert*-butoxide, 8 mg (20 µmol, 2.47 eq) bis(4-(2-phenylpropan-2-yl)phenyl)amine and 2.3 mg PEPPSI™-IPr catalyst (3 µmol, 0.42 eq) under inert conditions. Then the Schlenk was evacuated and Ar flushed (5 cycles). 2 ml

of dry toluene degassed by purging with Ar for 10 min were added to the reagents. After stirring the reaction mixture for one minute, the Schlenk flask was placed in a preheated oil bath at 100 °C and the intense red solution was kept stirring for one hour. The reaction mixture was allowed to cool down to R.T. and was then precipitated from 10 ml of a mixture of MeOH/H_2O=9+1. The precipitate was collected after centrifugation and then the crude product was purified by flash column chromatography (CH/DCM=1+1, R_f=0.49).

Yield: 3 mg (24 %), red solid.

$C_{115}H_{108}N_2O_4$ [1582.14 g/mol]

^{1}H-NMR (300.36 MHz, CDCl$_3$):δ 8.61 (d, $^4J_{HH} = 2.0$ Hz, 2H, 4), 8.33 (d, $^3J_{HH} = 8.1$ Hz, 2H, 6), 8.15 (d, $^3J_{HH} = 8.7$ Hz, 2H, 3), 8.04 (d, $^3J_{HH} = 8.0$ Hz,$^4J_{HH} = 2.0$ Hz , 2H, 5), 7.87 (d, $^3J_{HH} = 7.8$ Hz, 2H, 9), 7.81 (d, $^4J_{HH} = 2.4$ Hz, 2H, 1), 7.76 (dd, 8,$^3J_{HH} = 7.8$ Hz, $^4J_{HH}$=1.7 Hz, 2H, 8), 7.72 (d, $^4J_{HH} = 1.7$ Hz, 2H, 7), 7.37 – 7.27 (m, 16H, Ph), 7.22 (m, 12H, Ph+Anq), 7.08 (d, $^3J_{HH} = 8.6$ Hz, 8H, Ph), 2.11 (m, 4H), 1.72 (s, 24H, 20), 1.16 – 1.04 (m, 16H), 0.75 (t, J = 6.9 Hz, 6H, 16), 0.71 – 0.60 (m, 4H) ppm

TLC: R_f=0.49 (CH/DCM=1+1)

MALDI TOF: *m/z*: [M$^+$] calc.: 1581.83, found: 1581.80

ε(toluene, λ_{max}\M^{-1}cm^{-1}): 379\20000, 492\4500

4.1.8 2,6-bis(bis(4-(9,9-dimethyl-9*H*-fluoren-2-yl)phenyl)amino)anthracene-9,10-dione (8)
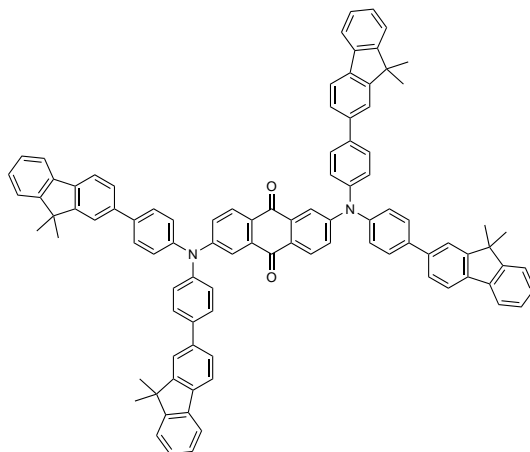
Figure 4.8: Structure of compound **8**

34 mg **5** (40 µmol, 1 eq), 33.9 mg potassium carbonate (239 mol, 6.03 eq) and 43.7 mg (9,9-dimethyl-9*H*-fluoren-2-yl)boronic acid (184 µmol, 4.63 eq) were placed in a flame dried and Ar flushed 25 ml Schlenk-tube. Then 5 ml of a mixture of toluene/THF/H$_2$O=2+2+1 were added and the suspension was degassed by purging with Ar for 15 min. Subsequently the Schlenk-tube was placed in a preheated oil bath at 80 °C and after 2 min of stirring, 5 mg (4 µmol, 0.11 eq) of Pd(PPh$_3$)$_4$ were added under Ar counterflow. The reaction mixture was kept stirring at 80 °C for 24 h and then allowed to cool down to R.T. before it was filtered through silica using DCM. The solvent was then removed under reduced pressure to give a red solid. The crude product was then purified by flash column chromatography (CH/EE=19+1, R$_f$=0.19).

Yield: 10 mg (19 %), red solid.

C$_{98}$H$_{74}$N$_2$O$_2$ [1311.68 g/mol]

^{1}H-NMR (300.36 MHz, CDCl$_3$):δ 8.12 (d, J = 8.7 Hz, 2H, Anq), 7.95 (d, ^{4}J$_{HH}$ = 2.5 Hz, 2H, Anq), 7.80 (d, ^{3}J$_{HH}$ = 7.9 Hz, 4H, Fl), 7.78 – 7.74 (m, 4H, Fl), 7.68 (m, 12H, Ph(8H)+Fl(4H)), 7.60 (dd, ^{3}J$_{HH}$ = 8.0, ^{4}J$_{HH}$ = 1.8 Hz, 4H, Fl), 7.48 – 7.44 (m, 4H, Fl), 7.40 – 7.29 (m, 18H, Fl+Ph(8H)), 1.56 (s, 24H, CH$_3$) ppm

APT-NMR (75.53 MHz, CDCl$_3$):δ 182.11, 154.50, 154.03, 152.99, 145.07, 139.59, 138.97, 138.78, 138.71, 135.78, 129.32, 128.73, 127.45, 127.20, 126.55, 126.46, 126.12, 123.96, 122.78, 121.39, 120.50, 120.23, 117.24, 47.13, 27.4 ppm

TLC: R$_f$=0.19 (CH/EE=19+1)

MALDI TOF: *m/z*: [M$^+$] calc.: 1311.58, found: 1311.56

ε(toluene, λ_{max}\M^{-1}cm^{-1}):345\62000, 472\13000

4.1.9 2-(phenyl(*m*-tolyl)amino)-6-(phenyl(*p*-tolyl)amino)anthracene-9,10-dione (9)

Figure 4.9: Structure of compound **9**

Procedure analogously to: Q. Zhang, H. Kuwabara, W. J. Potscavage, S. Huang, Y. Hatae, T. Shibata, C. Adachi, *Journal of the American Chemical Society* **2014**, *136*, 18070–18081.

A flame dried and Ar flushed 25 ml Schlenk-tube was charged with 249.3 mg (681 µmol, 1 eq) 2,6-dibromoanthraquinone, 191.7 mg (1.71 mmol, 2.51 eq) potassium *tert*-butoxide, 262.8 mg (1.43 mmol, 2.11 eq) 4-methyl-*N*-phenylaniline and 27.4 mg (40 µmol, 0.06 eq) PEPPSI™-IPr catalyst under inert conditions. The Schlenk-tube was then evacuated and Ar flushed (5 cycles). 8 ml of dry toluene, degassed by purging with Ar for 20 min, were added and the reaction mixture was stirred for one minute. Then it was placed in a preheated oil bath at 100 °C and the kept stirring for 1.5 hours before it was allowed to cool down to room temperature. The reddish brown reaction mixture was then precipitated from 40 ml of a mixture of MeOH/H$_2$O=9+1. The intense red precipitate

was then isolated by vacuum filtration and washed with MeOH (3x25 ml). The crude product was dried in the drying oven at 60°C overnight and then purified by flash column chromatography (CH/DCM=3+1, R_f=0.1).

Yield: 196 mg (50 %), red solid.

$C_{40}H_{30}N_2O_2$ [570.69 g/mol]

^{1}H-NMR (300.36 MHz, CDCl$_3$):δ 8.00 (d, $^3J_{HH}$ = 8.7 Hz, 2H, Anq), 7.72 (d, $^4J_{HH}$ = 2.6 Hz, 2H, Anq), 7.39 – 7.29 (m, 4H, Ph), 7.22 – 7.13 (m, 12H, Ph+Anq), 7.11 – 7.03 (m, 4H, Ph), 2.36 (s, 6H, CH$_3$) ppm

APT-NMR (75.53 MHz, CDCl$_3$):δ 182.13 (C$_q$, C=O, Anq), 153.30 (C$_q$, Anq-N), 146.08 (C$_q$, Ph-N), 143.38(C$_q$, CH$_3$-Ph-N), 135.66 (C$_q^{Ar}$), 135.61 (C$_q^{Ar}$), 130.70(C$_t^{Ar}$, Ph), 129.92(C$_t^{Ar}$, Ph), 129.11 (C$_t^{Ar}$, Anq), 126.72 (C$_t^{Ar}$, Ph) , 126.23 (C$_t^{Ar}$, Ph) , 125.82 (C$_q^{Ar}$ Anq), 125.32(C$_t^{Ar}$, Ph), 122.78(C$_t^{Ar}$, Anq), 116.13 (C$_t^{Ar}$, Anq), 21.15 (CH$_3$) ppm

TLC: R_f=0.1 (CH/DCM=3+1)

MALDI TOF: m/z: [M + 2H]$^+$ (c.f. [59]) calc.: 572.25, found: 572.18

ε(toluene, λ_{max}\M^{-1}cm^{-1}): 373\27000, 453\19000

4.1.10 2,6-bis((4-bromophenyl)(*p*-tolyl)amino)anthracene-9,10-dione
(10)
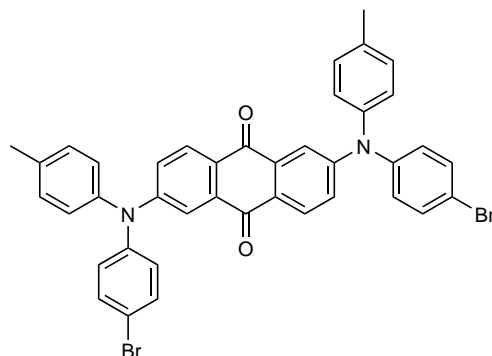
Figure 4.10: Structure of compound **10**

In a 100 ml round-bottom flask 158 mg (277 µmol, 1 eq) **9** were dissolved in 40 ml CHCl$_3$ and a catalytic amount of FeCl$_3$ was added. Then 725 µl of a 0.766 M (535 µmol, 1.93 eq) Br$_2$ solution in CHCl$_3$ were added dropwise via syringe to the stirred solution. After quantitative conversion was detected by TLC (CH/EE=4+1, R$_f$(E)=0.65 , R$_f$(P)=0.72) the reaction mixture was quenched with 15 ml 10 wt% Na$_2$SO$_3$ aqueous solution. After addition of 10 ml H$_2$O, the organic layer was separated and filtered through silica using DCM. Then the solvent was removed under reduced pressure. The product was not further purified.

Yield: 192 mg (95 %), red solid.

C$_{40}$H$_{28}$Br$_2$N$_2$O$_2$ [728.48 g/mol]

^{1}H-NMR (300.36 MHz, CDCl$_3$):δ 8.02 (d, ^{3}J$_{HH}$ = 8.7 Hz, 2H, Anq), 7.72 (d, ^{4}J$_{HH}$ = 2.5 Hz, 2H, Anq), 7.48 – 7.40 (m, 4H, Ph), 7.21 – 7.13 (m, 6H, Ph+Anq), 7.09 – 7.01 (m, 8H, Ph), 2.36 (s, 6H, CH$_3$) ppm

APT-NMR (75.53 MHz, CDCl$_3$):δ 181.95 (C$_q^{Ar}$, C=O, Anq), 152.88 (C$_q^{Ar}$, Anq-N), 145.26 (C$_q$, Ph-N), 143.00 (C$_q$, CH$_3$-Ph-N), 136.01(C$_q^{Ar}$), 135.63(C$_q^{Ar}$), 132.99 (C$_t^{Ar}$, Ph), 130.86 (C$_t^{Ar}$, Ph), 129.24 (C$_t^{Ar}$, Anq), 127.38(C$_t^{Ar}$, Ph), 126.67 (C$_t^{Ar}$, Ph), 126.26(C$_q^{Ar}$ Anq), 123.36 (C$_t^{Ar}$, Anq), 118.02(C$_q^{Ar}$, Ph-Br), 116.61 (C$_t^{Ar}$, Anq), 21.16 (CH$_3$) ppm

TLC: R$_f$=0.74 (CH/EE=4+1)

ε(toluene, λ_{max}\M^{-1}cm^{-1}): 373\26500, 452\18000

4.1.11 2-(bis(4-(2-phenylpropan-2-yl)phenyl)amino)-13,13-dimethyl-6H-indeno-[1,2-b]-anthracene-6,11(13H)-dione (11)
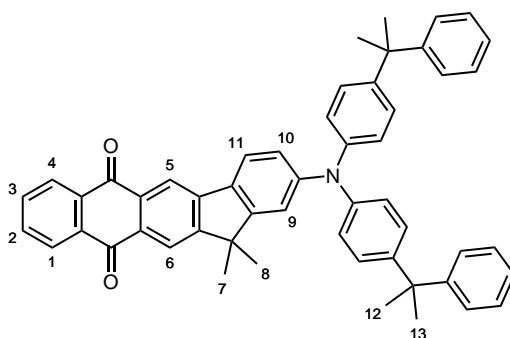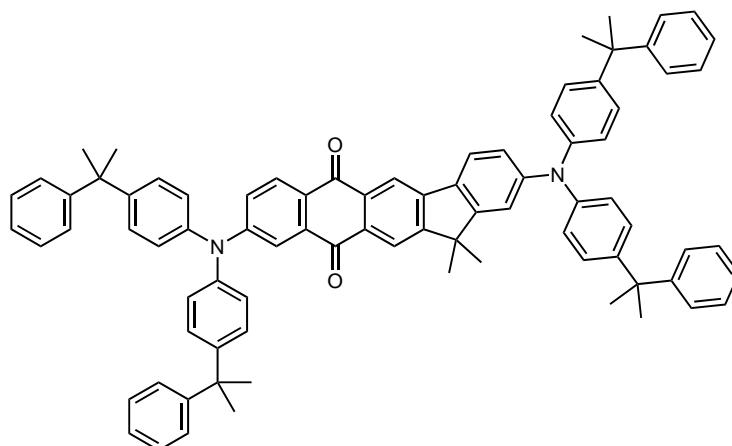

Figure 4.11: Structure of compound **11**

In a flame dried and Ar flushed 25 ml Schlenk-tube 75.5 mg (187 µmol, 1eq) 2-bromo-13,13-dimethyl-6H-indeno[1,2-b]anthracene-6,11(13H)-dione (**23**), 89.9 mg (222 µmol, 1.18 eq) bis(4-(2-phenylpropan-2-yl)phenyl)amine, 55.3 mg (493 µmol, 2.63 eq) potassium *tert*-butoxide and 9.9 mg (15 µmol, 0.08 eq) PEPPSI™-IPr catalyst were placed under inert conditions. Then Schlenk was evacuated and Ar flushed (5 cycles). Subsequently the Schlenk tube was equipped with a flame dried dropping funnel, which was then charged with 7 ml dry toluene. After degassing the toluene by purging with Ar for 15 min, it was added to the reagents and stirred for 1 min at room temperature. Then the reaction mixture was placed in a preheated oil bath at 100 °C and kept stirring for 3 h. Then the Schlenk was allowed to cool down to room temperature and kept stirring for 60 h at room temperature. The reaction mixture was then precipitated from 35 ml of a mixture of MeOH/H2O=9+1. After centrifugation the received solid was collected and purified via flash column chromatography (gradient elution starting from CH/DCM=4+1, detection via TLC: CH/EE=4+1, R$_f$=0.45).

Yield: >54mg (40 %), red solid. (26 mg of crude product left)

C$_{53}$H$_{45}$NO$_2$ [727.95 g/mol]

^{1}H-NMR (300.36 MHz, CDCl$_3$):δ 8.48 (s, 1H, 5), 8.38 – 8.32 (m, 2H, 1,4), 8.31 (s, 1H, 6), 7.83 – 7.75 (m, 2H, 2,3), 7.71 (d, ^{3}J$_{HH}$ = 8.3 Hz, 1H, 11), 7.34 – 7.27 (m, 8H, Ph), 7.22 – 7.12 (m, 7H, Ph+9), 7.04 (d, ^{3}J$_{HH}$ = 8.5 Hz, 5H, Ph+10), 1.70 (s, 12H, 12,13), 1.49 (s, 6H, 7,8) ppm

APT-NMR (75.53 MHz, CDCl$_3$):δ 183.85 (C$_q^{Ar}$, C=O, Anq), 183.34 (C$_q^{Ar}$, C=O, Anq), 159.40 (C$_q^{Ar}$), 156.26 (C$_q^{Ar}$), 150.74 (C$_q^{Ar}$), 149.80 (C$_q^{Ar}$), 146.02(C$_q^{Ar}$), 145.62 (C$_q^{Ar}$), 144.97 (C$_q^{Ar}$), 134.11 (C$_q^{Ar}$), 134.06(C$_q^{Ar}$), 133.88, 133.80, 132.19 (C$_q^{Ar}$), 131.78 (C$_q^{Ar}$), 130.84 (C$_q^{Ar}$), 128.16, 127.87, 127.30, 126.91, 125.79, 124.39, 122.48, 122.25, 121.47, 117.68, 116.56, 47.68 (C$_q$), 42.74 (C$_q$,), 30.94 (CH$_3$), 26.89 (CH$_3$) ppm

TLC:R$_f$=0.45 (CH/EE=4+1)

MALDI TOF: *m/z*: [M$^+$] calc.: 727.35, found: 727.32

ε(toluene, λ_{max}\M^{-1}cm^{-1}): 389\23000, 485\9000

4.1.12 2-(diphenylamino)-13,13-dimethyl-6*H*-indeno-[1,2-*b*]-anthracene-6,11(13*H*)-dione (12)

Figure 4.12: Structure of compound **12**

A flame dried and Ar flushed 10 ml Schlenk-tube was charged with 49.4 mg (122 µmol, 1 eq) **23**, 25.8 mg (152 µmol, 1.24 eq) diphenylamine, 34.6 mg (308 µmol, 2.52 eq) potassium *tert*-butoxide and 8.3 mg (12 µmol, 0.1 eq) PEPPSI™-IPr catalyst under inert conditions. Then 5 ml of dry toluene, degassed by purging with Ar for 10 mins, were added under Ar counterflow to the reagents. The reaction mixture was then stirred for 1 min at room temperature and then placed in a preheated oil bath at 100 °C. The dark

orange suspension was kept stirring for 3 h before it was allowed to cool down to room temperature and kept stirring for 60 h at room temperature. The reaction mixture was then precipitated from 25 ml of a mixture of MeOH/H$_2$O=9+1. After centrifugation the received solid was collected and purified via flash column chromatography (gradient elution starting from CH/DCM=4+1, detection via TLC: CH/EE=4+1, R$_f$=0.36).

Yield: 33 mg (55 %), red solid. C$_{35}$H$_{25}$NO2 [491.59 g/mol]

^{1}H-NMR (300.36 MHz, CDCl$_3$):δ 8.49 (s, 1H, 5), 8.37 – 8.32 (m, 2H, 1,4), 8.31 (s, 1H, 6), 7.80 (m, 2H, 2,3), 7.74 (d, ^{3}J$_{HH}$ = 8.4 Hz, 1H, 11), 7.35 – 7.27 (m, 4H, 13,15), 7.21 – 7.13 (m, 5H, 12,16), 7.13 – 7.04 (m, 3H, 10,14), 1.49 (s, 6H, 7,8) ppm

APT-NMR (75.53 MHz, CDCl$_3$):δ 183.78 (C$_q^{Ar}$, C=O, Anq), 183.33 (C$_q^{Ar}$, C=O, Anq), 159.42 (C$_q^{Ar}$), 156.35 (C$_q^{Ar}$), 149.72 (C$_q^{Ar}$), 147.63 (C$_q^{Ar}$), 145.48 (C$_q^{Ar}$), 134.11, 134.03 (C$_q^{Ar}$), 133.90, 133.80 (C$_q^{Ar}$), 133.77 (C$_q^{Ar}$), 131.91 (C$_q^{Ar}$), 131.29 (C$_q^{Ar}$), 129.57, 127.30, 125.07, 123.68, 122.61, 122.58, 121.50, 117.79, 116.99, 47.72(C$_q$), 26.83 (CH$_3$) ppm

TLC: R$_f$=0.36 (CH/EE=4+1)

MALDI TOF: m/z: [M$^+$] calc.: 491.19, found: 491.19

ε(toluene, λ_{max}\M^{-1}cm^{-1}): 382\23000, 466\9000

4.1.13 2-(bis(4-bromophenyl)amino)-13,13-dimethyl-6*H*-indeno-[1,2-*b*]-anthracene-6,11(13*H*)-dione (13)
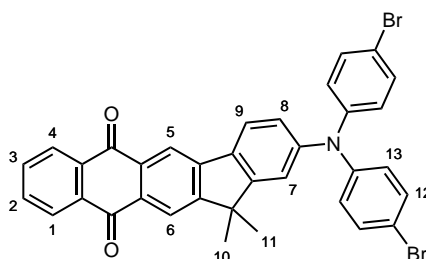
Figure 4.13: Structure of compound **13**

In 50 ml round-bottom flask 15 mg (31 µmol, 1 eq) **12** were dissolved in 10 ml $CHCl_3$ and 5 mg (31 µmol, 1 eq) $FeCl_3$ were added. 60 µl of a 1.01 M (61 µmol, 1.99 eq) Br_2 solution in $CHCl_3$ were added via syringe under stirring to the intense red solution. After quantitative conversion (5 min) monitored via TLC (CH/EE=4+1, R_f(E)=0.59, R_f(P)=0.64) the reaction was quenched with 5 ml 10 wt% Na_2SO_3 aqueous solution. Subsequent to phase separation the organic layer was washed with 5 wt% Na_2SO_3 (1x5 mL). The pooled organic fractions were dried over Na_2SO_4 and then the solvent was removed under reduced pressure. The red crude product was purified via flash column chromatography (CH/DCM=4+1, detection via TLC: CH/EE=4+1, R_f=0.64)

Yield: 8 mg (40 %), intense orange solid

$C_{35}H_{23}Br_2NO_2$ [649.38 g/mol]

^{1}H-NMR (300.36 MHz, $CDCl_3$):δ8.52 (s, 1H, 5), 8.38 – 8.33 (m, 2H, 1,4), 8.33 (s, 1H, 6), 7.79 (m| d, 2|1H, 2,3|9), 7.40 (d, $^3J_{HH} = 8.6$ Hz, 4H, 12), 7.15 (d, $^4J_{HH} = 1.6$ Hz, 1H, 7), 7.07 (dd, $^3J_{HH} = 8.6$ Hz, $^4J_{HH}$ 1.6 Hz, 1H), 7.02 (d, $^3J_{HH} = 8.6$ Hz, 4H, 13), 1.50 (s, 6H, 10,11) ppm

183.33 (C_q^{Ar}), C=O, Anq), 159.44 (C_q^{Ar}), 156.60 (C_q^{Ar}), 148.65 (C_q^{Ar}), 146.39 (C_q^{Ar}, Anq-N), 145.05 (C_q^{Ar}), 134.20 (C_t^{Ar}), 134.01 (C_t^{Ar}), 133.83 (C_q^{Ar}), 133.75 (C_q^{Ar}), 132.74 (C_t^{Ar}, Ph), 132.48 (C_q^{Ar}), 132.24 (C_q^{Ar}), 127.35 (C_t^{Ar}), 126.22 (C_t^{Ar}, Ph), 123.27 (C_t^{Ar}), 122.86 (C_t^{Ar}), 121.60 (C_t^{Ar}), 118.10 (C_t^{Ar}), 117.79 (C_t^{Ar}), 116.49 (C_q^{Ar}, C-Br), 47.84 (C_q, C-10/11), 26.84 (10,11) ppm

TLC: R_f=0.64 (CH/EE=4+1)

ε(toluene, λ_{max}\M^{-1}cm^{-1}): 337\26500, 383\26000, 466\9500

4.1.14 2,9-dibromo-13,13-dimethyl-6*H*-indeno-[1,2-b]-anthracene-6,11(13*H*)-dione
(14)
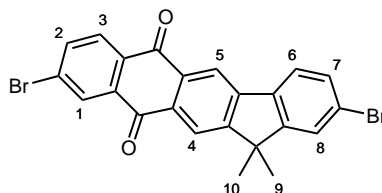
Figure 4.14: Structure of compound **14**

Procedure similar to: E. Lee, J.-S. Lee, T.-h. Kim, K.-s. Kim, *Anthracene derivatives and organic electroluminescent device using same*, US Patent 8,395,144, Google Patents, **2013**.

In a 250 ml round-bottom flask equipped with a drying funnel 1.50 g (6.63 mmol, 1.11 eq) 5-bromoisobenzofuran-1,3-dione and 1.64 g (5.99 mmol, 1 eq) 2-bromo-9,9-dimethyl-9*H*-fluorene were dissolved in 70 ml and cooled to 0°C with an ice bath. Then 1.80 g (13.5 mmol, 2.25 eq) AlCl$_3$ were gradually added to the clear solution. The initially yellow/orange solution was stirred overnight (16 h) at room temperature. The greenish brown reaction mixture was then poured onto a mixture of 20 ml 1 M HCl and 180 ml ice water. After the ice had molten, the product was extracted from the aqueous layer with DCM (3x50 mL). The combined organic layers were dried over Na$_2$SO$_4$ and the solvent was removed under reduced pressure. The received solid was finely ground and then washed with CH (4x25 ml). The dried solid was then placed in a 250 ml round-bottom flask and 50 ml polyphosphoric acid were added. The reaction mixture was stirred at 120 °C for 2 hours and was then allowed to cool to room temperature. The thick blue suspension was then poured onto 500 ml H$_2$O and a yellow precipitate formed, which was isolated by vacuum filtration. The solid was then washed with water (2x100 mL), saturated NaHCO$_3$ solution(1x200 ml) and water(1x200 ml). The crude product mixture (2 isomers, yellow [main product] and red solids) was purified via flash column chromatography (gradient elution: starting from CH/DCM=5+1 to CH/DCM=3+2, detection TLC CH/EE=4+1, R$_f$=0.45) and trituration with CHCl$_3$ (desired product is less soluble in CHCl$_3$).

Yield: 238 mg (8 %), yellow solid

C$_{23}$H$_{14}$Br$_2$O$_2$ [482.17 g/mol]

^{1}H-NMR (300.36 MHz, CD$_2$Cl$_2$):δ 8.60 (s, 1H, 5), 8.45 (d, ^{4}J$_{HH}$= 2.1 Hz, 1H, 1), 8.37 (s, 1H, 4), 8.19 (d, ^{3}J$_{HH}$ = 8.2 Hz, 1H, 3), 7.95 (dd, ^{3}J$_{HH}$ = 8.2 Hz, ^{4}J$_{HH}$ = 2.1 Hz, 1H, 2), 7.83 (d, ^{3}J$_{HH}$ = 8.1 Hz, 1H, 6), 7.68 (d, ^{4}J$_{HH}$ = 1.8 Hz, 1H, 8), 7.59 (dd, ^{3}J$_{HH}$ = 8.2 Hz, ^{4}J$_{HH}$ = 1.8 Hz, 1H, 7), 1.58 (s, 6H, 9,10) ppm.

TLC: R$_f$=0.45 (CH/EE=4+1)

4.1.15 2,9-bis(diphenylamino)-13,13-dimethyl-6*H*-indeno-[1,2-b]-anthracene-6,11(13*H*)-dione

(15)
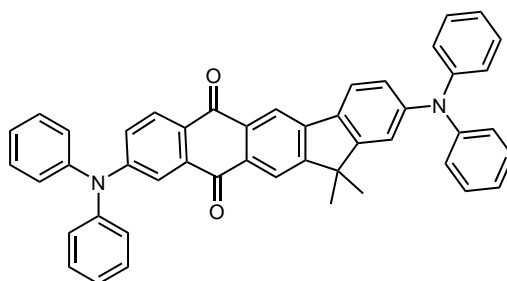
Figure 4.15: Structure of compound **15**

A flame dried and Ar flushed 25 ml Schlenk-tube was charged with 100.9 mg (209 µmol, 1 eq) **14**, 74.6 mg (441 µmol, 2.11 eq) diephenylamine, 66.6 mg (594 µmol, 2.84 eq) potassium *tert*-butoxide and 10.2 mg (15 µmol, 0.07 eq) PEPPSI™-IPr catalyst under inert conditions. The Schlenk was evacuated and Ar flushed (5 cycles). Then a flame dried and Ar flushed dropping funnel was attached and charged with 5 ml dry toluene under Ar counterflow. The toluene was degassed by purging with Ar for 10 min and then added to the reagents. The reaction mixture was then stirred for 2 min at room temperature and subsequently placed in a preheated oilbath at 100 °C. The dark red mixture was kept stirring until quantitative conversion of the antraquinone species was detected via TLC (CH/EE=4+1, Rf$_f$(E)=0.65, R$_f$(P)=0.61). The Schlenk was then allowed to cool down to room temperature before the reaction mixture was precipitated from 25 ml of a MeOH/H$_2$O=9+1 mixture. After centrifugation the collected crude product was purified via flash column chromatography (CH/DCM=1+1, R$_f$=0.4).

Yield: 130 mg (94 %), red solid

C$_{47}$H$_{34}$N$_2$O$_2$ [658.80 g/mol]

^{1}H-NMR (300.36 MHz, CD$_2$Cl$_2$):δ 8.46/8.40* (s, 1(0.35+0.65)H), 8.28/8.22 (s, 1H), 8.09 (d, J = 8.7 Hz, 1H), 7.80 – 7.66 (m, 2H), 7.40 (t, J = 7.8 Hz, 4H), 7.34 – 7.18 (m, 12H), 7.17 – 7.00 (m, 7H), 1.48/1.47 (s, 6(2+4)H, CH$_3$) ppm.
*probably two isomers, discussion of those shifts in the chapter "Results and Discussion".
MALDI TOF: *m/z*: [M + 2H]$^+$ (c.f. [59]) calc.: 660.28, found: 660.38

ε(toluene, λ_{max}\M^{-1}cm^{-1}): 384\44500, 457\21500

4.1.16 2,9-bis(bis(4-(2-phenylpropan-2-yl)phenyl)amino)-13,13-dimethyl-6*H*-indeno-[1,2-*b*]-anthracene-6,11(13*H*)-dione (16)

Figure 4.16: Structure of compound **16**

100.0 mg (207 µmol, 1 eq) **14**, 177.4 mg (437 µmol, 2.11 eq) bis(4-(2-phenylpropan-2-yl)phenyl)amine, 62.5 mg (557 µmol, 2.69 eq) potassium *tert*-butoxide and 11.2 mg (16 µmol, 0.08 eq) PEPPSI™-IPr catalyst were placed in a flame dried and Ar flushed 25 ml Schlenk-tube under inert conditions. After the evacuation and Ar flushing of the reaction Schlenk (5 cycles) 5 ml dry toluene degassed by purging with Ar for 10 min were added. The reaction mixture was stirred at room temperature for 1 min before it was placed in a preheated oil bath at 100 °C and kept stirring until quantitative conversion, monitored via TLC (CH/DCM=1+1, R$_f$(E)= 0.66, R$_f$(P)=0.65), was detected. The reaction mixture was allowed to cool down to room temperature and subsequently precipitated from 25

ml of a mixture of MeOH/H$_2$O=9+1. The crude product which was collected after centrifugation was purified via flash column chromatography (gradient elution starting from CH/DCM=3+1 to CH/DCM=1+1, detected via TLC: CH/DCM=3+1, R$_f$=0.33).

Yield: 157 mg (67 %), red solid.

C$_{83}$H$_{74}$N$_2$O$_2$ [1131.52 g/mol]

^{1}H-NMR (300.36 MHz, CD$_2$Cl$_2$):δ 8.43/8.38 (s, 1(0.35+0.65)H), 8.27/8.21 (s, 1H), 8.06 (d, J = 8.7 Hz, 1H), 7.72 (m, 2H), 7.35 – 6.98 (m, 39H), 1.71 (s, 12H), 1.69 (s, 12H), 1.48/1.47 (s, 6H) ppm.

MALDI TOF: *m/z*: [M + 2H]$^+$ (c.f. [59]) calc.: 1132.59, found: 1132.46

ε(toluene, λ_{max}\M^{-1}cm^{-1}): 390\39500, 471\18500

4.1.17 2,6-bis(3,6-di-*tert*-butyl-9*H*-carbazol-9-yl)anthracene-9,10-dione
(17)
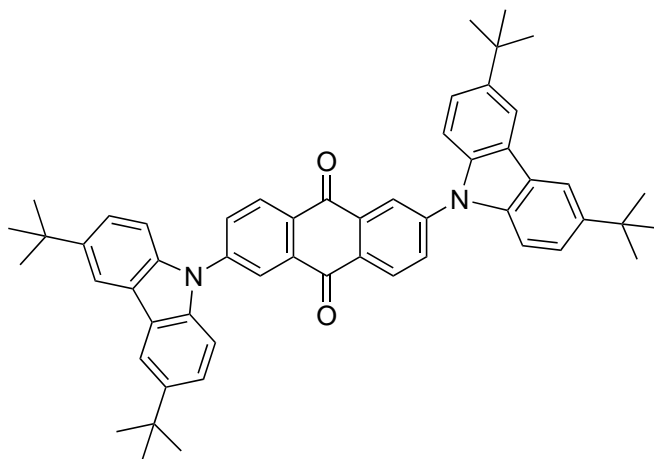
Figure 4.17: Structure of compound **17**

Procedure according to: Q. Zhang, H. Kuwabara, W. J. Potscavage, S. Huang, Y. Hatae, T. Shibata, C. Adachi, *Journal of the American Chemical Society* **2014**, *136*, 18070–18081.

A flame dried and Ar flushed 10 ml Schlenk-tube was charged with 75 mg 2,6-dibromoanthracene-9,10-dione (205 µmol, 1 eq), 121 mg 3,6-di-*tert*-butyl-9*H*-carbazole (433 µmol, 2.11 eq), 60 mg sodium *tert*-butoxide (624 µmol, 3.05 eq) and 8.6 mg PEPPSI™-IPr catalyst (13 µmol, 0.06 eq) under Ar counterflow. Then the Schlenk flask was evacuated and Ar flushed (5 cycles). After the addition of 3 ml degassed, dry toluene under inert conditions the reaction mixture was stirred for 1 min at room temperature and then placed in a preheated oilbath at 100 °C. The initially orange reaction mixture was kept stirring for 12 h at 100 °C and then allowed to cool down to room temperature. The brownish red mixture was then precipitated from a MeOH/H_2O mixture (MeOH/H_2O=9+1, 20 ml). After centrifugation the received, red solid was collected and dried in the drying oven at 60 °C. The crude product was purified via vacuum sublimation.

Yield: 28 mg (18 %), red solid.

$C_{54}H_{54}N_2O_2$ [763.04 g/mol]

^{1}H-NMR (300.36 MHz, $CDCl_3$):δ 8.62 (d, J = 2.2 Hz, 2H, Anq), 8.58 (d, J = 8.3 Hz, 2H, Anq), 8.18 – 8.14 (m, 4H, Carb), 8.08 (dd, J = 8.2, 2.2 Hz, 2H, Anq), 7.56 – 7.50 (m, 8H), 1.49 (s, 36H) ppm

TLC: R_f= 0.86 (CH/EE=4+1)

ε(toluene, λ_{max}\$M^{-1}cm^{-1}$): 342\13000, 463\6000

Analytical data are in accordance with those reported.

4.2 Sensor Material

The characteristics of the used polymers are to be found in section 3.1.

4.2.1 Polystyrene Foils (PS)

Dye "cocktails" with approximately 1 wt% dye with respect to the amount of PS (7 wt% dye+PS in $CHCl_3$) were knife coated (25 and 75 µm thick wet film) on dust-free PET support foils. After evaporation of the main part of the solvent (30 min), the foils were dried at 60 °C in a drying oven for 24 h.

4.2.2 Ormosil Foils

Approximately 4.5 mg of dye and 300 mg of poly(phenylsilsesquioxane) were dissolved in 3 g $CHCl_3$ using an ultrasonic bath. After removal of the solvent under nitrogen flow, the remaining solid was heated to 130 °C and kept at this temperature for 16 h. The received glassy solid was finely ground using a mortar. For the preparation of the sensor foils, a "cocktail" was made from approximately 100 mg of the received powder, 200 mg silicone E43 and 1 g $CHCl_3$ and then knife coated (75 µm) on dust free PET support foils. The foils were dried at room temperature for at least 24 h.

4.2.3 Poly(vinylidene chloride-co-acrylonitrile) Foils ("PVCAN")

Dye cocktails with approximately 1 wt% dye with respect to the amount of poly(vinylidene chloride-co-acrylonitrile) (10 wt% dye+PS in dry THF) were knife coated (25 and 75 µm thick wet film) on dust-free PET support foils under inert conditions (glovebox). After evaporation of the solvent (1 h) the foils were retrieved from the glove box and dried in the drying oven at 60 °C for another 24 h.

4.2.4 Ethylcellulose Foils (EC)

Dye cocktails with approximately 1 wt% dye with respect to the amount of EC (5 wt% dye+EC in THF) were knife coated (25 and 75 µm thick wet film) on dust-free PET support foils. After evaporation of the main part of the solvent (30 min), the foils were dried at 60 °C in a drying oven for 24 h.

4.2.5 Poly(styrene-*co*-acrylonitrile) Foils ("PSAN")

Dye cocktails with approximately 1 wt% dye with respect to the amount of PSAN (7 wt% dye+PSAN in $CHCl_3$) were knife coated (25 and 75 µm thick wet film) on dust-free PET support foils. After evaporation of the main part of the solvent (30 min), the foils were dried at 60 °C in a drying oven for 24 h.

4.2.6 Silicone E43 Foils

Dye cocktails with approximately 1 wt% dye with respect to the amount of silicone E43 (15 wt% dye+silicone E43 in CH_2Cl_2) were knife coated (25 and 75 µm thick wet film) on dust-free PET support foils. The foils were dried at room temperature.

5 Results and Discussion

5.1 Synthetic Considerations

5.1.1 Anthraquinone Based Dyes
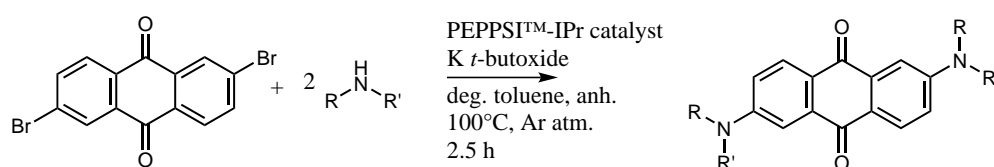
Figure 5.1: Reaction scheme for the synthesis of 2,6-bis(diarylamino)anthraquinones via Buchwald-Hartwig amination.

The intention was to synthesize a series of anthraquinone based dyes with varying substituents and to investigate the influence of the substition on the photophysical properties.

The starting reaction for all anthraquinone dyes, depicted in figure 5.1, was a double Hartwig-Buchwald amination of 2,6-dibromoanthraquinone analogously to literature [13]. Instead of sodium *tert*-butoxide, potassium *tert*-butoxide was used, as conversion appeared (comparison via reaction control by TLC) to be faster and due to its better solubility in organic solvents. Reaction control via TLC was, however, a bit misleading, as parts of 2,6-dibromoanthraquinone, not only stained its own spot, but also blended the product spots, noticeable by comparison of UV detection at 254 and 366 nm. Purification was done in general by precipitation and flash column chromatography, which has proved challenging, due to the poor solubility of educts and products. Sometimes vacuum sublimation was necessary to remove unreacted 2,6-dibromoanthraquinone, which could be sublimed off.

The improvement of reaction conditions and work up procedure, although lacking refinement, has not been of special importance as the reactions worked sufficiently well for subsequent characterization of the synthesized dyes. Therefore the yields are lower than those described in literature[13].

The bromination of some dyes was intended to, on the one hand increase spin-orbit

coupling (due to Br as a heavy atom) and on the other hand to introduce a handle for functionalization or further coupling reactions. At first the amount of bromine was measured volumetrically, which lead to product mixtures of various times brominated species. The reaction, however, worked smoothly, when the amount bromine to be added was measured gravimetrically. Satisfying MS-spectra of the brominated species are still to be obtained, previously used matrix materials resulted in poor ionisation and miserable spectra.

The tetrabrominated compound **5** was used as an educt in a Suzuki coupling with (9,9-dimethyl-9*H*-fluoren-2-yl)boronic acid. The reaction gave the desired product, but MS shows a contaminant that could not be removed with flash column chromatography and that could not be seen by TLC and by NMR spectroscopy only to a negligible extent. Therefore the origin and the identity of this contaminant remains unclear.

A few attempts were made to synthesize products with mixed substitution for generation of intermediate properties. When choosing a one pot reaction approach with two different amines, according to NMR after separation, preferentially the symmetrical products have formed (figure 5.2). Also doing a stepwise substitution did not work. As indicated by MS, a product formed, where one bromine was substituted with an amine and the other one with the used base, *tert*-butoxide (figure 5.3). As these attempts also proved to be time consuming, the goal of mixed substitution was abandoned.

Another idea for systematic investigation of these class of dyes was to also vary the
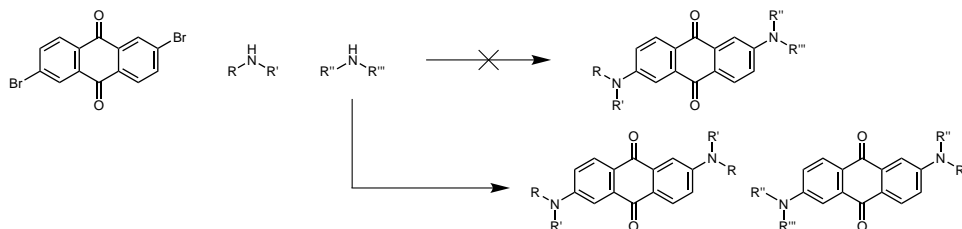
Figure 5.2: Reaction scheme for the synthesis of asymmetrically substituted products via a one pot reaction.

core structure by using some other anthraquinone derivatives (figure 5.4) for variation of the size of the π-system. Here 2-bromo-13,13-dimethyl-6*H*-indeno[1,2-*b*]anthracene-6,11(13*H*)-dione (**23**) as a commercially available starting material and 2,9-dibromo-13,13-dimethyl-6*H*-indeno-[1,2-*b*]-anthracene-6,11(13*H*)-dione (**14**) from own synthesis were used.

The synthesis of compound **14** was done via Friedel-Craft acylation and subsequent ring closure/condensation with polyphosphoric acid. As illustrated in 5.5, the reaction gives two isomers, depending on the orientation of the 5-bromoisobenzofuran-1,3-dione
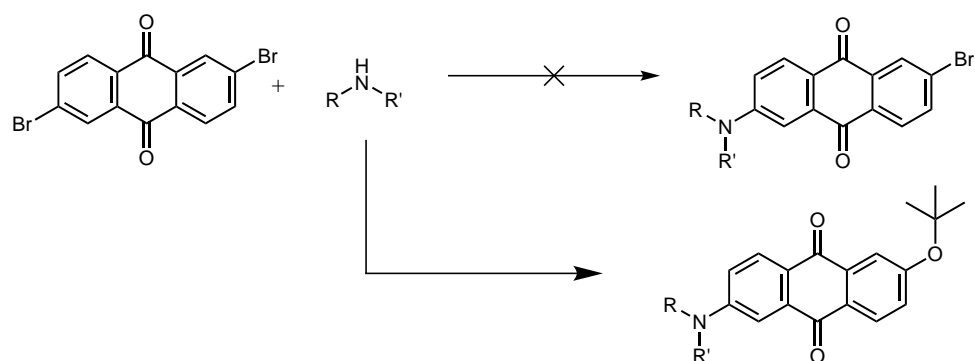
Figure 5.3: Reaction scheme for the first substitution for the synthesis of asymmetrically substituted products.
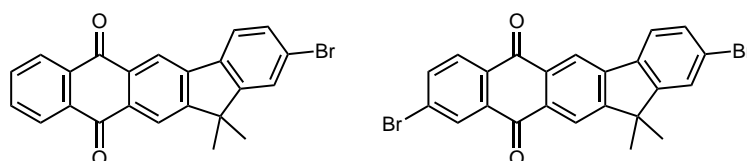
Figure 5.4: Structures of the used anthraquinone derivatives, **23** and **14**, respectively.

during acylation, which could be seperated after ring closure either by flash column chromatography or by trituration with $CHCl_3$ as the solubility of the two isomers vary substantially (**14**a less soluble in $CHCl_3$).

The synthesis was done according to a patent[60], but with adjustments. The amount
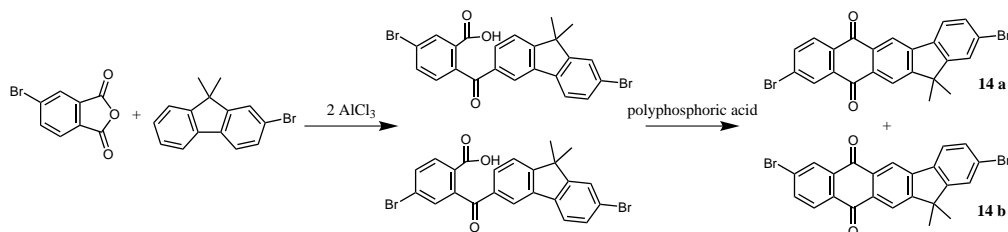
Figure 5.5: Reaction scheme for the synthesis of compound **14**.

of used $AlCl_3$ was increased from 1.5 to 2 eq, as a second equivalent binds to the formed carbonic acid[61]. The purification was changed from sole washing with methanol to flash column chromatography/trituration with $CHCl_3$ as two isomers formed, one yellow (main product) and one red solid, which was not mentioned in the patent. To determine the structure of the isomer used for further synthesis (the "yellow one" was used), the crystallisation of the two isomers and the crystallisation of the reaction products was attempted. A crystal structure co-crystallized with acetone from compound **15** (figure 5.6) was received and indicates the structure shown in figure 5.5, compound **14**a, for the main product received during the synthesis of **14**. The NMR (^{1}H, APT and HSQC) of

15 (and also compound **16**), however, displays two sets of peaks in a ratio 0.35+0.65 indicating again two isomers, however, as such a double set of peaks cannot be found in the proton NMR of the educt, it can be assumed that no position isomerism is involved. A possible explanation would be conformational isomerism, with different conformations of the two diphenylamine substituents relative to each other. This could be further investigated with temperature dependent NMR measurements.

When the matrix dithranol was used, in some of the measured MS-spectra, the
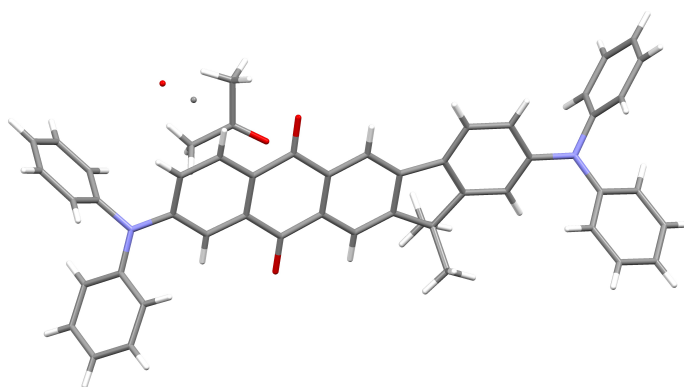
Figure 5.6: Crystal structure of compound **15** with aceton.

molecules appear as pseudomolecular ions in the form $[M+2H]^+$. This behaviour is known to occur among anthraquinones according to [59].

5.1.2 Dicyanobenzene Based Dyes

The idea for the synthesis of compound **2** was to increase the moderate solubility of **20** by use of 3,6-di-*tert*-butyl-9*H*-carbazole instead of carbazole. Compound **20** or actually the *ortho*-substituted core structure was chosen for modification, as it displays the longest lifetime of the three isomers (**18**, **18** and **20**), considering the latter investigation for the suitability as an oxygen sensor. The nucleophilic substition of tetrafluorophthalonitrile worked fine, but for purification simple flash column chromatography alone was not sufficient, as it could not remove excess 3,6-di-*tert*-butyl-9*H*-carbazole. The excess carbazole, however, could be removed by vacuum sublimation. Similar to the synthesis of **20** stated by literature, only a rather moderate yield (33 %) was obtained.
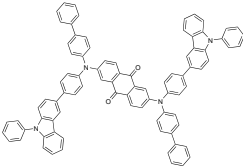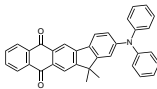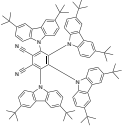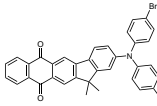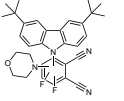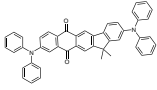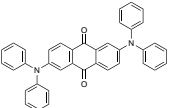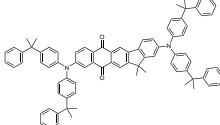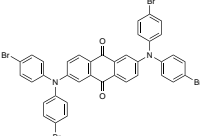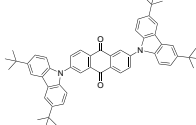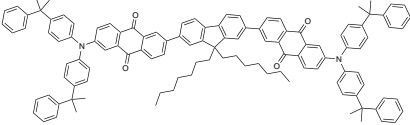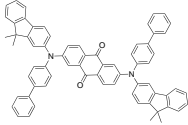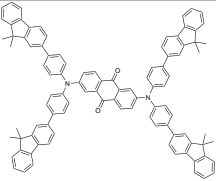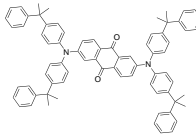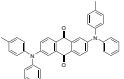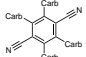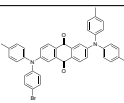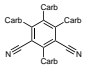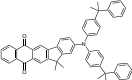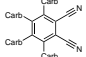
The intention behind the synthesis of compound **3** was to increase the moderate molar absorption coefficient of the tetracarbazole substituted phthalonitrile (around 25.000

$M^{-1}cm^{-1}$), by the replacement of one or more carbazole substituents with morpholine as the four times morpholine substituted phthalonitrile is characterized by a high molar absorption coefficient. The synthesis of **3** was characterized by poor experimental execution as the product of the nucleophilic substitution of tetrafluorophthalonitrile with the carbazole was used in the subsequent nucleophilic substitution with morpholine without further purification. This approach resulted in a wide product mixture with poor yield. NMR and MS measurement indicated that the isolated product has one morpholine and one 3,6-di-*tert*-butyl-9*H*-carbazole substituent. The exact structure could not be determined so far as crystallisation attempts have not been successful.

5.2 Dye Characterisation

In table 5.1 all the dyes that have been characterised are listed and their structures, compound numbers and assigned names for further discussion are shown.

Table 5.1: List of characterized dyes.

Structure	No.	Name	Structure	No.	Name
	1	BPhPhCarbAAnq		**12**	DiPhAkA
	2	TDTBCP		**13**	DiBrDiPhAkA
	3	CDiFMP		**15**	DiPhAkAnq
	4	DiPhAAnq		**16**	DiPhMe2PhAkAnq
	5	TBrDiPhAAnq		**17**	DiTBCarbAnq
	7	Oligo		**22**	DiFlBPhAAnq
	8	TFlDiPhAAnq		**21**	DiPhMe2PhAAnq
	9	oTPhAAnq		**18**	pTCP
	10	DiBroTPhAAnq		**19**	mTCP
	11	DiPhMe2PhAkA		**20**	oTCP

5.2.1 Photophysical Properties

In table 5.2 the photophysical properties of all dyes dissolved in toluene are summarized. The individual results are discussed in the corresponding subchapters below.

Table 5.2: Photophysical properties of all dyes in toluene at room temperature. (sh = shoulder)

dye	Abs. $\lambda_{max}[nm]\backslash\varepsilon$(tol, $M^{-1}cm^{-1}$)	Em. $\lambda_{max}[nm]$	τ_{TADF} [s]	$\Phi_F\backslash\Phi_{TADF}\backslash\Phi$ [%]
BPhPhCarbAAnq (**1**)	327\92500, 380\37500, 470\23500	676	n.d.	0.1\0\0.1
DiPhAAnq (**4**)	370\34000, 448\23000	618	5,81E-4	7\3\11
TBrDiPhAAnq (**5**)	370\34000, 448\23000	609	3,34E-4	6\9\15
Oligo (**7**)	379\20000, 492\4500	669	5,83E-4	3\0.4\3
TFlDiPhAAnq (**8**)	345\62000, 472\13000	678	4,65E-5	1\0.1\1
oTPhAAnq (**9**)	373\27000, 453\19000	631	2,45E-4	5\2\6
DiBroTPhAAnq (**10**)	373\26500, 452\18000	625	1,23E-4	5\3\7
DiTBCarbAnq (**17**)	342\13000, 463\6000	617	1.06E-5	3\3\6
DiFlBPhAAnq (**22**)	334\73000, 383\37000, 473\25000	667	5,74E-5	1\0.2\2
DiPhMe2PhAAnq (**21**)	375\30000, 457\21000	651	1,40E-4	4\1\5
DiPhMe2PhAkA (**11**)	389\23000, 485\9000	628	7.28E-6	15\18\33
DiPhAkA (**12**)	382\23000, 466\9200	614	6.47E-6	19\14\33
DiBrDiPhAka (**13**)	337\26500, 383\26000, 466\9500	611	7.90E-6	13\9\23
DiPhAkAnq (**15**)	384\44500, 457\21500	612	3.04E-5	12\5\17
DiPhMe2PhAkAnq (**16**)	390\39500, 471\18500	650	3.63E-5	6\1\6
TDTBCP (**2**)	383\24500, s450	546	7,86E-6	11\50\61
CDiFMP (**3**)	366\11000	519	3,21E-4	9\27\35
pTCP (**18**)	322\13000, 335\12000, 460\1200, 490(sh)	537	2,85E-6(73) 1,88E-5(27)	23\50\73
mTCP (**19**)	326\14000, 377\15000, 445(sh)	506	5,00E-6	23\56\78
oTCP (**20**)	326\15000, 371\16000, 430(sh)	528	1,55E-5	11\57\68

Absorption- and Emission Spectra

Dicyanobenzene based dyes

When comparing the absorption spectra of the dicyanobenzene dyes to each other, **18** stands out with properties different from all others. **18** displays the smallest Stokes shift with around 40 nm, the smallest molar absorption coefficient of the peak near the VIS-region and a different overall structure of the spectrum. These compounds in general possess only mediocre to poor molar absorption coefficients ranging from 11000 (**3**) to 24500 (**2**). The molar absorption coefficient of **20** is strangely by a factor of 10 lower than that stated by literature[12], which could be erroneous, because the data within the series of dicyanobenzene based dyes is consistent. The intention to increase the molar absorption coefficient by morpholine substitution (**3**) failed, even resulting in a decrease. This decrease may be due to the lower extent of substitution (two times substituted **3** compared to 4 times substituted **2**, **19** and **20**) The additional *tert*-butyl groups in **2**

compared to **20** resulted in a bathochromic shift, with the *t*-Bu groups increasing the electron donating abilities of the peripheral carbazolyl groups[12].
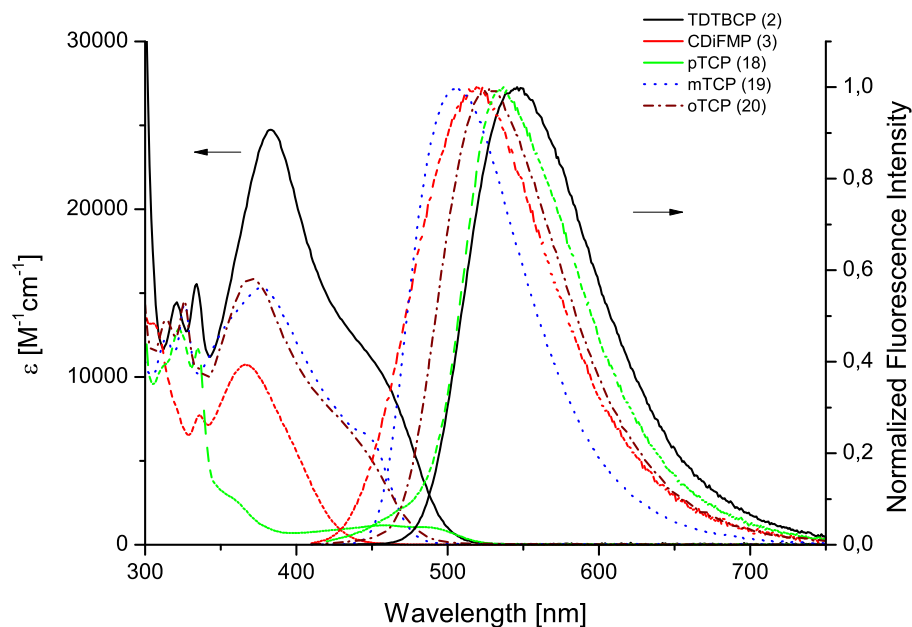
Figure 5.7: Absorption and emission spectra of the diycanobased dyes in toluene at room temperature.

Anthraquinone based dyes

All the anthraquinone based dyes share a similar overall structure of their absorption spectra (figures 5.8, 5.9, 5.10) with two distinct peaks, that only are slightly distorted in **7** and **17**. The Stokes shift of these dyes is generally very large and around 160 nm. The spectra are increasingly bathochromically shifted with increasing size of the π-system from emission at 618 nm by diphenylsubstituted compound **4** to emission at 676 and 678 nm by compounds **1** and **8**. In contrast, bromination shifts the spectra hypsochromically by about 2-3 nm per added bromine (c.f. **4/5** and **9/10**).

The variation of the core structure (c.f. figure 5.11) has nearly no influence on the emission spectrum and results in an only minor bathochromic shift of the absorption specrum with increasing size of the π-system. Molar absorption coefficients are decreased in the single amine-donor substituted compounds **11**, **12** and **13**, compared to the doubly-substituted compounds.
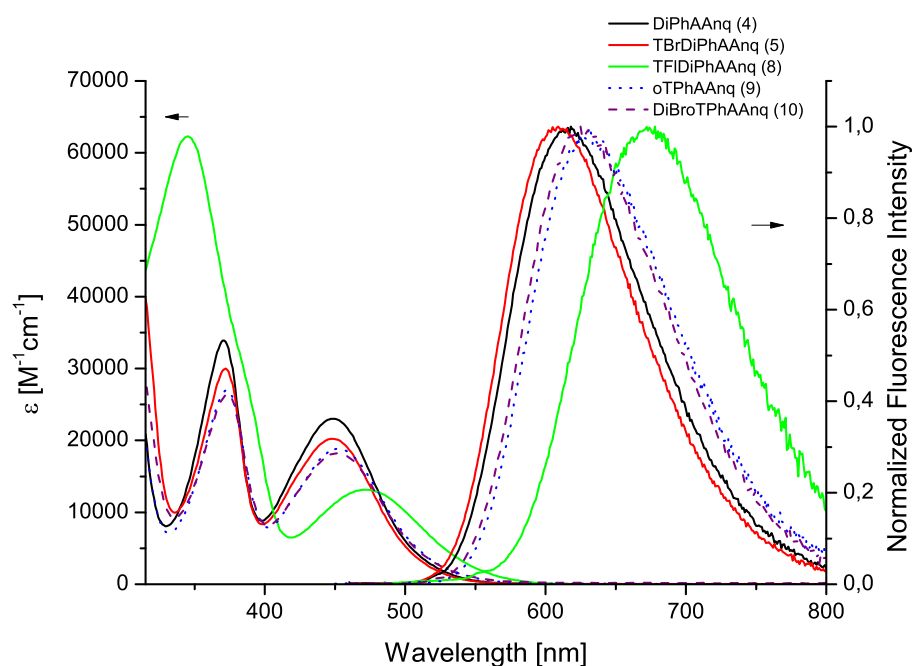
Figure 5.8: Absorption and emission spectra of the anthraquinone based dyes in toluene at room temperature.
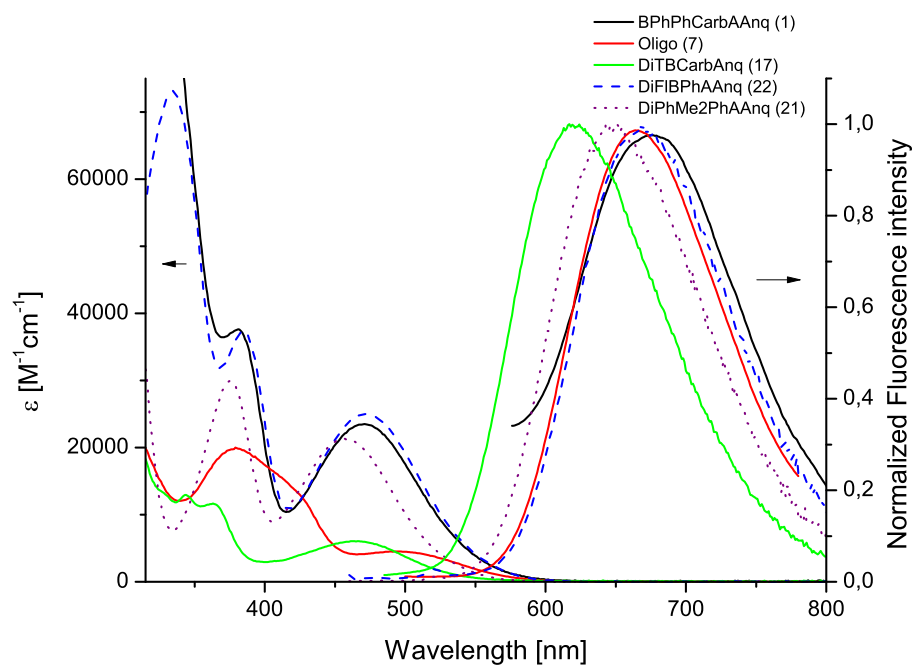
Figure 5.9: Absorption and emission spectra of the anthraquinone based dyes in toluene at room temperature.
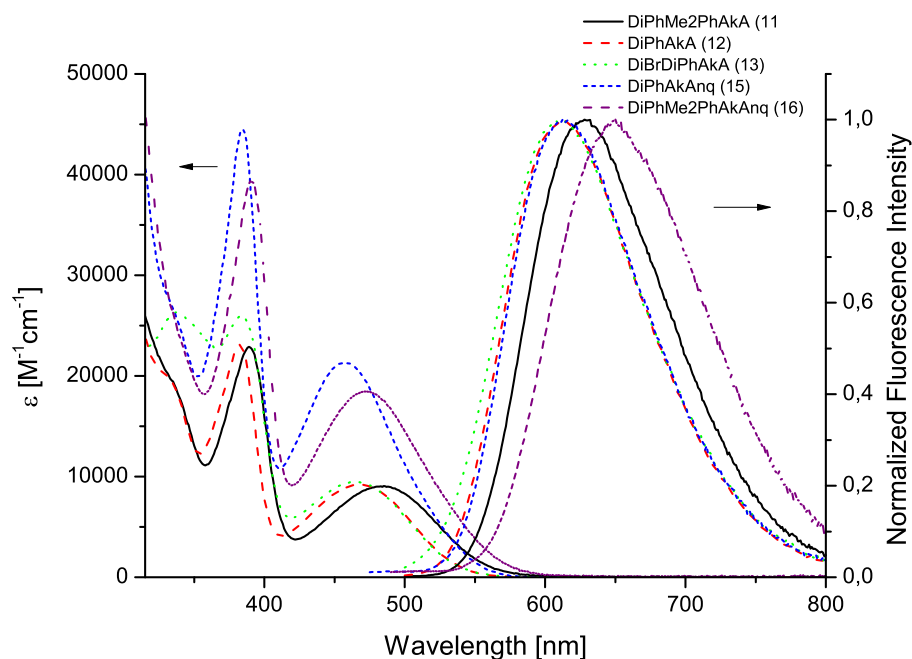
Figure 5.10: Absorption and emission spectra of the anthraquinone based dyes (condensed anthraquinones) in toluene at room temperature.
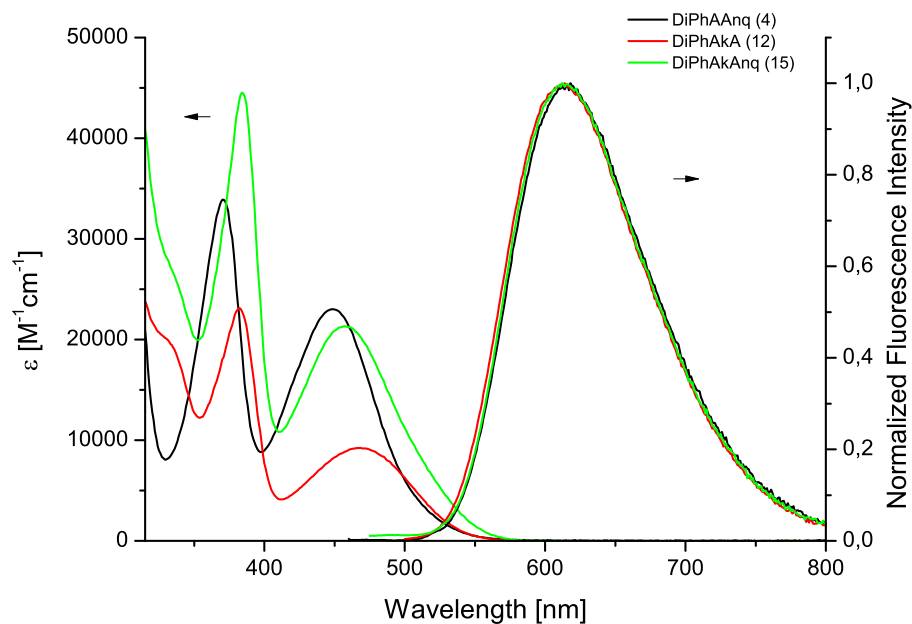
Figure 5.11: Absorption and emission spectra of the diphenylamine substituted anthraquinone based dyes in toluene at room temperature.
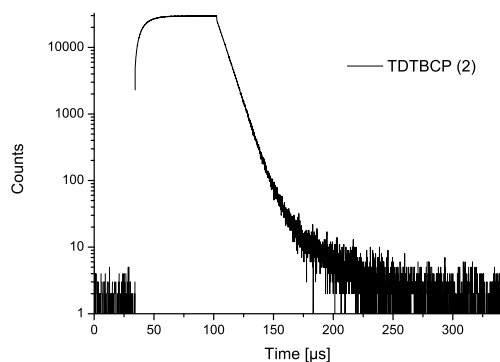
Figure 5.12: Decay curve of **2** in toluene at room temperature.
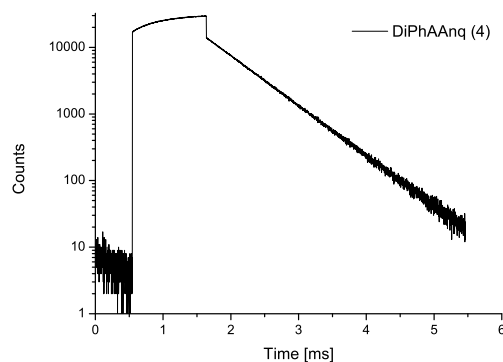
Figure 5.13: Decay curve of **4** in toluene at room temperature.
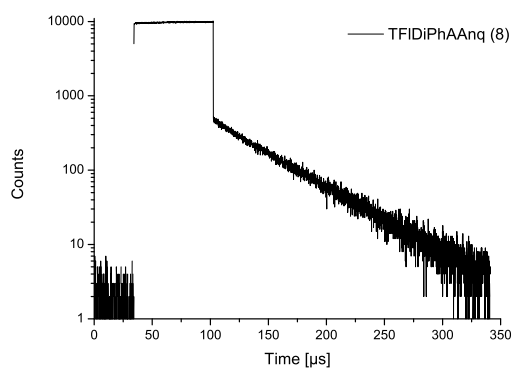
Figure 5.14: Decay curve of **8** in toluene at room temperature.
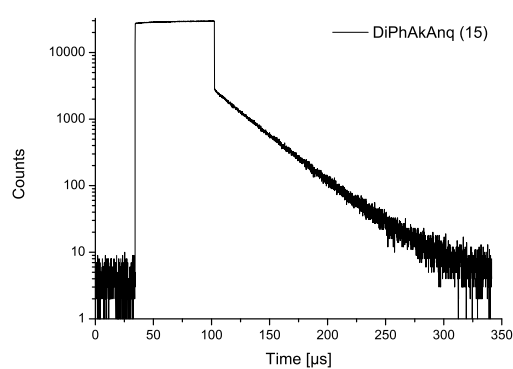
Figure 5.15: Decay curve of **15** in toluene at room temperature.

TADF Lifetimes

All the dyes apart from **18** display a monoexponential decay in solution (with representative decay curves depicted in figures 5.12, 5.13, 5.14 and 5.15). The decay curve of **18** could not be fitted with a monoexponential function. Considering the poor solubility of this dye and the compared to the other dicyanobased dyes different shape of the absorption spectra, this may indicate aggregation.

Dicyanobenzene based dyes

The dicyanobenzene based dyes except **3** possess lifetimes in the low µs region. The morpholine substitution of **3**, which does not increase the molar absorption coefficient, however, greatly increases the lifetime by a factor of about 100. When comparing **20** and **2**, the lifetime decreases two-fold with the additional *t*-Bu groups. This could be reasoned by the increased number of possible non-radiative deexcitation pathways by increasing molecule size.

Anthraquinone based dyes

The lifetimes of the anthraquinone based dyes vary over a wide range from around 6 µs in **12** to around 580 µs in **4**. However no clear trends affecting all different anthraquinone core structures can be seen. In the group of the basic anthraquinone lifetime decreases with increasing size of the molecule (c.f. 580 µs for **4** to 140 µs for **21**) and with increasing bromination (c.f. 580 µs/335 µs for **4/5** and 245 µs/123 µs for **9/10**). These trends could be reasoned by the increased spin-orbit coupling by bromination, which would increase k_{RISC} and again by the raising the number of possible non-radiative deexcitation pathways by increasing molecule size. The trends, however, reverse when looking at the dyes base on other anthraquinone bodies(e.g. **11** and **15**). This reversal may be due to the decrease of symmetry, when using the condensed anthraquinones. The decrease may result in an entirely different electronic situation and therefore another starting point for discussion.

Quantum Yields

Dicyanobenzene based dyes

When looking at the quantum yields, the dicyanobenzene based dyes, seem to have much higher rate constants for (reverse) intersystem crossing k_{ISC}/k_{RISC} and radiative

deexcitation by k_F than for the non radiative k_{nr} deexcitation pathways. This results in high quantum yields even in solution, but still increasing molecule size seem to lower the quantum yields by increasing non-radiative deactivation (c.f. **20** and **2**). The obtained quantum yields for **18** (73/lit. 72) and **20** (68/lit. 74) also compare well to those stated in literature[12].

Anthraquinone based dyes

The anthraquinone based dyes seem to be much more prone to deexcitation by collisions with solvent molecules than the dicyanobenzene based dyes. Again this effect seems to even more pronounced for the larger dyes. Bromination leads to a distinct increase in Φ_{TADF} for **5** compared to **4**. The increased Φ_{TADF} of **10** compared to **9**, however, is not so distinct, as it lies within the typical error of quantum yields. For the condensed anthraquinone dyes no clear trend can be stated, except that they have significantly higher quantum yields than the dyes based on simple anthraquinone.

5.3 Sensor Characterisation

After the basic dye characterisation in solution, all dyes were incorporated into polystyrene and those with the smaller lifetimes (the dicyanobenzene based dyes) were also incorporated into ormosil (organically modified silica) and silicone rubber matrices. Ormosil and silicone matrices were chosen with oxygen sensing in mind, to increase the sensitivity by using these two more oxygen permeable matrices compared to PS.

5.3.1 Photophysical Properties

Excitation- and Emission Spectra

Compared to the dyes in solution, the emission peaks are considerably blue shifted when the dyes are incorporated into polymer matrices. In literature[13] this is explained, by the lacking stabilisation of the excited states by reorganisation of surrounding molecules. The trends within the series of dyes regarding their excitation and emission spectra are analogous to those (bromination, size of π-system) of the dyes in solution. The chosen anthraquinone body (anthraquinone/condensed anthraquinone) now also affects the emission wavelength. Those dyes based on the condensed anthraquinone are bathochromically shifted.
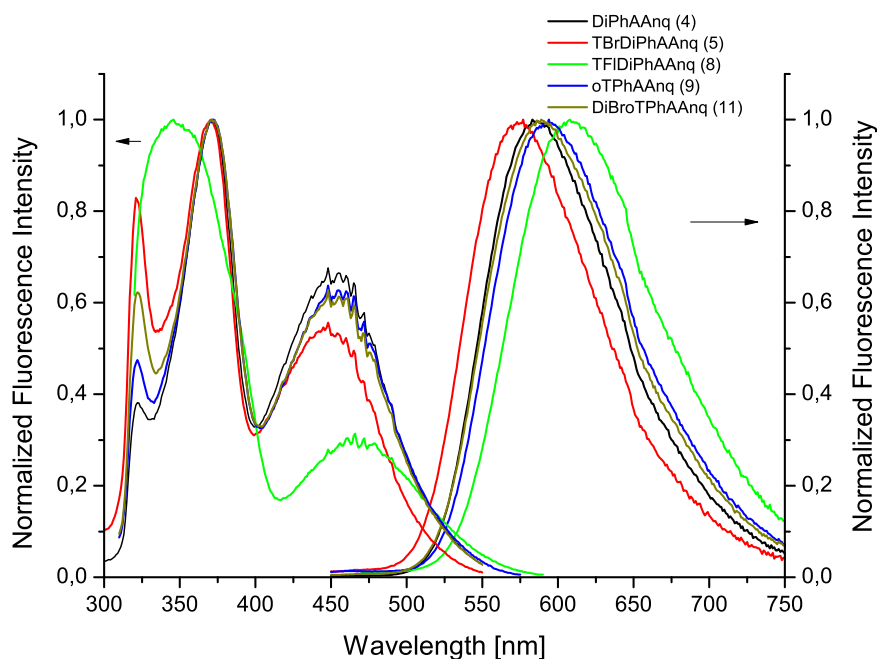
Figure 5.16: Excitation and emission spectra of the anthraquinone based dyes in polystyrene at room temperature.
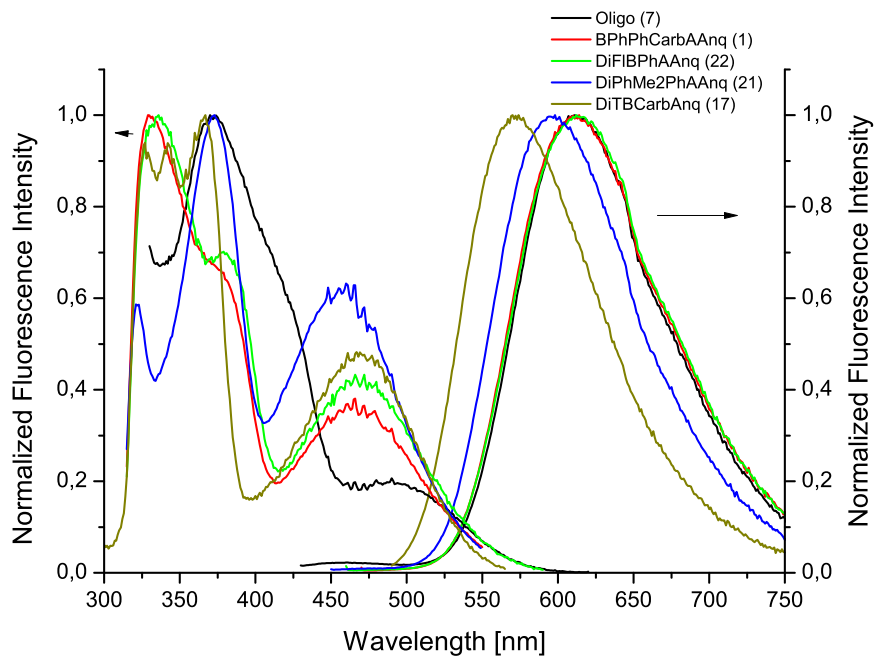
Figure 5.17: Excitation and emission spectra of the anthraquinone based dyes in polystyrene at room temperature.
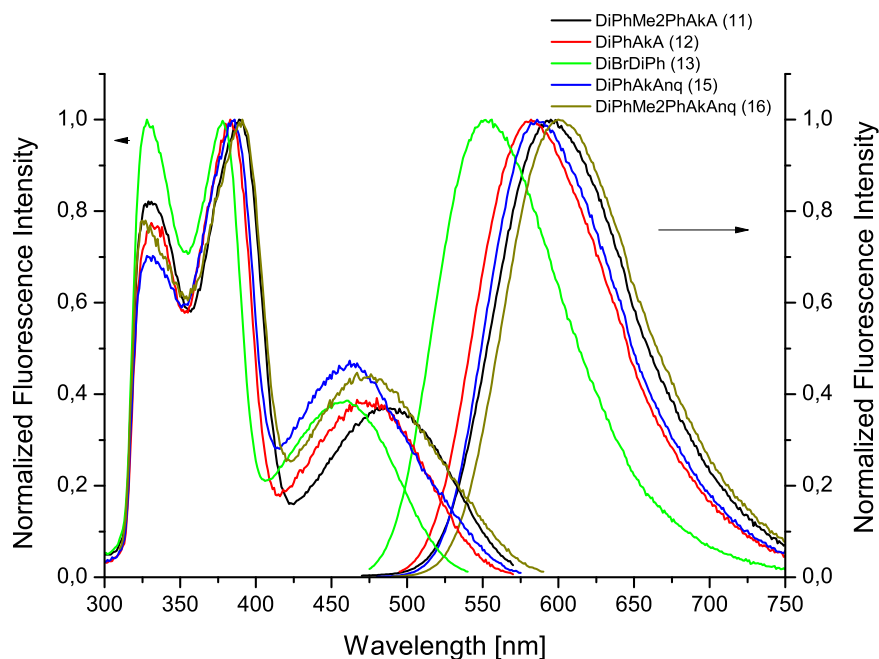
Figure 5.18: Excitation and emission spectra of the anthraquinone based dyes (condensed anthraquinones) in polystyrene at room temperature.
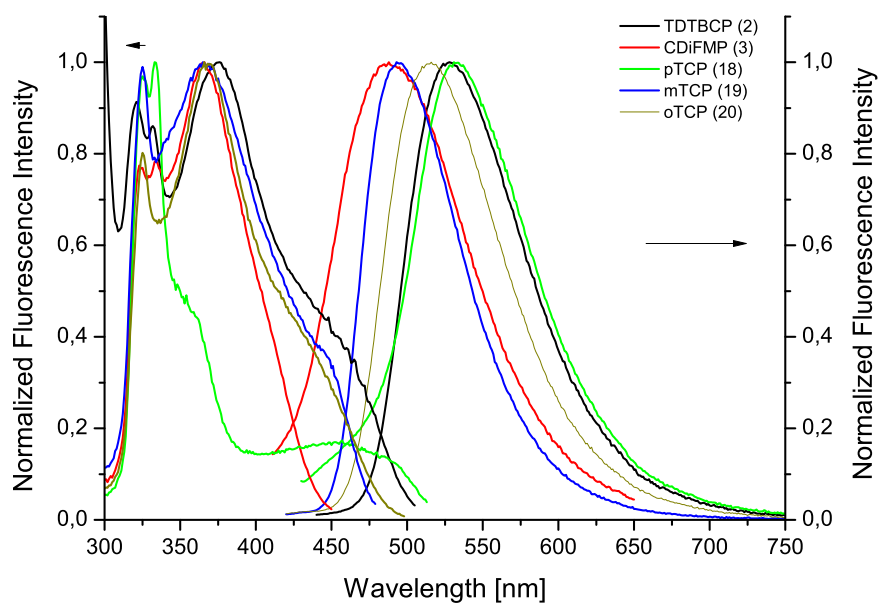
Figure 5.19: Excitation and emission spectra of the dicyanobenzene based dyes in polystyrene at room temperature.
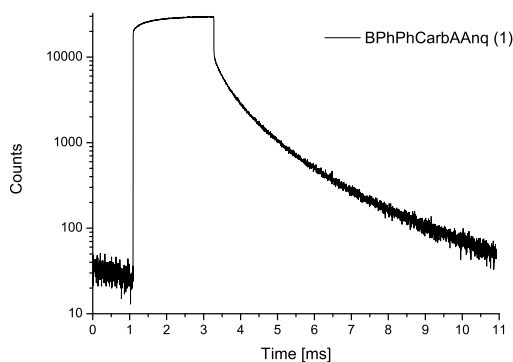
Figure 5.20: Decay curve of **1** in polystyrene at room temperature.
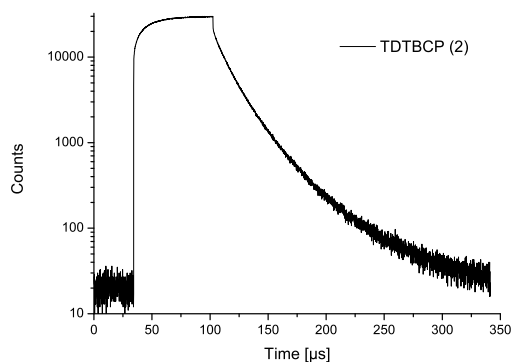
Figure 5.21: Decay curve of **2** in polystyrene at room temperature.
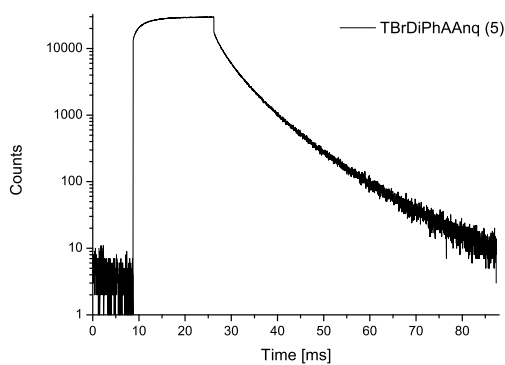
Figure 5.22: Decay curve of **5** in polystyrene at room temperature.
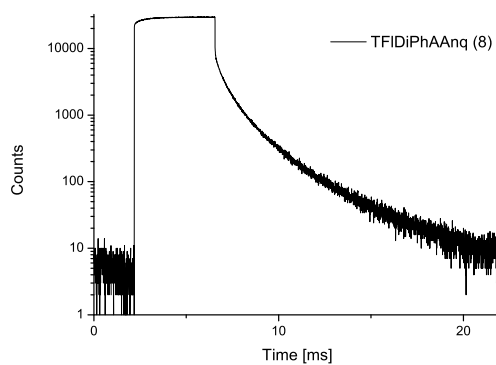
Figure 5.23: Decay curve of **8** in polystyrene at room temperature.

Table 5.3: Summarizing table of the photophysical properties of all dyes incorporated into a polystyrene matrix. (sh = shoulder)

dye	Abs λ_{max} [nm]	Em λ_{max} [nm]	av. τ_{TADF} [s]	$\Phi_F \backslash \Phi_{TADF} \backslash \Phi$ [%]
BPhPhCarbAAnq (**1**)	329, 466	614	9.73E-4	11/15/26
DiPhAAnq (**4**)	372,455	583	5.56E-3	8/38/46
TBrDiPhAAnq (**5**)	371,448	577	4.82E-3	7/41/48
Oligo (**7**)	370, s490	611	2.82E-3	21/5/26
TFlDiPhAAnq (**8**)	346, 466	608	1.37E-3	11/18/29
oTPhAAnq (**9**)	372, 455	594	2.83E-3	8/27/35
DiBroTPhAAnq (**10**)	371, 448	589	2.92E-3	7/28/35
DiTBCarbAnq (**17**)	367, 470	577	4.20E-5	15/28/42
DiFlBPhAAnq (**22**)	336, 466	612	1.20E-3	11/21/33
DiPhMe2PhAAnq (**21**)	373, 460	598	2.84E-3	8/26/34
DiPhMe2PhAkA (**11**)	390, 487	596	1.72E-3	64/9/73
DiPhAkA (**12**)	383, 475	588	1.92E-3	66/9/75
DiBrDiPhAka (**13**)	330, 377, 458	560	2.43E-3	72/13/85
DiPhAkAnq (**15**)	384, 461	599	9.84E-4	19/53/72
DiPhMe2PhAkAnq (**16**)	390, 471	611	7.54E-4	21/40/61
TDTBCP (**2**)	375, 455(sh)	528	2.09E-5	40/53/93
CDiFMP (**3**)	366	488	1.12E-2	17/15/32
pTCP (**18**)	333, 455(sh)	531	1.72E-5	38/21/58
mTCP (**19**)	365, 450(sh)	493	8.63E-6	58/38/96
oTCP (**20**)	366, 440(sh)	516	3.99E-5	33/54/87

TADF Lifetimes

Incorporated into polymer matrices the decay curves cease to have monoexponential form, but now display a biexponential form (with representative decay curves depicted in figures 5.20, 5.21, 5.22 and 5.23). This may arise from the microheterogeneous environment in the rigid polymers, which can lead to the entrapment of (two) different rotamers[13]. The rigid matrix also greatly increases the lifetime of the dyes (by a factor of 10) as deactivation pathways involving collisions with surrounding molecules are no longer feasible[16]. The trend stated for the brominated dyes in solution is no longer visible for the dyes incorporated into foils.

Quantum Yields

The quantum yields are as well greatly increased by the rigid polymer matrices, again due to the collision-free environment. The quantum yields of Φ_{TADF} are still raised by increased spin-orbit coupling caused by bromination, but the effect is much less pronounced than in solution. Especially **2** stands out with a superb quantum yield (93 %), but also the other dyes display reasonable quantum yields. The use of the condensed anthraquinones (compounds **11/12/13** and **15/16**) resulted in a distinct increase of the overall quantum yields for those dyes. The monosubstituted compounds

11, **12** and **13** display a significant increase of the quantum yield of prompt fluorescence, but only a minor quantum yield of TADF. In contrast, the disubstituted dyes with the condensed anthraquinone body **15** and **16** also display an increase in the quantum yield of TADF compared to the dyes based on anthraquinone.

5.3.2 Oxygen Calibration

As the decay curves of the sensor foils possess a biexponential form, the oxygen calibrations were done performing intensity based measurements. The "two lifetimes" of the sensor foils being in the same magnitude render simple frequency domain based measurements with standard equipment unsuitable. For fitting of the oxygen calibration data the two-site model[17] for microheterogeneous systems (equation 5.1) was used.

$$\frac{I}{I_0} = \frac{f}{1 + K_{SV}^1 pO_2} + \frac{1 - f}{1 + K_{SV}^1 * m * pO_2} \tag{5.1}$$

As starting values for fitting $K_{SV}^1 = 0.1$, $f = 0.5$ and $m = 0.05$ (K_{SV}^1, f, $m > 0$) have been chosen. Fits were done using *python* with a modified *lmfit* module (*pHfit* by Christoph Staudinger).

In the Stern-Volmer plots, it can be seen, that the characterized dyes cover a wide range of sensitivity (fit parameters in table 5.4) from less sensitive dyes in figure 5.24, over dyes with intermediate sensitivity in figure 5.25 to a set of dyes very sensitive towards oxygen in figures 5.26 and 5.27.

Already during calibration it could be seen that **3** displays only poor photostability (c.f. slope of plateaus in figure 10.44).

For compound **2** incorporated into PS, ormosil and silicone a strange result of the calibrations was found. In contrast to expectations the most sensitive sensor foil was the PS one (figure 5.28), although PS has the smallest oxygen permeability of the three used matrices. To further investigate these controversial results, **2** was incorporated into three other polymer matrices of varying oxygen permeability (ethyl cellulose, poly(styrene-*co*-acrylonitrile) and poly(vinylidene chloride-*co*-acrylonitrile)). The additional results, however, indicate that ormosil and silicone are unsuitable matrices for **2** as the additional sensor foils display the expected behaviour with the ethyl celluose being most sensitive and decreasing sensitivity from PS, over PSAN to PVCAN. These results are in agreement with the decreasing oxygen permeability of the polymers (c.f. table 2.2). The reason for this behaviour of **2** in ormosil and silicone E43 has not been further investigated.
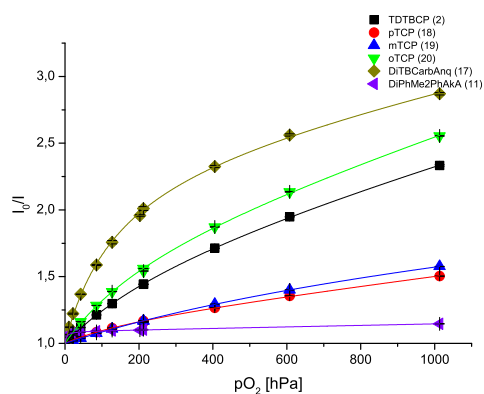
Figure 5.24: Stern-Volmer plots of the least sensitive sensors.
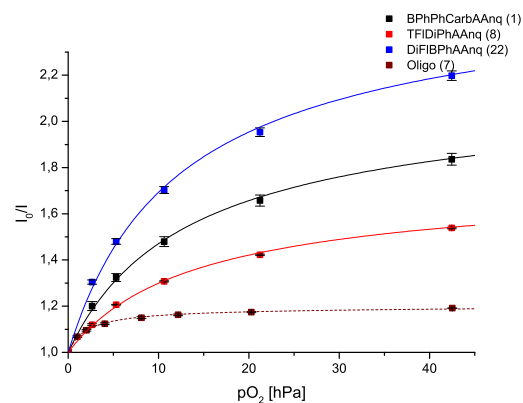
Figure 5.25: Stern-Volmer plots of the intermediately sensitive sensors.
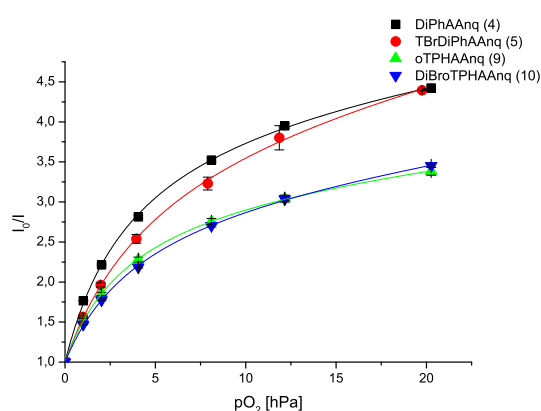
Figure 5.26: Stern-Volmer plots of the sensitive sensors.
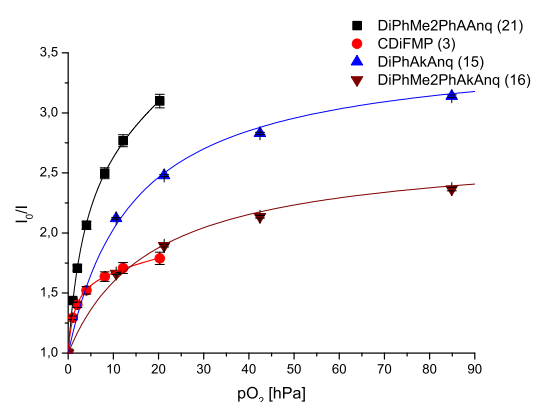
Figure 5.27: Stern-Volmer plots of the sensitive sensors.
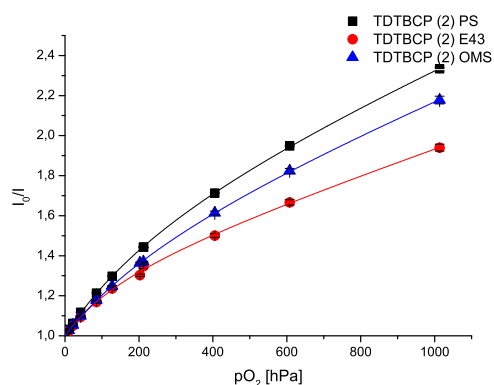
Figure 5.28: Unexpected behaviour of the oxygen sensitivity of dye **2** in different polymer matrices of varying oxygen permeability.
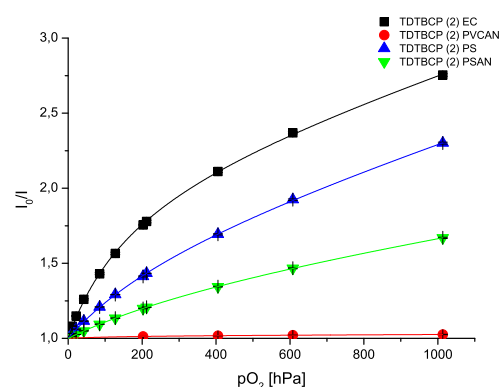
Figure 5.29: Comparison of the oxygen sensitivity of **2** in different polymer matrices.

Table 5.4: Calculated SV-Fitting Parameter of the oxygen of all dyes incorporated into PS.

dye	$K_{SV}^1[hPa^{-1}]$	f	m	R^2	dye	$K_{SV}^1[hPa^{-1}]$	f	m	R^2
BPhPhCarbAAnq (**1**)	0.163	0.512	2.60E-3	0.99884	DiPhMe2PhAkA (**11**)	0.2725	0.0828	1.89E-4	0.99806
DiPhAAnq (**4**)	1.15	0.781	5.64E-3	0.99941	DiPhAkAnq (**15**)	0.2455	0.715	2.83E-4	0.99788
TBrDiPhAAnq (**5**)	0.817	0.785	1.16E-2	0.9991	DiPhMe2PhAkAnq (**16**)	0.147	0.625	6.49E-4	0.99723
Oligo (**7**)	0.583	0.160	2.19E-4	0.99806	TDTBCP (**2**)	0.00528	0.511	7.58E-2	0.99994
TFlDiPhAAnq (**8**)	0.128	0.408	2.30E-3	0.99924	CDiFMP (**3**)	1.16	0.405	4.23E-3	0.99918
oTPhAAnq (**9**)	0.895	0.709	7.05E-3	0.99985	pTCP (**18**)	0.00553	0.181	5.12E-2	0.99907
DiBroTPhAAnq (**10**)	0.765	0.709	1.16E-2	0.99968	mTCP (**19**)	0.00169	0.514	5.44E-2	0.99995
DiTBCarbAnq (**17**)	0.0175	0.612	1.31E-2	0.99942	oTCP (**20**)	0.00724	0.529	5.99E-2	0.99953
DiFlBPhAAnq (**22**)	0.214	0.598	1.99E-3	0.99864					
DiPhMe2PhAAnq (**21**)	0.763	0.674	1.02E-2	0.99965					

5.3.3 Photostability

As the photostability is an important parameter for the application of sensors, it was assessed via high intensity irradiation of the sensor foils and monitoring the absorption of the sensor foils. Unlike the oxygen calibrations, the experiments were conducted only once for each dye, as a triple determination appeared to be too time consuming. All dyes except **3** show reasonable absorption at $\lambda = 465nm$, which is the wavelength of the emission peak of the used high power 3 LED-array (photon flux of 5500 µmol s^{-1} m^{-2}) and is also in close proximity to the wavelength the dyes and sensors are usually excited. Therefore the results for **3** are of limited significance, however, still show more photobleaching with this minimal absorption than for the other dyes. The other dyes display very good photostability (c.f. figures 5.30, 5.31 and 5.32).

In another preliminary experiment, an insight to the mechanism of photobleaching was gained. Apart from the standard experiment, which was done at ambient air, one sensor foil was also irradiated under "Ar atmosphere". The Ar atmosphere was provided by an Ar filled balloon attached to a syringe, which purged the inside of a cuvette sealed by a screw cap with Ar. The resulting Ar atmosphere, although much less than before, apparently still contained significant amounts of oxygen. The results of the experiment conducted under these conditions were quite surprising, as the photobleaching increased considerably. Therefore the experiment was repeated under improved conditions, with Ar purging directly from a gas bottle and to mimic the poorly deoxygenated atmosphere used before, by purging with N_2 containing 0.1% O_2. The results are depicted in figure 5.29. Apparently the photobleaching is enhanced by small amounts of oxygen. When considering if the photobleaching occurs with the dye being in the singlet or the triplet state, these results could be an indication for the triplet state. The lifetime of the triplet
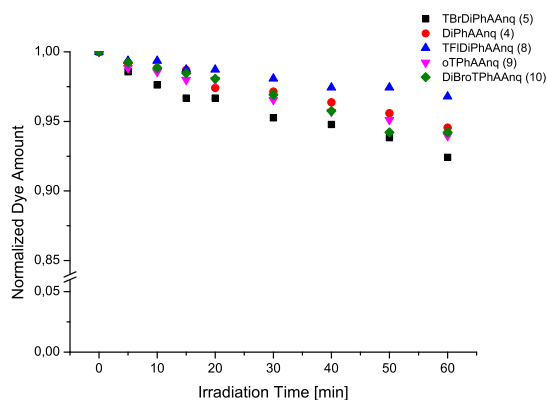
Figure 5.30: Results of the photobleaching experiments for the anthraquinone based dyes.
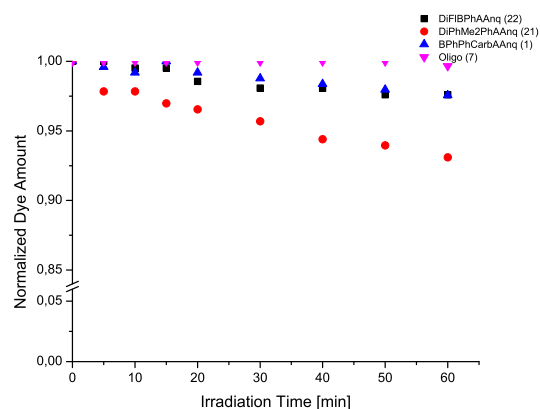
Figure 5.31: Results of the photobleaching experiments for the anthraquinone based dyes.
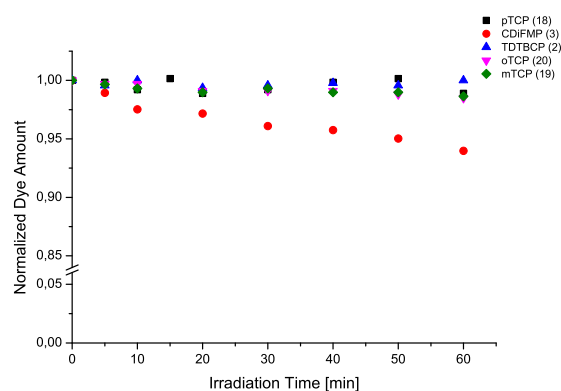
Figure 5.32: Results of the photobleaching experiments for the dicyanobenzene based dyes.
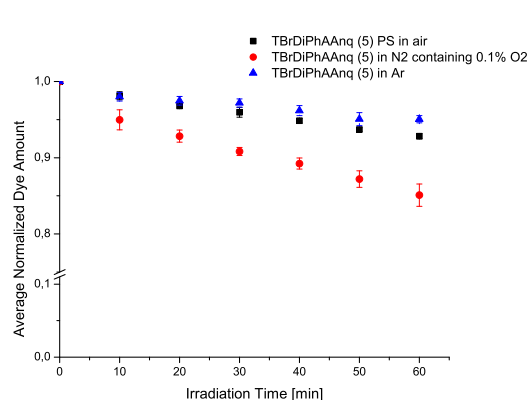
Figure 5.33: Comparison of the photobleaching of **24** under different conditions.

state strongly depends on the oxygen concentration of the environment. A decreasing oxygen concentration results in an increase of the lifetime, a measure for the time the dye stays in this state. If the lifetime becomes longer, the triplet state now becomes more vulnerable to reaction with singlet oxygen produced by luminescence quenching. When no oxygen is present the lifetime is long, but no oxygen for the reaction is available. at low oxygen concentrations the lifetime is still long, but oxygen becomes available for photobleaching. At high oxygen concentration, there is much oxygen available, but due to the decrease of the lifetime, the dye is less prone to photobleaching, since it is efficiently deactivated to the ground state. However, these results and its proposed explanation can serve as a starting point for further investigation.

5.3.4 Temperature Dependency - Temperature Calibration

PS Foils

Another parameter to check for the investigation of the suitability of these dyes for oxygen sensing was their temperature dependency. This was done by temperature dependent measurement of the TADF lifetimes of the sensor foils under deoxygenated conditions (2 wt% aqueous sodium sulfite solution). The foils were diagonally placed in cuvettes filled with the sodium sulfite solution and were kept in the refrigerated/heating circulator before measurement to preadjust the right temperature. The measurements were performed with temperature adjusted by a peltier element. During fitting, data region and parameters were chosen to keep the relative amplitudes of the two lifetime components constant. The average lifetimes calculated according to equation 3.1 were plotted against temperature to depict the temperature dependency. The received average lifetimes at 25 °C occasionally compare only poorly to those determined during basic sensor characterisation, but seem to be consistent within the temperature calibration. The poor comparability may be due to many factors, starting with inconsistent fitting (considering the biexponetial form), heterogeneity of the sensor foils (different foils were used), varying pressures in the cuvettes (heating, closed cuvette, release of overpressure), different light intensities reaching the sensor foils (TTA) and others. In figures 5.34, 5.35, 5.36 and 5.37 the temperature dependency of the lifetime of the polystyrene sensor foils is depicted. The huge temperature dependency renders the sensor foils unsuitable for oxygen sensing for standard applications as this feature is entirely undesirable. This, however, suggested the use of these dyes as temperature probes after incorporation into oxygen impermeable matrices like poly(vinylidene chloride-*co*-acrylonitrile) ("PVCAN"). The temperature dependency of prompt fluorescence was determined for two selected dyes **2** and **4** and the results are depicted in 5.38. In contrast to the TADF lifetimes, the prompt fluorescence lifetimes only display a minor decrease when temperature is changed from 278 to 323 K with 3 % for **2** and 19 % for **4**.
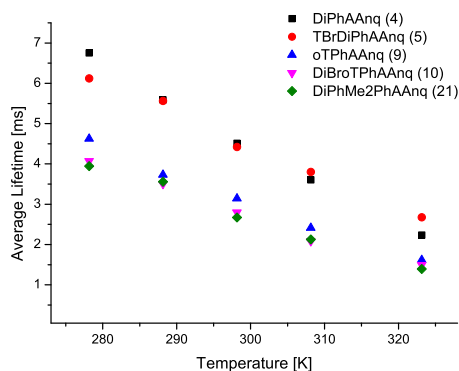
Figure 5.34: Average lifetime of the PS sensor foils of the anthraquinone based dyes plotted as a function of temperature.
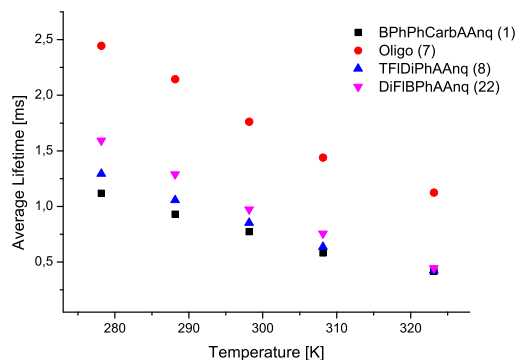
Figure 5.35: Average lifetime of the PS sensor foils of the anthraquinone based dyes plotted as a function of temperature.
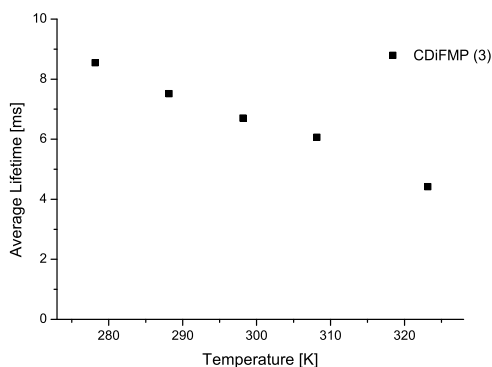
Figure 5.36: Average lifetime of the PS sensor foils of **3** plotted as a function of temperature.
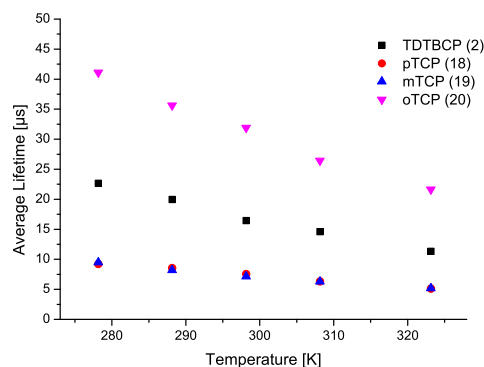
Figure 5.37: Average lifetime of the PS sensor foils of the dicyanobenzene based dyes plotted as a function of temperature.
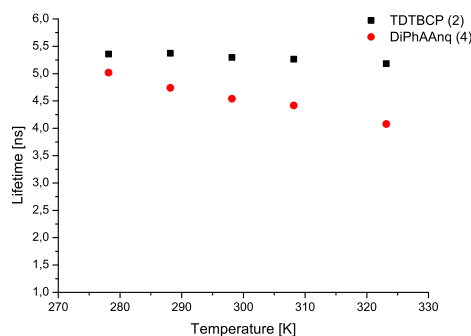
Figure 5.38: Prompt fluorescence lifetimes of **2** and **4** plotted as a function of temperature.

PVCAN Foils

After incorporation of the dyes (dyes with shorter lifetimes/reduced oxygen sensitivity were chosen) into a PVCAN matrix, the temperature dependency measurements were repeated under air saturated ("air") and deoxygenated (2 wt% aqueous sodium sulfite solution, "ax") conditions (with representative decay curves depicted in figures 5.39, 5.40, 5.41 and 5.42), to investigate the temperature dependency in the new matrix and the cross sensitivity towards oxygen. As it can be seen in figures 5.43 and 5.44, there seem to be no or only a negligible cross sensitivity (less than the experimental error) towards oxygen and a similar temperature dependency like with PS sensor foils. The sensitivity towards temperature of the individual sensor foils is listed in table 5.5 in % per Kelvin at 298 K. The values were calculated from a linear fit, as it has only a minimal deviation from the physically more meaningful Arrhenius-type model[62] and lacks the disadvantage of finding appropriate starting values for fitting. The received sensitivities are particularly high and can compare to high sensitivity probes[27].
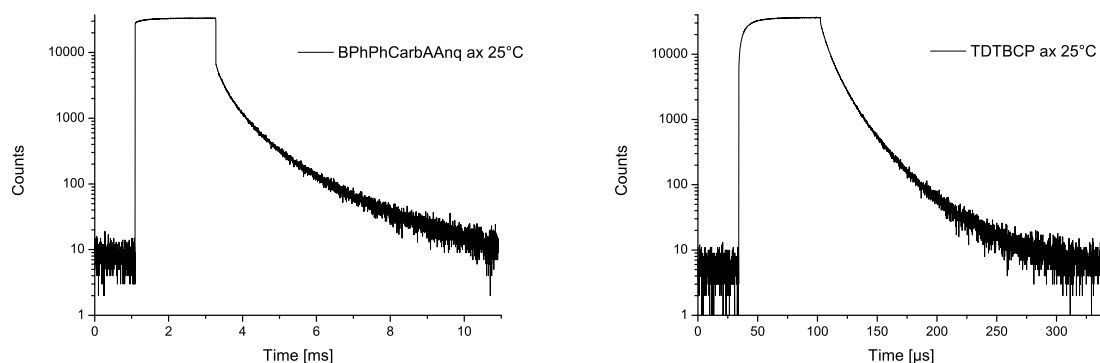
Figure 5.39: Decay curve of **1** in PVCAN at 298 K.

Figure 5.40: Decay curve of **2** in PVCAN at 298 K.
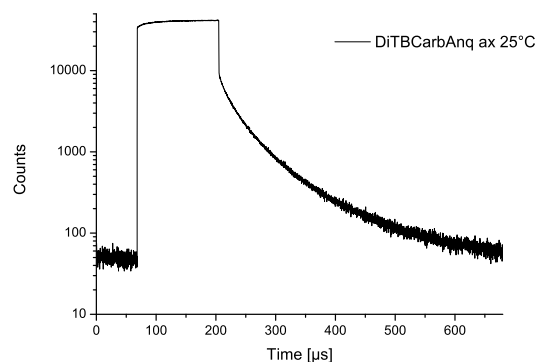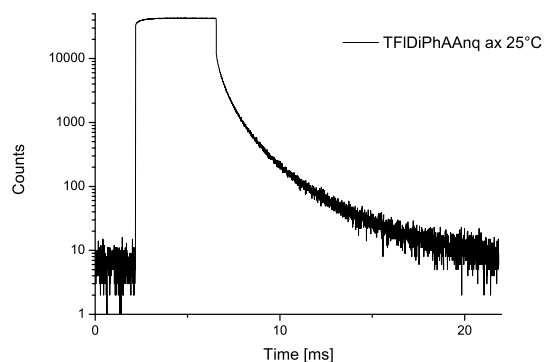
Figure 5.41: Decay curve of **8** in PVCAN at 298 K.

Figure 5.42: Decay curve of **17** in PVCAN at 298 K.
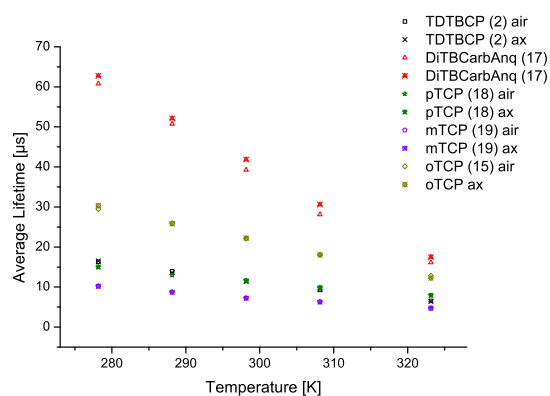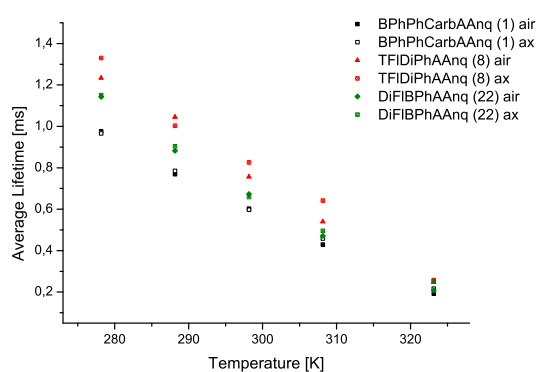
Figure 5.43: Average lifetime of the PV-CAN sensor foils of the antrahquinone based dyes plotted as a function of temperature.

Figure 5.44: Average lifetime of the PV-CAN sensor foils of the dicyanobenzene based dyes plotted as a function of temperature..

Table 5.5: Temperature sensitivity of the PVCAN sensor foils at 298 K.

	% change of τ per K		% change of τ per K
BPhPhCarbAAnq (**1**)	2.8	TDTBCP (**2**)	1.9
TFlDiPhAAnq (**8**)	2.8	pTCP (**18**)	1.5
DiFlBPhAAnq (**22**)	3.0	mTCP (**19**)	1.7
DiTBCarbAnq (**17**)	2.4	oTCP (**20**)	1.8

From the decay curves the share of TADF was estimated by division of the luminescence intensity (the number of counted photons is proportional to the intensity at a given time) at the beginning of the TADF decay (after the prompt fluorescence has ceased)

through the intensity during the pulse. The ratio stays constant for the dicyanobenzene based dyes and nearly constant for the anthraquinone base dyes, with a slight decrease of TADF at 50 °C (figures 5.45), probably due to an increase of non-radiative deexcitation pathways starting from the triplet state.

The temperature naturally also has an influence on the luminescence intensity, which also could be used for temperature measurement, but has the usual drawbacks of sole intensity based measurement. Nevertheless the change in intensity is important, as the measurement equipment needs sufficiently high signal intensities. The changes were checked for the the single photon counting based measurements and for intensity measurements at *FluoroLog® 3 spectrofluorometer*. The results show a stronger decrease for the steady-state measurements with the *FluoroLog® 3 spectrofluorometer* to around 50 % of the initial value and only a slight decrease for the single photon counting measurements. The dicyanobenzenene based dyes, however, display a lower decrease in intensity compared to the anthraquinone based dyes.
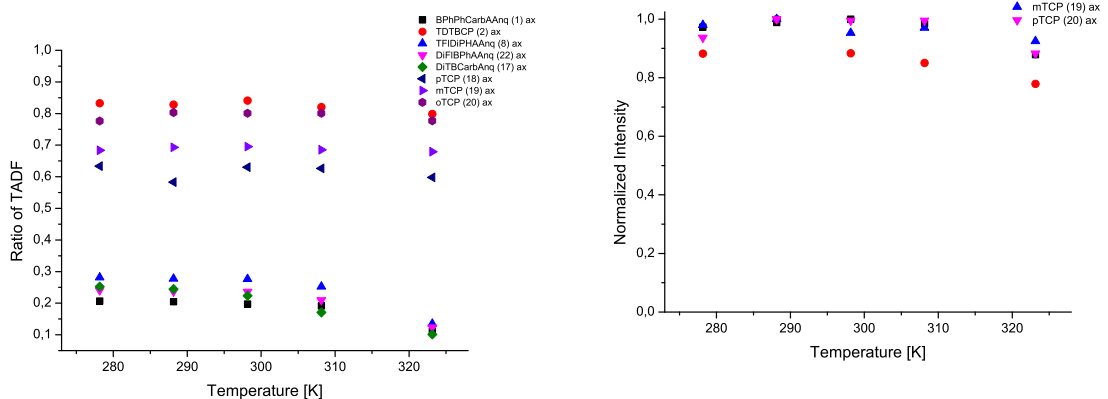
Figure 5.45: The ratio of TADF plotted as a function of temperature.

Figure 5.46: Luminescence intensity (single photon counting) of the PVCAN sensor foils of the dicyanobenzene based dyes as a function of temperature.
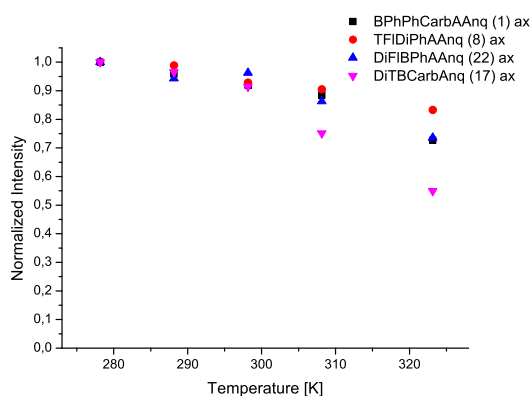
Figure 5.47: Luminescence intensity (single photon counting) of the PVCAN sensor foils of the anthraquinone based dyes as a function of temperature.
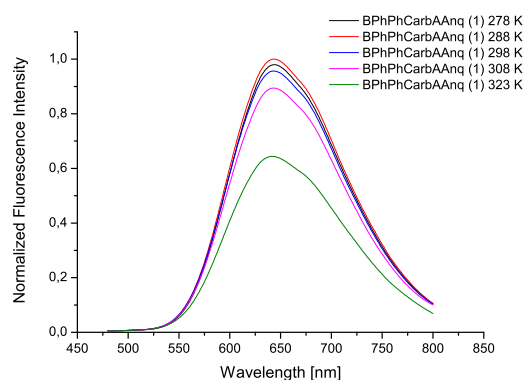
Figure 5.48: Luminescence intensity (steady state measurement) of the PV-CAN sensor foils of compound **1** as a function of temperature.
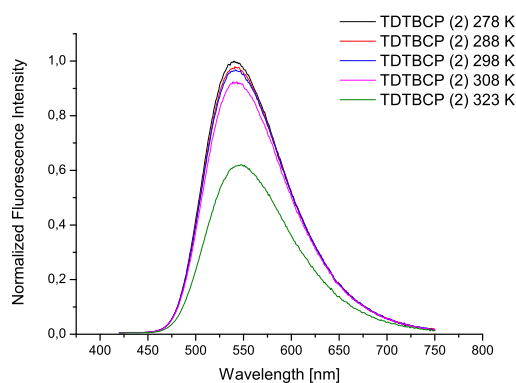
Figure 5.49: Luminescence intensity (steady state measurement) of the PV-CAN sensor foils of compound **2** as a function of temperature.
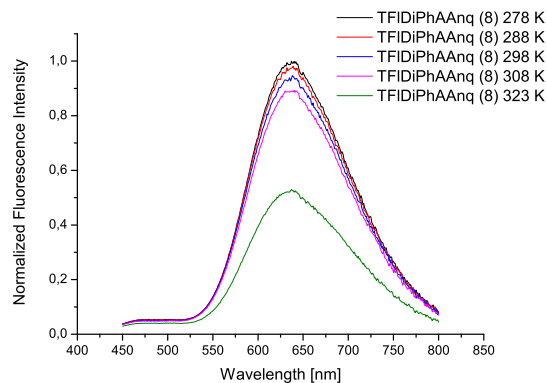
Figure 5.50: Luminescence intensity (steady state measurement) of the PV-CAN sensor foils of compound **8** as a function of temperature.
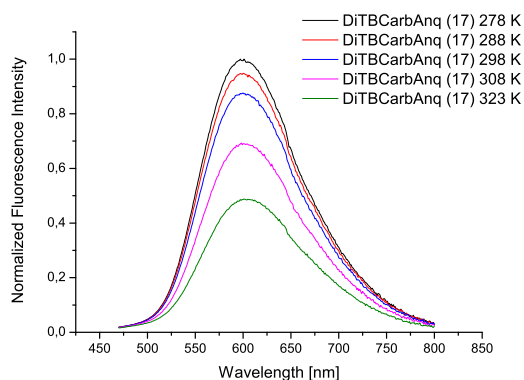
Figure 5.51: Luminescence intensity (steady state measurement) of the PV-CAN sensor foils of compound **17** as a function of temperature.

The basic properties of the prepared PVCAN sensor foils were determined as well and are shown in table 5.6.

Table 5.6: Summary of the photophysical properties of the prepared PVCAN sensor foils at 298 K.

dye	Emλ_{max} [nm]	τ_{TADF} [s]	Φ [%]	dye	Em λ_{max} [nm]	τ_{TADF} [s]	Φ [%]
BPhPhCarbAAnq (**1**)	639	5.98E-4	4	DiPhMe2PhAkAnq (**16**)	662	n.d.	8
TFlDiPhAAnq (**8**)	630	8.26E-4	5	TDTBCP (**2**)	539	1.14E-5	47
DiTBCarbAnq (**17**)	597	4.19E-5	6	pTCP (**18**)	526	1.15E-5	30
DiFlBPhAAnq (**22**)	644	6.59E-4	5	mTCP (**19**)	498	7.23E-6	72
DiPhAkAnq (**15**)	655	n.d.	16	oTCP (**20**)	522	2.22E-5	53

6 Conclusion and Outlook

In this thesis a series of bis-(diarylamino)-anthraquinones and derived structures, as well as dicyanobenzene based dyes were synthesized. The synthesis has proved not to be exceedingly demanding and was done from commercially available precursors. It was shown that the spectral properties and lifetimes of the received dyes can be adjusted over a wide range with appropriate substitution.

From the synthesized dyes, sensor foils in polystyrene were prepared with high oxygen sensitivity for the anthraquinone based dyes and high quantum yields and intermediate sensitivity for the dicyanobenzene based dyes. The sensor foils, however, are characterized by an extremely high temperature cross sensitivity and therefore are of limited relevance for oxygen sensing.

When incorporated into an oxygen impermeable matrix, such as poly(vinylidene chloride-*co*-acrylonitrile), the dyes display high temperature sensitivity with no or negligible oxygen cross sensitivity. When compared to commonly used temperature probes in literature, they rank among the most sensitive representatives reported.

It is intended to produce nano-particles with selected dyes and to investigate their applicability for temperature imaging in biological applications. The range of examined dyes could be expanded to other dye classes displaying TADF. The research also could be expanded to sensing of parameters other than oxygen and temperature, such as pH or ion sensing, by appropriate modification of already known dyes. For this goal it is essential to further reduce the TADF lifetime in order to minimize oxygen cross sensitivity.

7 References

[1] Y. Tao, K. Yuan, T. Chen, P. Xu, H. Li, R. Chen, C. Zheng, L. Zhang, W. Huang, *Advanced Materials* **2014**, *26*, 7931–7958.

[2] C. A. Parker, C. G. Hatchard, *Transactions of the Faraday Society* **1961**, *57*, 1894–1904.

[3] B. Valeur, *Molecular fluorescence: principles and applications*, OCLC: ocm45541665, Wiley-VCH, Weinheim ; New York, **2002**, 387 pp.

[4] J. C. Fister, D. Rank, J. M. Harris, *Analytical Chemistry* **1995**, *67*, 4269–4275.

[5] G. Blasse, D. R. McMillin, *Chemical Physics Letters* **1980**, *70*, 1–3.

[6] S. A. Carlson, D. M. Hercules, *Journal of the American Chemical Society* **1971**, *93*, 5611–5616.

[7] A. Maciejewski, M. Szymanski, R. P. Steer, *The Journal of Physical Chemistry* **1986**, *90*, 6314–6318.

[8] M. N. Berberan-Santos, J. M. M. Garcia, *Journal of the American Chemical Society* **1996**, *118*, 9391–9394.

[9] C. Baleizão, S. Nagl, S. M. Borisov, M. Schäferling, O. S. Wolfbeis, M. N. Berberan-Santos, *Chemistry - A European Journal* **2007**, *13*, 3643–3651.

[10] A. Endo, M. Ogasawara, A. Takahashi, D. Yokoyama, Y. Kato, C. Adachi, *Advanced Materials* **2009**, *21*, 4802–4806.

[11] X. Xiong, F. Song, J. Wang, Y. Zhang, Y. Xue, L. Sun, N. Jiang, P. Gao, L. Tian, X. Peng, *Journal of the American Chemical Society* **2014**, *136*, 9590–9597.

[12] H. Uoyama, K. Goushi, K. Shizu, H. Nomura, C. Adachi, *Nature* **2012**, *492*, 234–238.

[13] Q. Zhang, H. Kuwabara, W. J. Potscavage, S. Huang, Y. Hatae, T. Shibata, C. Adachi, *Journal of the American Chemical Society* **2014**, *136*, 18070–18081.

[14] D. Wöhrle, M. W. Tausch, W.-D. Stohrer, *Photochemie: Konzepte, Methoden, Experimente*, im Kolophon: Milton Keynes: Lightning Source, 2010, OCLC: 846444388, Wiley-VCH, Weinheim, **2010**, 523 pp.

[15] J. R. Lakowicz, *Principles of fluorescence spectroscopy*, 3rd ed, Springer, New York, **2006**, 954 pp.

[16] N. J. Turro, *Modern molecular photochemistry*, OCLC: 610827654, Univ. Science Books, Sausalito, Calif, **1991**, 628 pp.

[17] E. R. Carraway, J. N. Demas, B. A. DeGraff, *Analytical Chemistry* **1991**, *63*, 332–336.

[18] H. Adam, G. Stanislaw, I. Folke, *Pure Appl. Chem* **1991**, *63*, 1274–1250.

[19] P. Gründler, *Chemische Sensoren: eine Einführung für Naturwissenschaftler und Ingenieure ; mit 27 Tabellen*, OCLC: 820457027, Springer, Berlin, **2012**, 295 pp.

[20] *Polymer handbook, 4th edition*, 4th ed, (Eds.: J. Brandrup, E. H. Immergut, E. A. Grulke), OCLC: ocm56457312, Wiley, New York ; Chichester, **2004**, 2 pp.

[21] M. Quaranta, S. M. Borisov, I. Klimant, *Bioanalytical Reviews* **2012**, *4*, 115–157.

[22] *Optical chemical sensors*, (Eds.: F. Baldini, North Atlantic Treaty Organization), OCLC: ocm68769258, Springer, Dordrecht, **2006**, 535 pp.

[23] Y. Amao, *Microchimica Acta* **2003**, *143*, 1–12.

[24] *Temperature measurement*, 2nd ed, (Eds.: L. Michalski, L. Michalski), J. Wiley, Chichester ; New York, **2001**, 501 pp.

[25] C. Wang, R. Xu, W. Tian, X. Jiang, Z. Cui, M. Wang, H. Sun, K. Fang, N. Gu, *Cell Research* **2011**, *21*, 1517–1519.

[26] C. D. S. Brites, P. P. Lima, N. J. O. Silva, A. Millán, V. S. Amaral, F. Palacio, L. D. Carlos, *Nanoscale* **2012**, *4*, 4799.

[27] X.-d. Wang, O. S. Wolfbeis, R. J. Meier, *Chemical Society Reviews* **2013**, *42*, 7834.

[28] K. Okabe, N. Inada, C. Gota, Y. Harada, T. Funatsu, S. Uchiyama, *Nature Communications* **2012**, *3*, 705.

[29] W. Wu, J. Shen, P. Banerjee, S. Zhou, *Biomaterials* **2010**, *31*, 7555–7566.

[30] P. M. Hare, C. E. Crespo-Hernandez, B. Kohler, *Proceedings of the National Academy of Sciences* **2007**, *104*, 435–440.

[31] D. Jaque, F. Vetrone, *Nanoscale* **2012**, *4*, 4301.

[32] Y. Feng, J. Cheng, L. Zhou, X. Zhou, H. Xiang, *The Analyst* **2012**, *137*, 4885.

[33] L. H. Fischer, S. M. Borisov, M. Schaeferling, I. Klimant, O. S. Wolfbeis, *The Analyst* **2010**, *135*, 1224.

[34] P. C. Ford, E. Cariati, J. Bourassa, *Chemical Reviews* **1999**, *99*, 3625–3648.

[35] V. W.-W. Yam, K. K.-W. Lo, *Chemical Society Reviews* **1999**, *28*, 323–334.

[36] G. E. Khalil, K. Lau, G. D. Phelan, B. Carlson, M. Gouterman, J. B. Callis, L. R. Dalton, *Review of Scientific Instruments* **2004**, *75*, 192.

[37] K. Miyata, Y. Konno, T. Nakanishi, A. Kobayashi, M. Kato, K. Fushimi, Y. Hasegawa, *Angewandte Chemie International Edition* **2013**, *52*, 6413–6416.

[38] R. C. Ashoori, *Nature* **1996**, *379*, 413–419.

[39] C. McDonagh, C. S. Burke, B. D. MacCraith, *Chemical Reviews* **2008**, *108*, 400–422.

[40] O. S. Wolfbeis, *Journal of Materials Chemistry* **2005**, *15*, 2657.

[41] A. Mills, *Sensors and Actuators B: Chemical* **1998**, *51*, 60–68.

[42] A. J. Cofrancesco in *Kirk-Othmer Encyclopedia of Chemical Technology*, (Ed.: John Wiley & Sons, Inc.), John Wiley & Sons, Inc., Hoboken, NJ, USA, **2000**.

[43] A. Vogel in *Ullmann's Encyclopedia of Industrial Chemistry*, (Ed.: Wiley-VCH Verlag GmbH & Co. KGaA), Wiley-VCH Verlag GmbH & Co. KGaA, Weinheim, Germany, **2000**.

[44] E. M. Malik, C. E. Müller, *Medicinal Research Reviews* **2016**, *36*, 705–748.

[45] H.-S. Bien, J. Stawitz, K. Wunderlich in *Ullmann's Encyclopedia of Industrial Chemistry*, (Ed.: Wiley-VCH Verlag GmbH & Co. KGaA), Wiley-VCH Verlag GmbH & Co. KGaA, Weinheim, Germany, **2000**.

[46] G. Goor, J. Glenneberg, S. Jacobi in *Ullmann's Encyclopedia of Industrial Chemistry*, (Ed.: Wiley-VCH Verlag GmbH & Co. KGaA), Wiley-VCH Verlag GmbH & Co. KGaA, Weinheim, Germany, **2007**.

[47] G. Collin, H. Höke, H. Greim in *Ullmann's Encyclopedia of Industrial Chemistry*, (Ed.: Wiley-VCH Verlag GmbH & Co. KGaA), Wiley-VCH Verlag GmbH & Co. KGaA, Weinheim, Germany, **2003**.

[48] G. Collin, H. Höke, J. Talbiersky in *Ullmann's Encyclopedia of Industrial Chemistry*, (Ed.: Wiley-VCH Verlag GmbH & Co. KGaA), Wiley-VCH Verlag GmbH & Co. KGaA, Weinheim, Germany, **2006**.

[49] K. Khan, R. Karodi, A. Siddiqui, S. Thube, R. A. Rub, *International Journal of Applied Research in Natural Products* **2012**, *4*, 28–36.

[50] M. Wuthi-udomlert, P. Kupittayanant, W. Gritsanapan, *J Health Res* **2010**, *24*, 117–122.

[51] M. Y. Fosso, K. Y. Chan, R. Gregory, C.-W. T. Chang, *ACS Combinatorial Science* **2012**, *14*, 231–235.

[52] D. Barnard, D. Fairbairn, K. O'Neill, T. Gage, R. Sidwell, *Antiviral Research* **1995**, *28*, 317–329.

[53] A. d. Meijere, F. Diederich, *Metal-catalyzed cross-coupling reactions*, 2nd, completely rev. and enl. ed, Wiley-VCH, Weinheim, **2004**, 2 pp.

[54] *Cross-coupling reactions: a practical guide*, (Ed.: N. Miyaura), OCLC: 248290932, Springer, Berlin, **2002**, 248 pp.

[55] R. Bates, *Organic synthesis using transition metals*, 2nd ed, Wiley, Chichester, West Sussex, **2012**, 446 pp.

[56] N. Miyaura, A. Suzuki, *Chemical Reviews* **1995**, *95*, 2457–2483.

[57] E. P. Gillis, M. D. Burke, *Aldrichimica acta* **2009**, *42*, 17.

[58] A. J. J. Lennox, G. C. Lloyd-Jones, *Angewandte Chemie International Edition* **2012**, *51*, 9385–9388.

[59] X. Lou, R. W. Sinkeldam, W. van Houts, Y. Nicolas, P. G. A. Janssen, J. L. J. van Dongen, J. A. J. M. Vekemans, E. W. Meijer, *Journal of Mass Spectrometry* **2007**, *42*, 293–303.

[60] E. Lee, J.-S. Lee, T.-h. Kim, K.-s. Kim, *Anthracene derivatives and organic electroluminescent device using same*, US Patent 8,395,144, Google Patents, **2013**.

[61] *Organikum: organisch-chemisches Grundpraktikum*, 21., neu bearb. und erw. Aufl, (Ed.: H. G. O. Becker), OCLC: 52657057, Wiley-VCH, Weinheim, **2001**, 852 pp.

[62] G. Liebsch, I. Klimant, O. S. Wolfbeis, *Advanced Materials* **1999**, *11*, 1296–1299.

8 List of Figures

9 List of Tables

10 Appendix

10.1 NMR Data

10.1.1 Compound 1
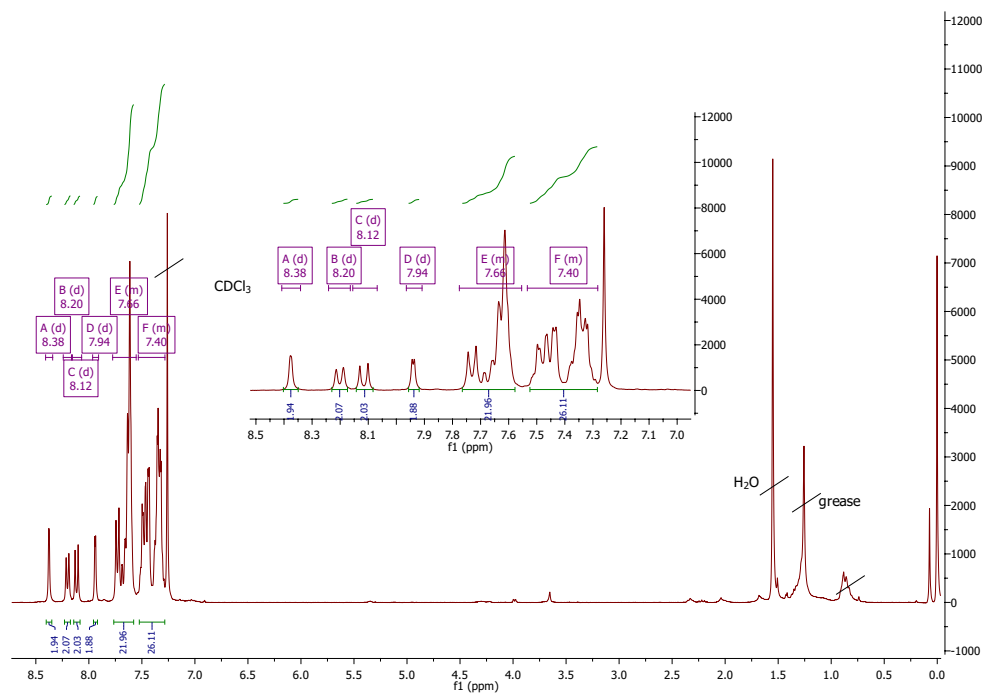
Figure 10.1: ^{1}H-NMR spectrum of compound **1**.
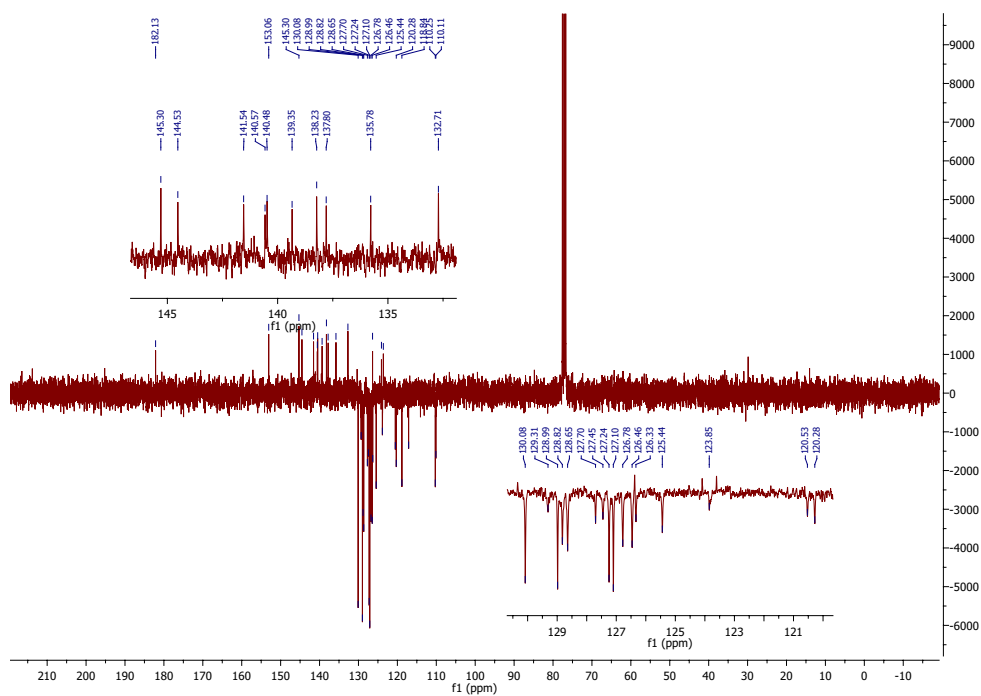
Figure 10.2: APT-NMR spectrum of compound **1**.
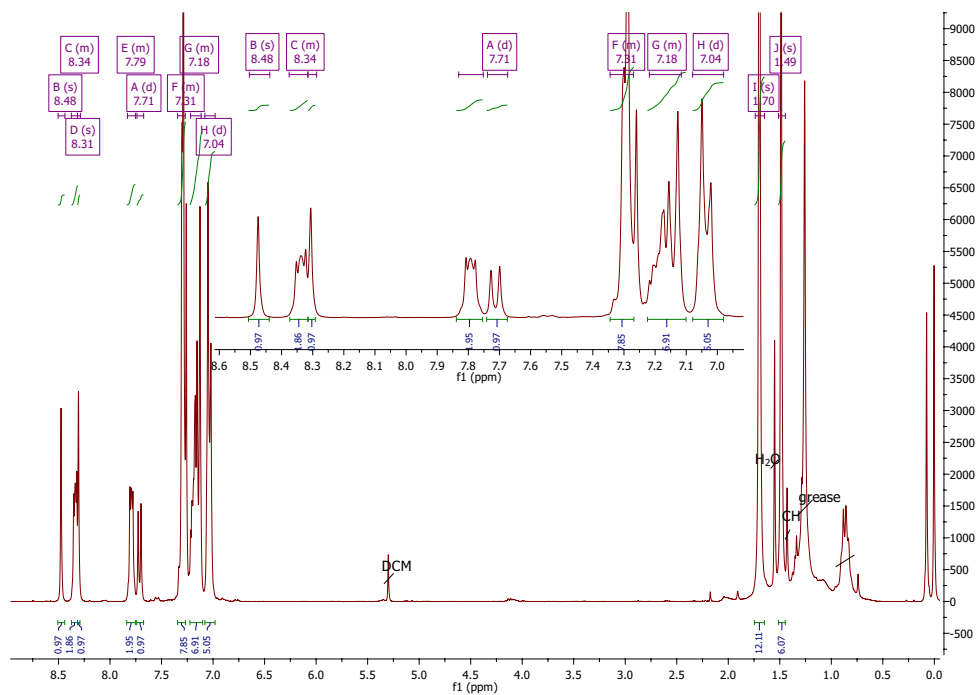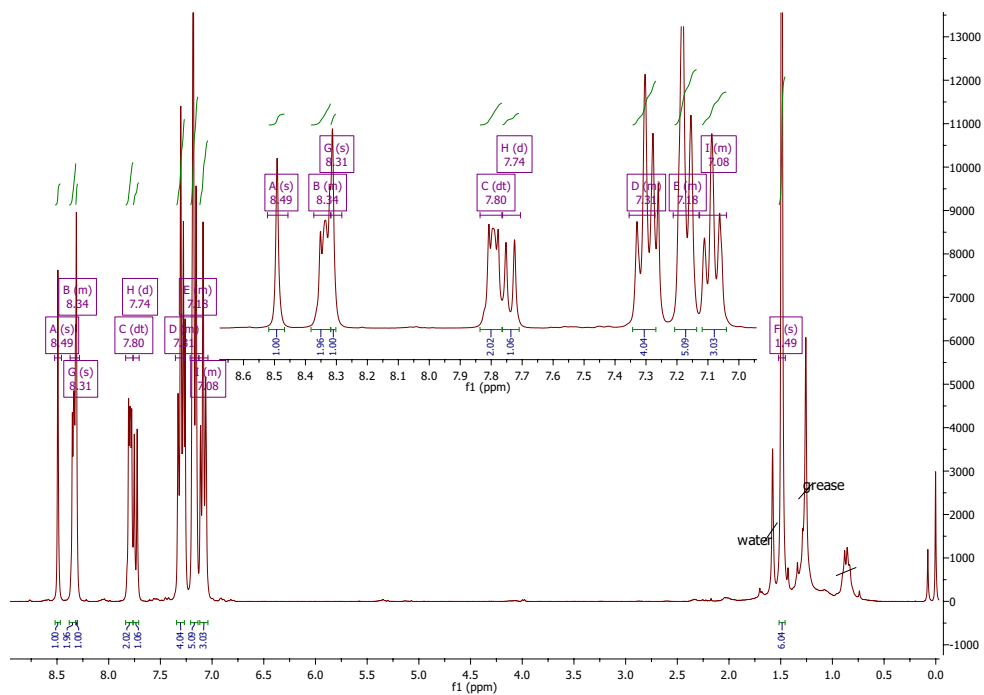
10.1.2 Compound 2
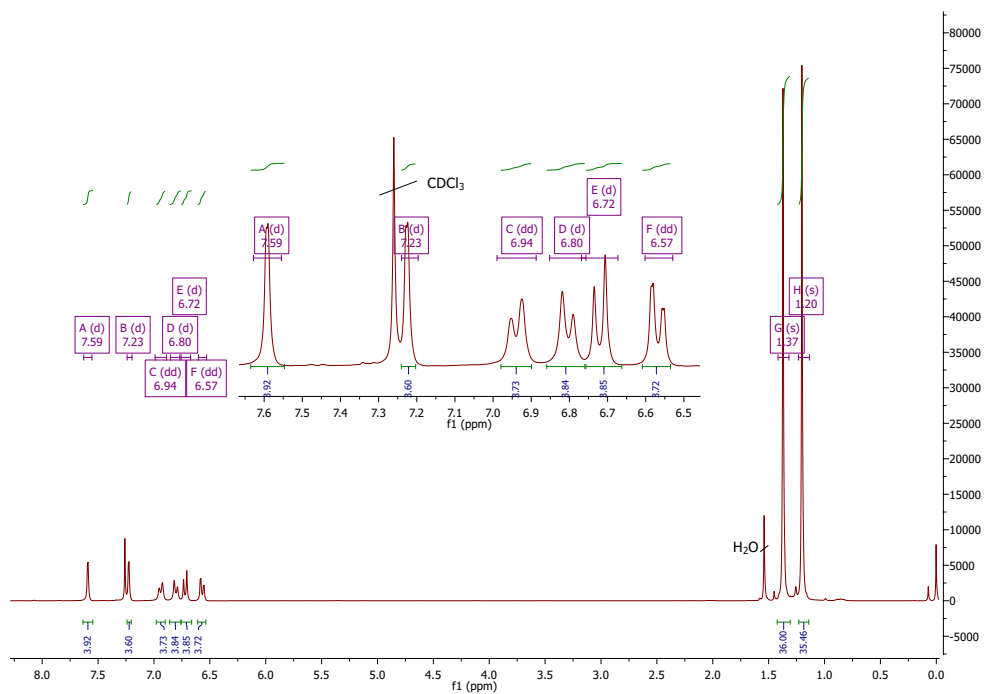
Figure 10.3: ^{1}H-NMR spectrum of compound **2**.
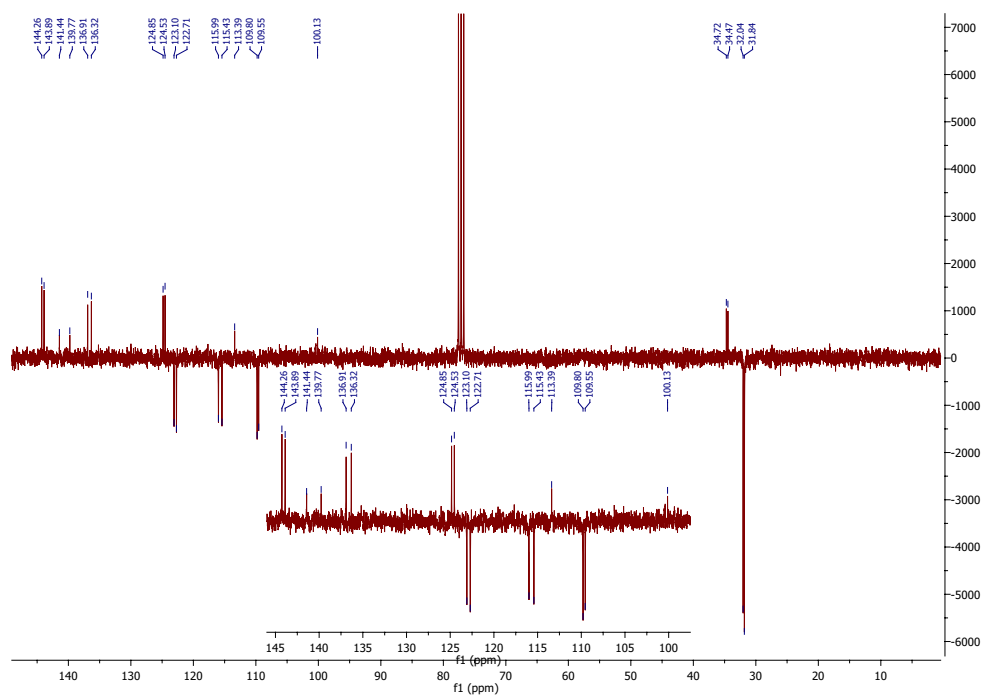
Figure 10.4: APT-NMR spectrum of compound **2**.

10.1.3 Compound 3
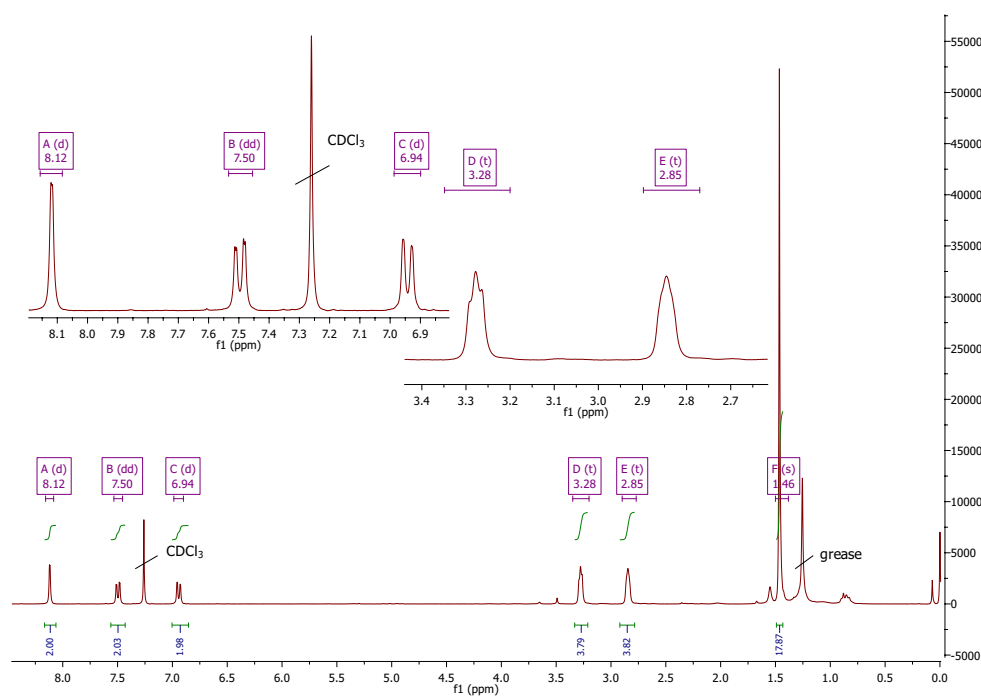
Figure 10.5: ¹H-NMR spectrum of compound **3**.
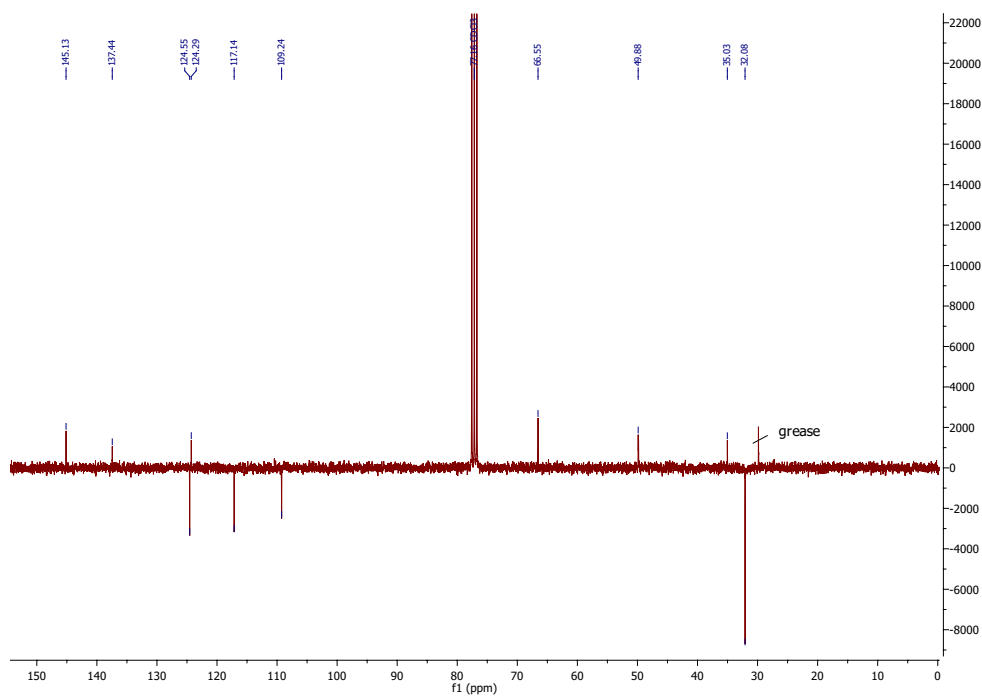
Figure 10.6: APT-NMR spectrum of compound **3**.

10.1.4 Compound 4
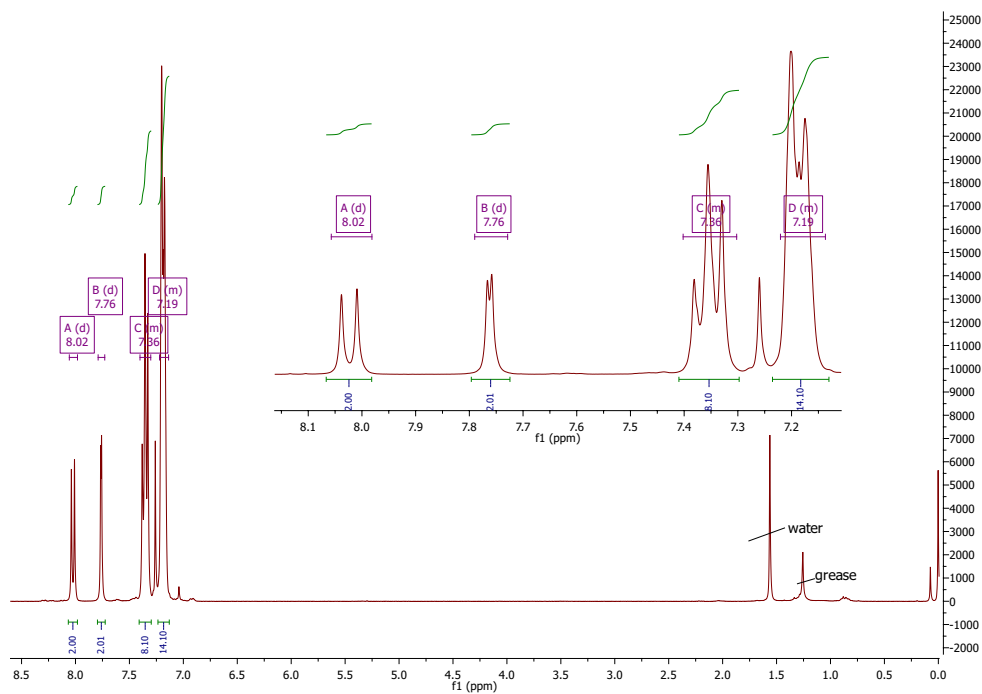
Figure 10.7: ^{1}H-NMR spectrum of compound **4**.
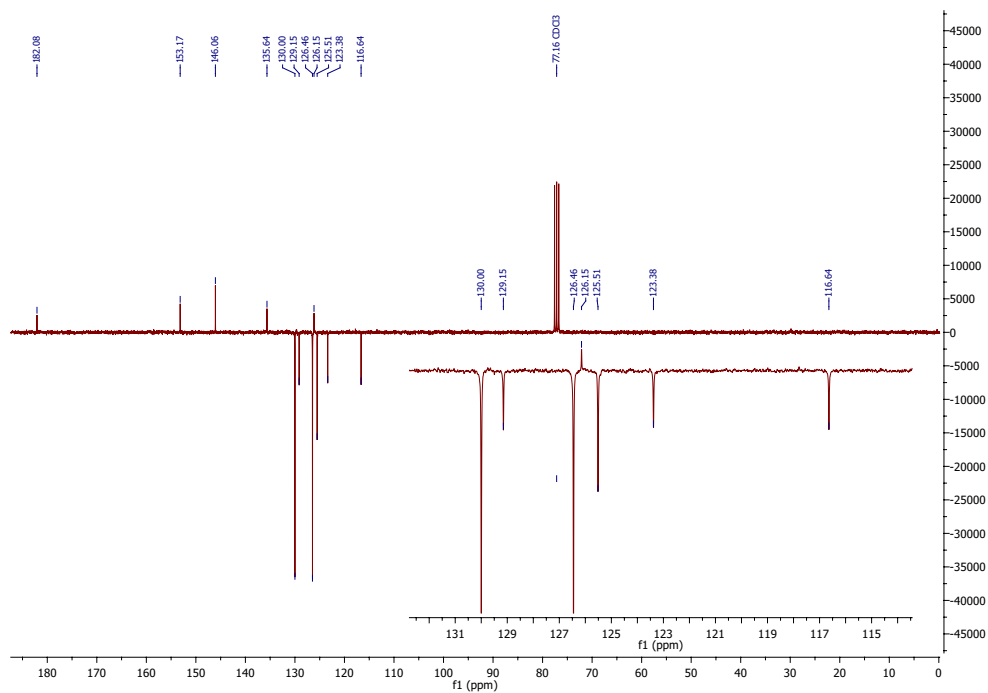
Figure 10.8: APT-NMR spectrum of compound **4**.

10.1.5 Compound 5
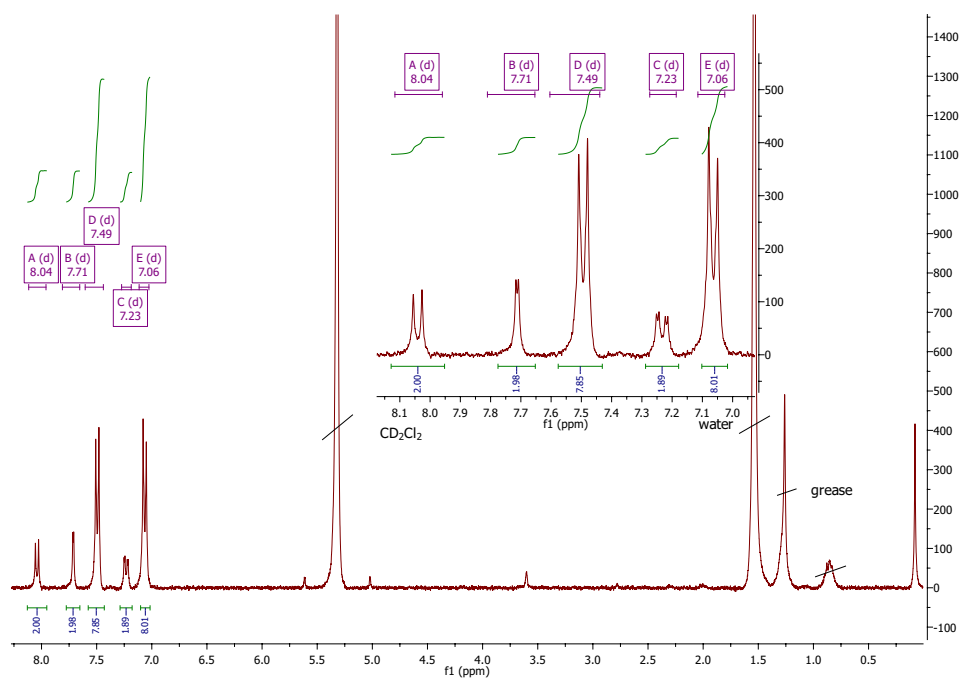
Figure 10.9: ^{1}H-NMR spectrum of compound **5**.
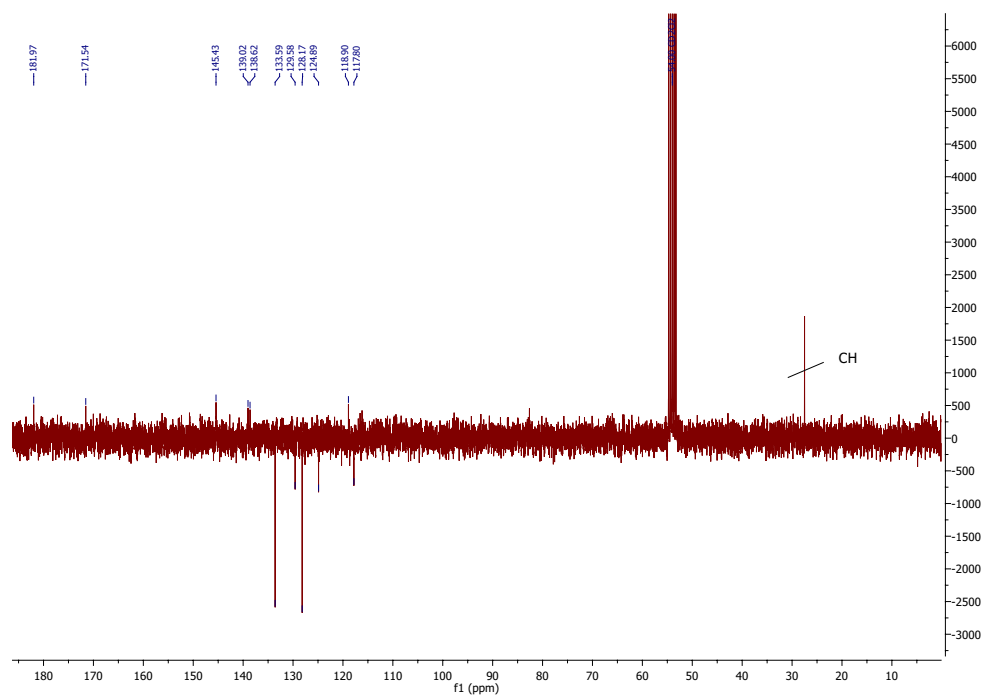
Figure 10.10: APT-NMR spectrum of compound **5**, (not the same NMR-sample as for proton-NMR).

10.1.6 Compound 6
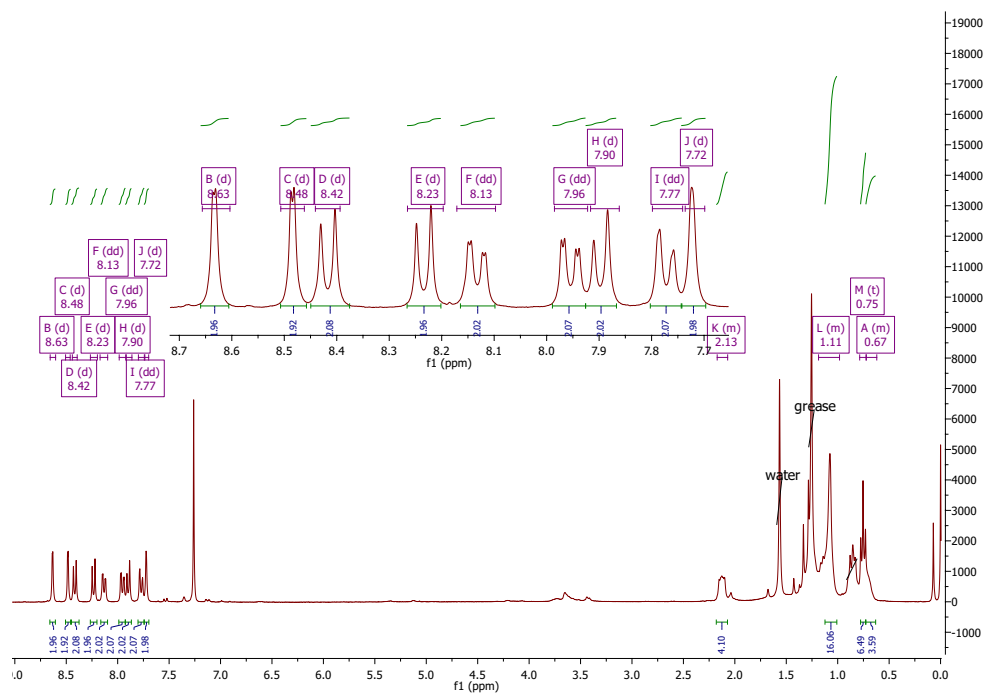
Figure 10.11: ^{1}H-NMR spectrum of compound **6**.

10.1.7 Compound 7
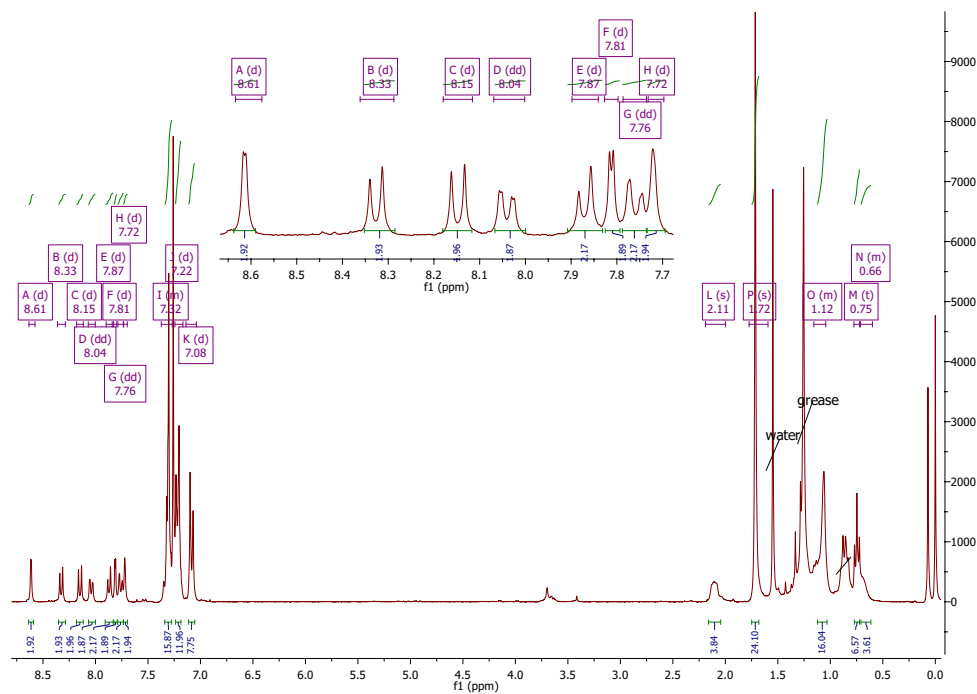
Figure 10.12: ^{1}H-NMR spectrum of compound **7**.

10.1.8 Compound 8
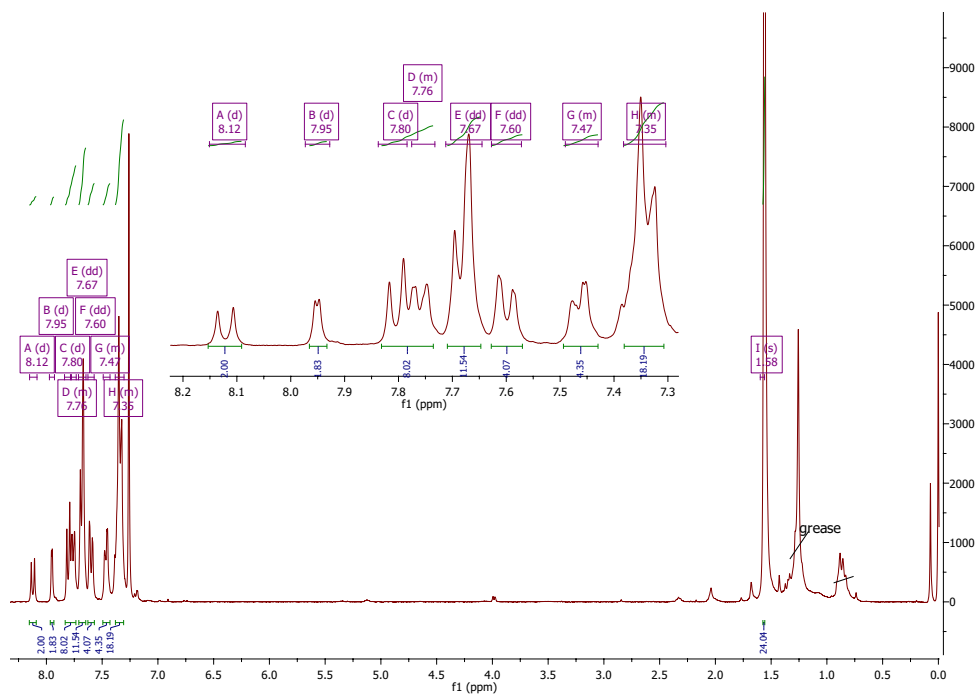
Figure 10.13: ^{1}H-NMR spectrum of compound **8**.
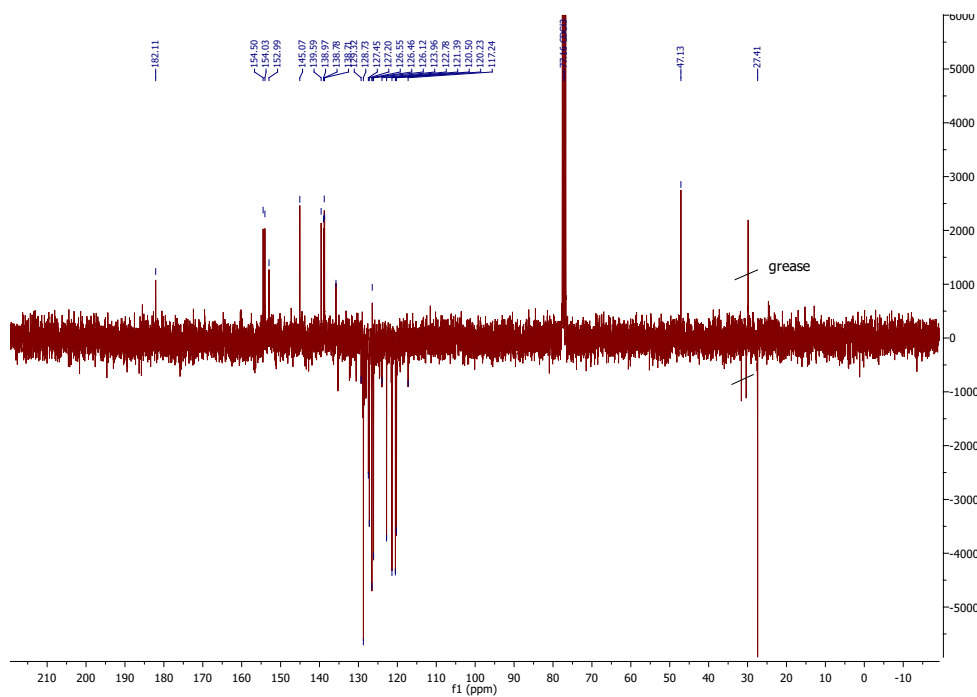
Figure 10.14: APT-NMR spectrum of compound **8**.

10.1.9 Compound 9
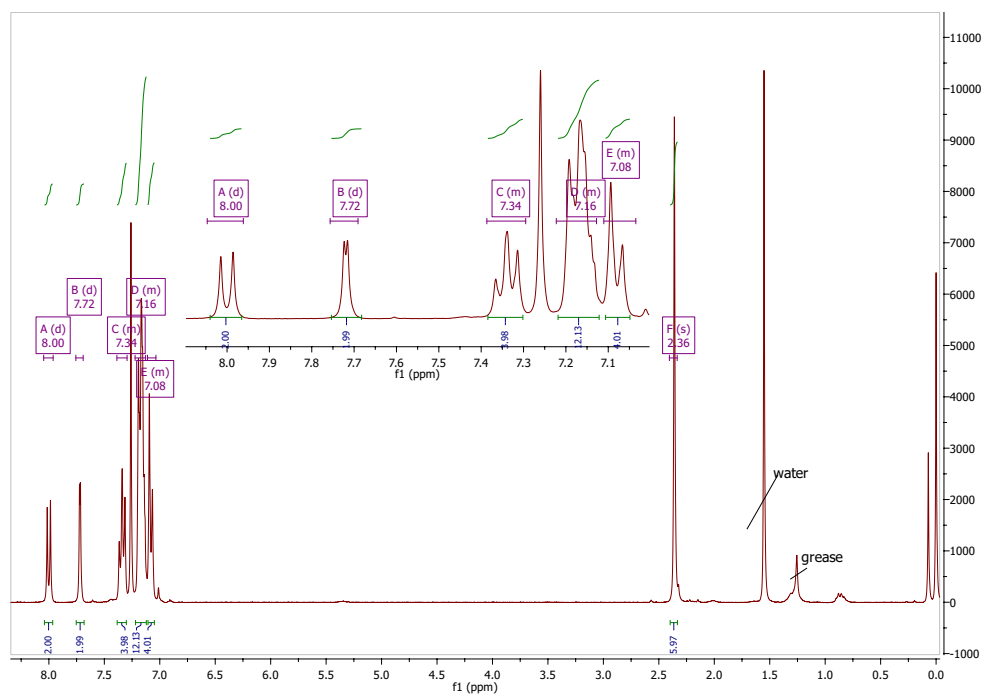
Figure 10.15: ¹H-NMR spectrum of compound **9**.
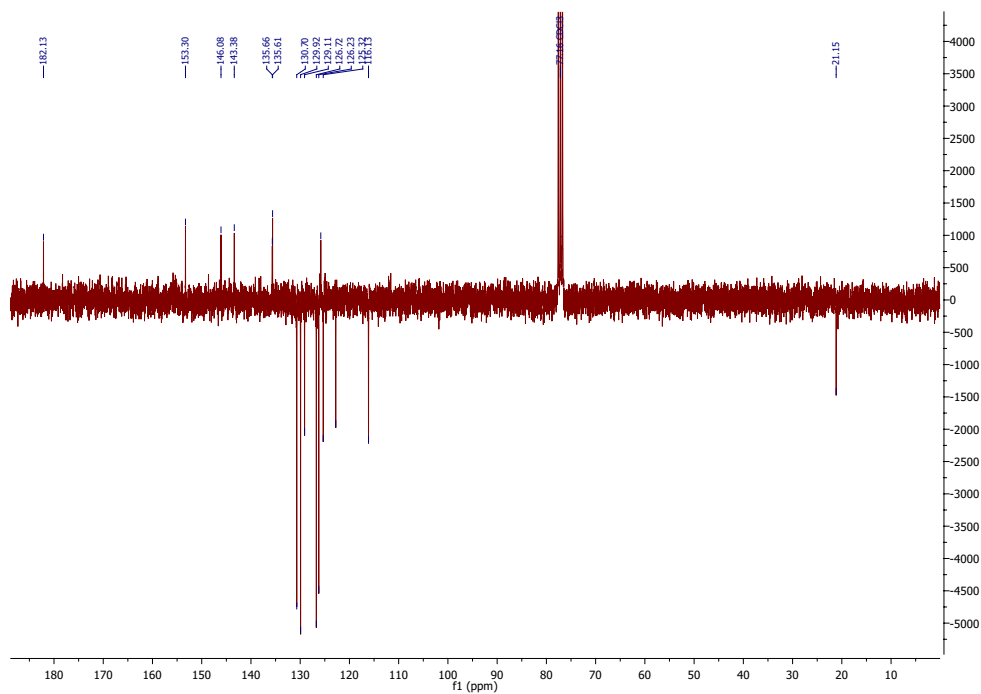
Figure 10.16: APT-NMR spectrum of compound **9**.

10.1.10 Compound 10
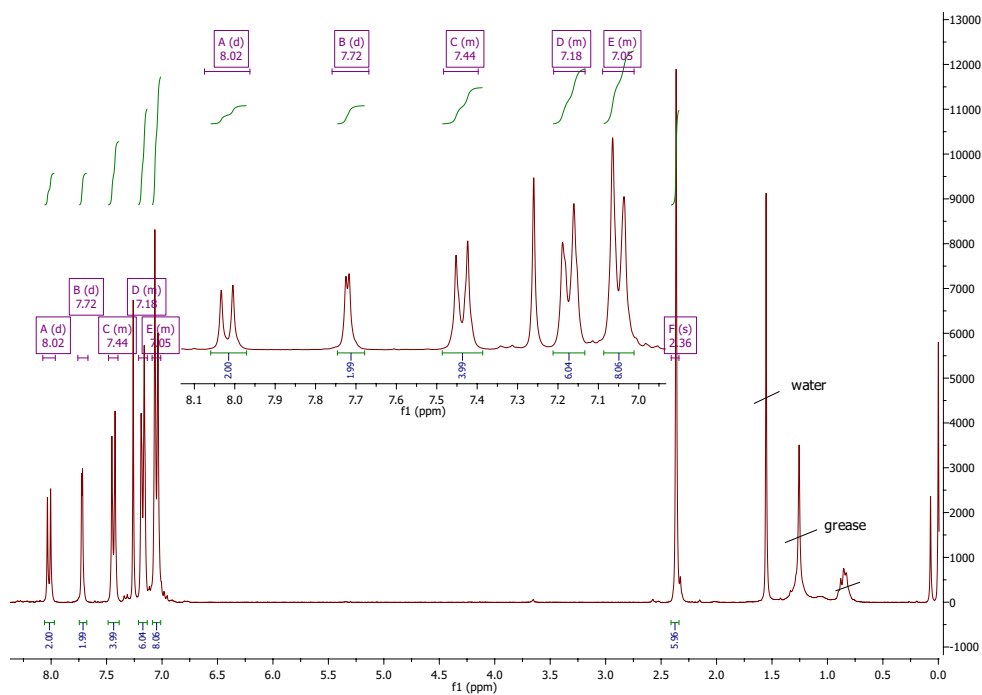
Figure 10.17: ^{1}H-NMR spectrum of compound **10**.
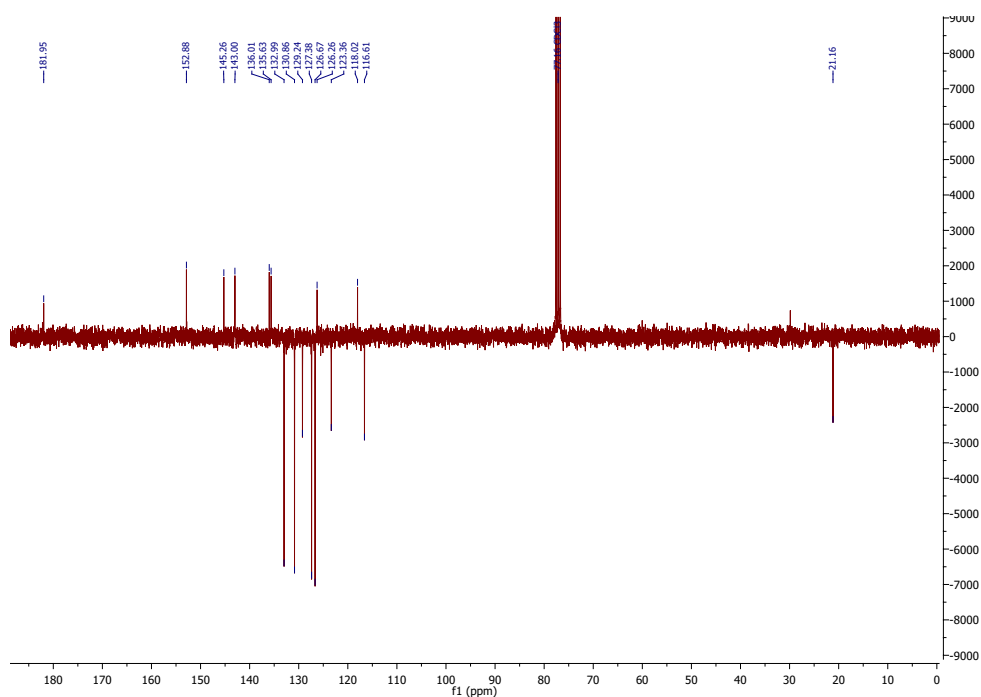
Figure 10.18: APT-NMR spectrum of compound **10**.

10.1.11 Compound 11

Figure 10.19: ^{1}H-NMR spectrum of compound **11**.
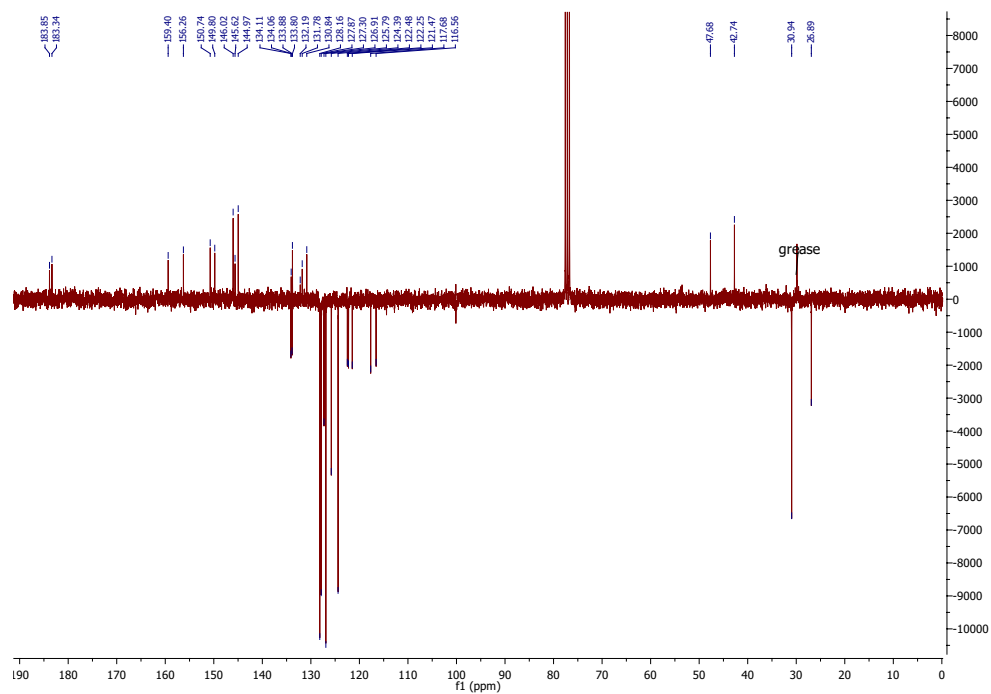
Figure 10.20: APT-NMR spectrum of compound **11**.

10.1.12 Compound 12

Figure 10.21: ^{1}H-NMR spectrum of compound **12**.
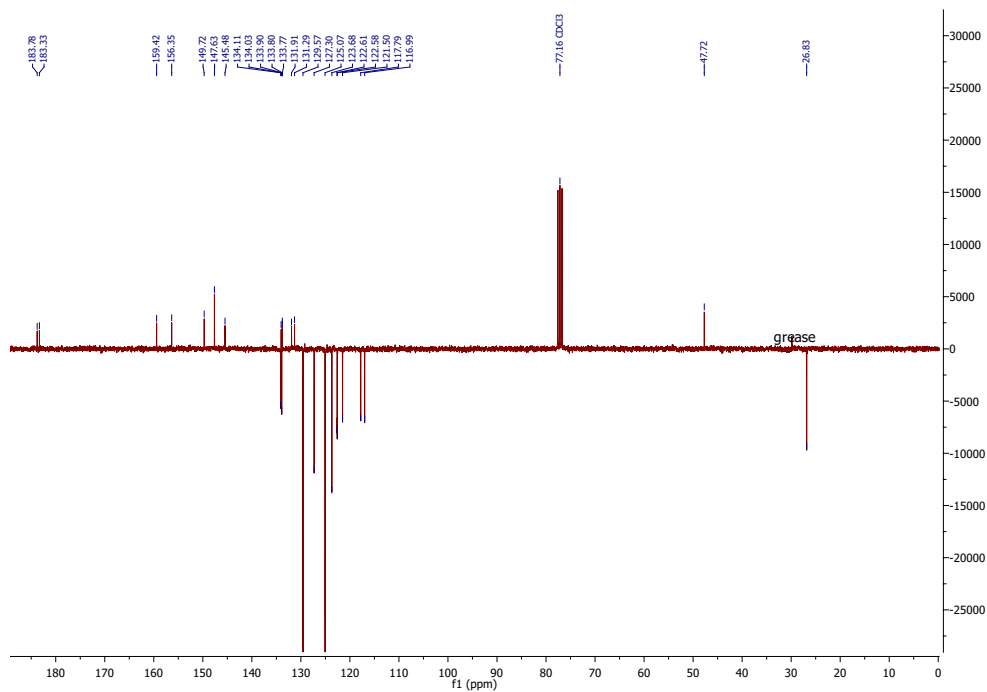
Figure 10.22: APT-NMR spectrum of compound **12**.

10.1.13 Compound 13
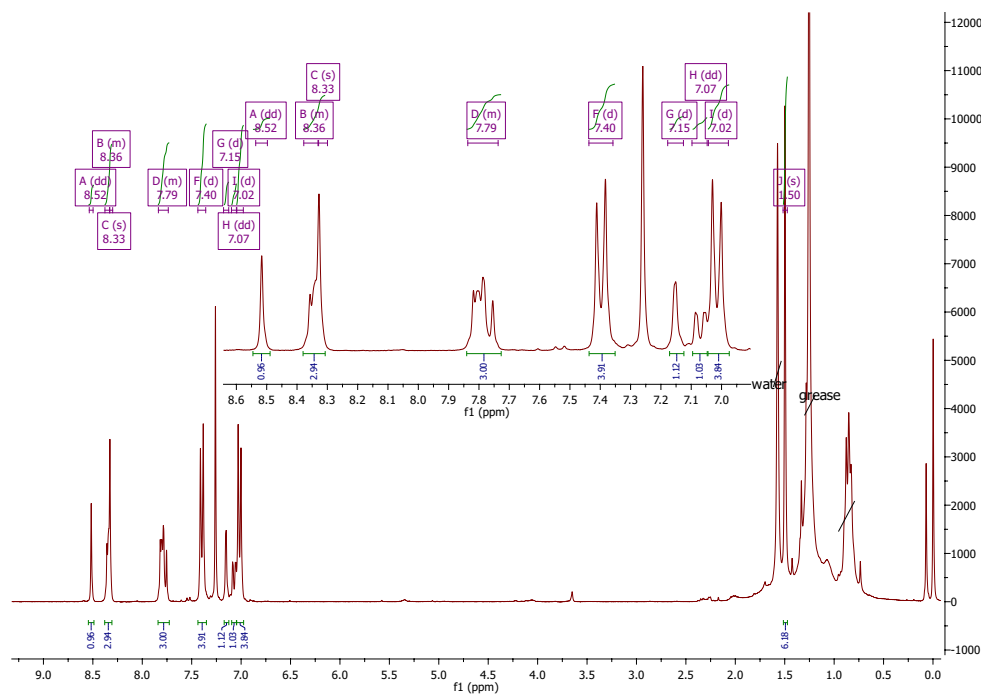
Figure 10.23: ^{1}H-NMR spectrum of compound **13**.
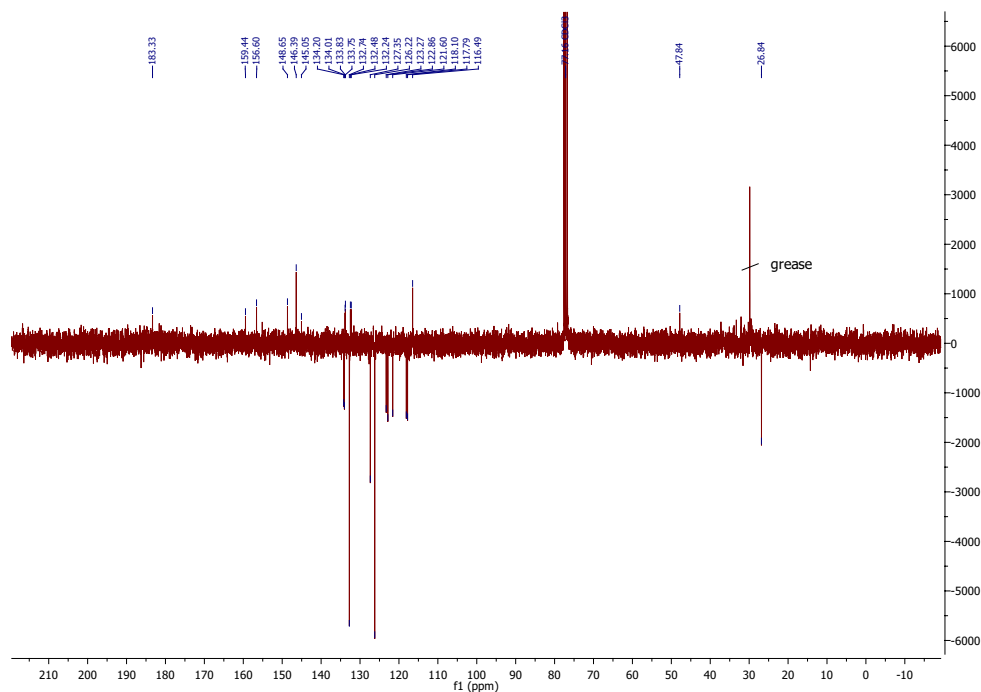
Figure 10.24: APT-NMR spectrum of compound **13**.

10.1.14 Compound 14
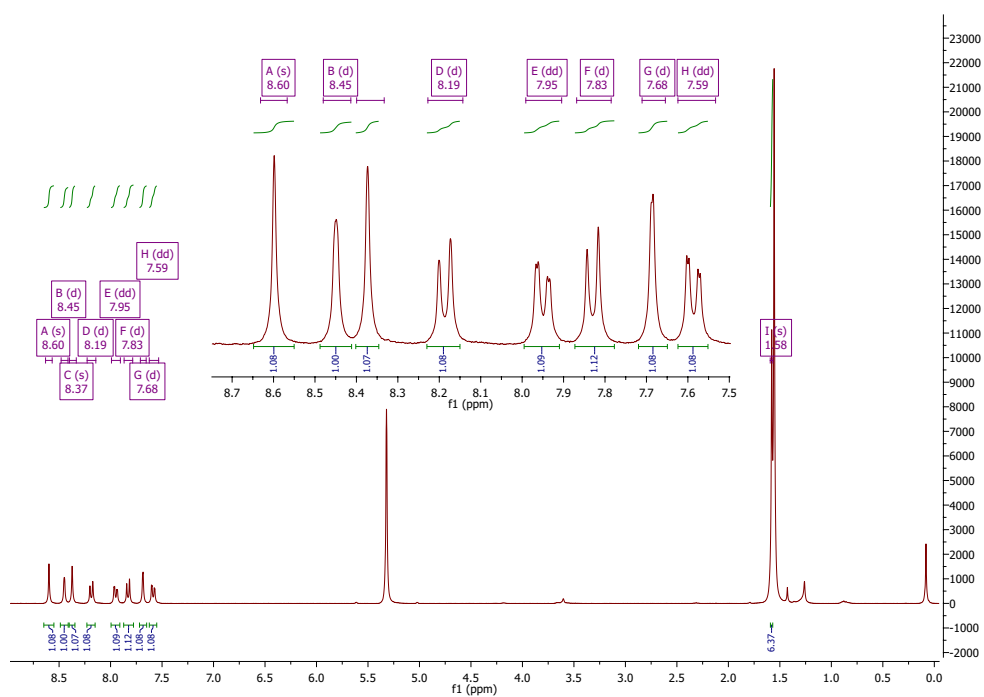
Figure 10.25: ^{1}H-NMR spectrum of compound **25**.

10.1.15 Compound 15
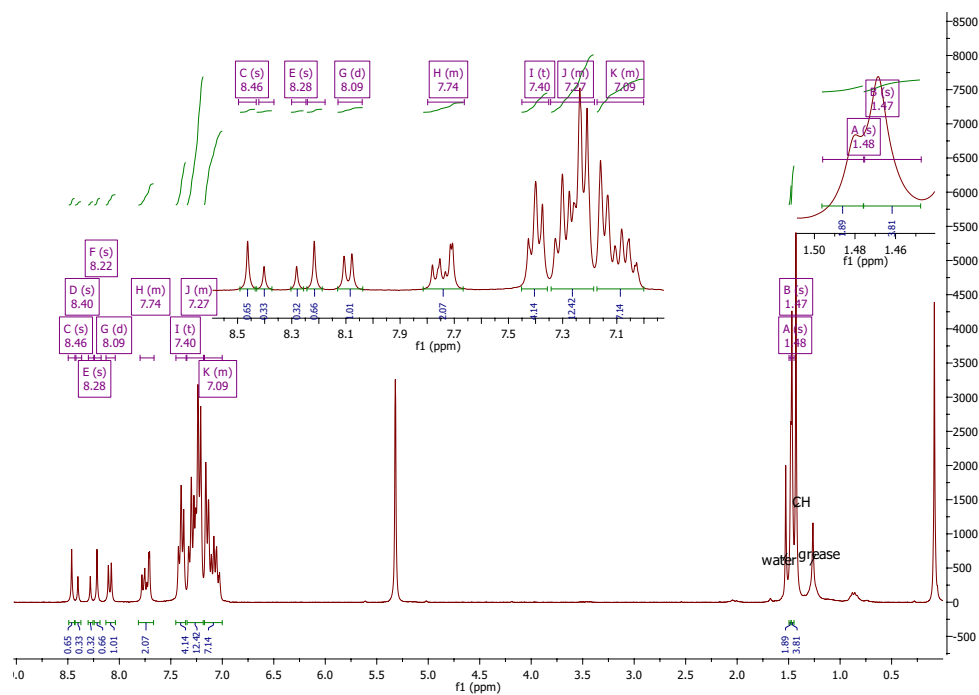
Figure 10.26: ¹H-NMR spectrum of compound **15**.
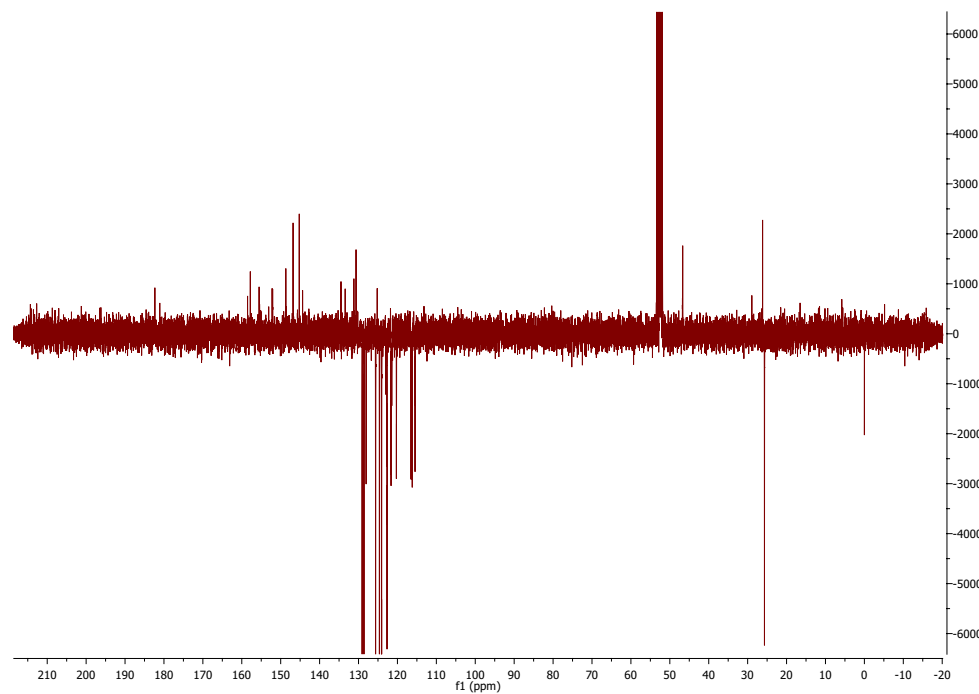
Figure 10.27: APT-NMR spectrum of compound **15**.

10.1.16 Compound 16
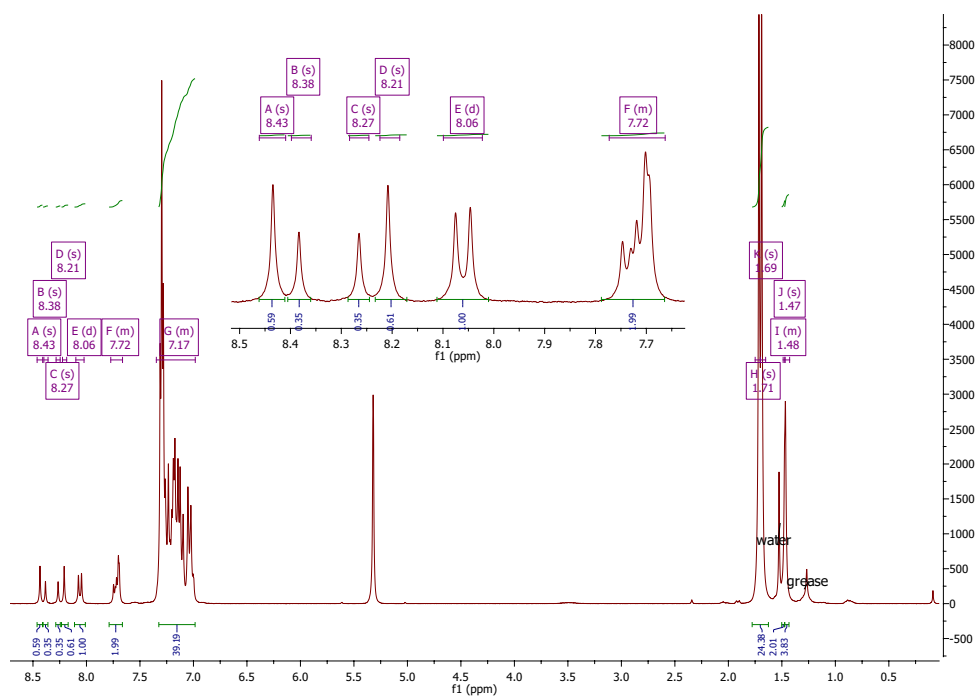
Figure 10.28: ^{1}H-NMR spectrum of compound **16**.
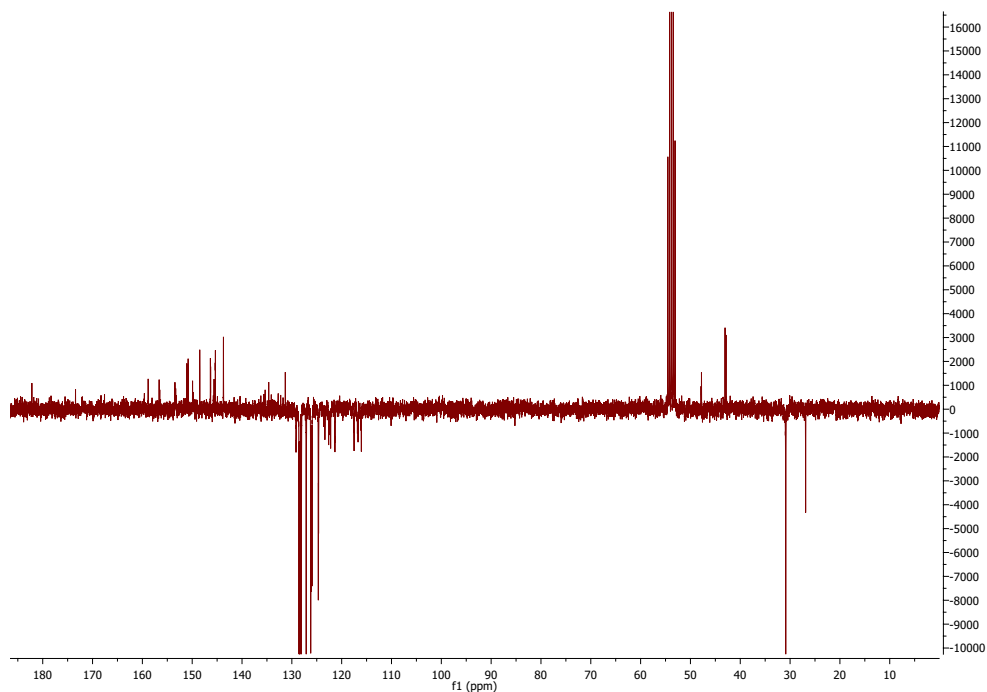
Figure 10.29: APT-NMR spectrum of compound **16**.

10.1.17 Compound 17
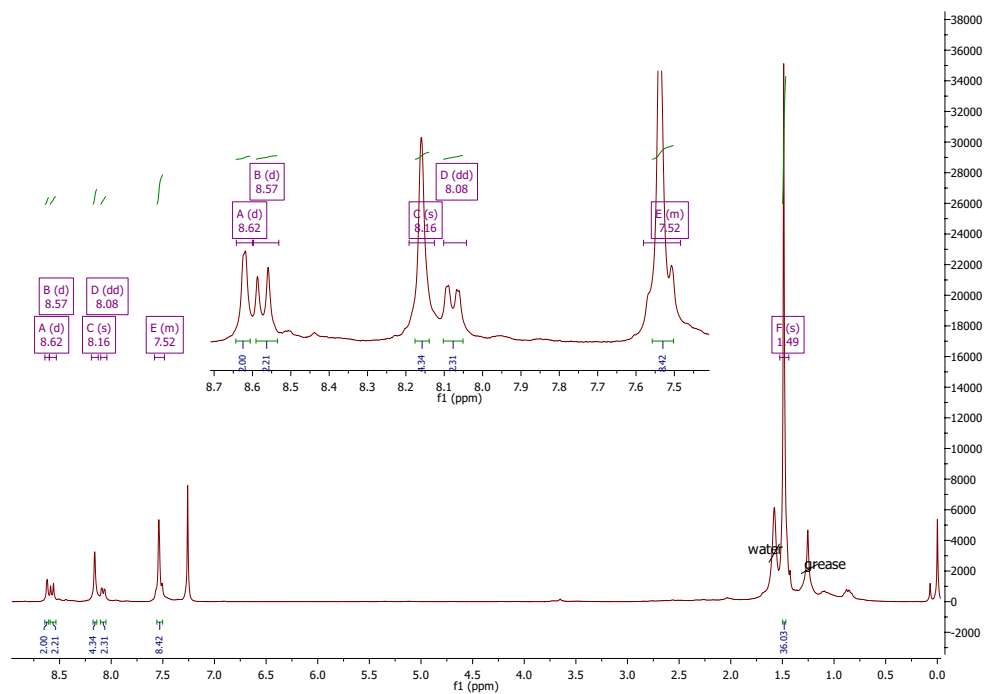
Figure 10.30: ¹H-NMR spectrum of compound **17**.

10.2 MS Data

10.2.1 Compound 1
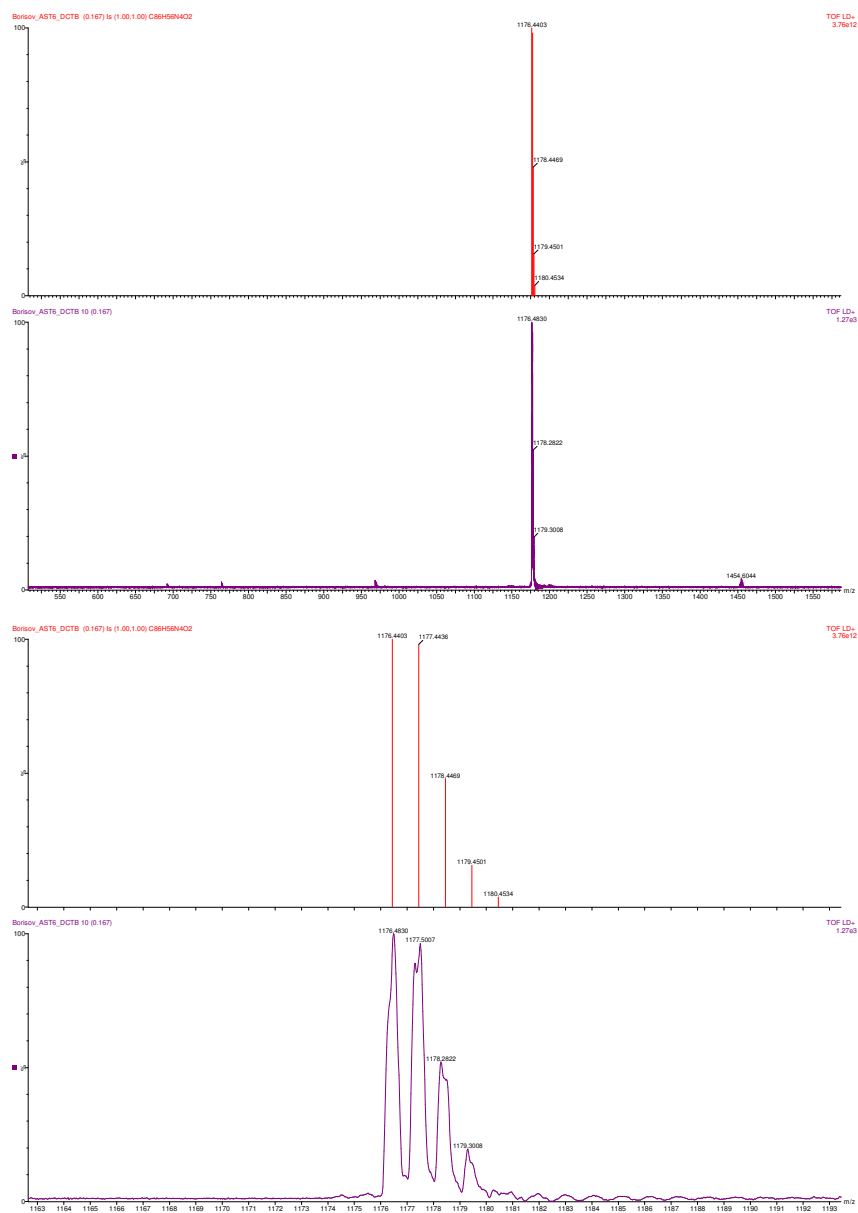
Figure 10.31: MALDI-TOF spectrum of compound **1** in a DCTB matrix and the corresponding isotope pattern.
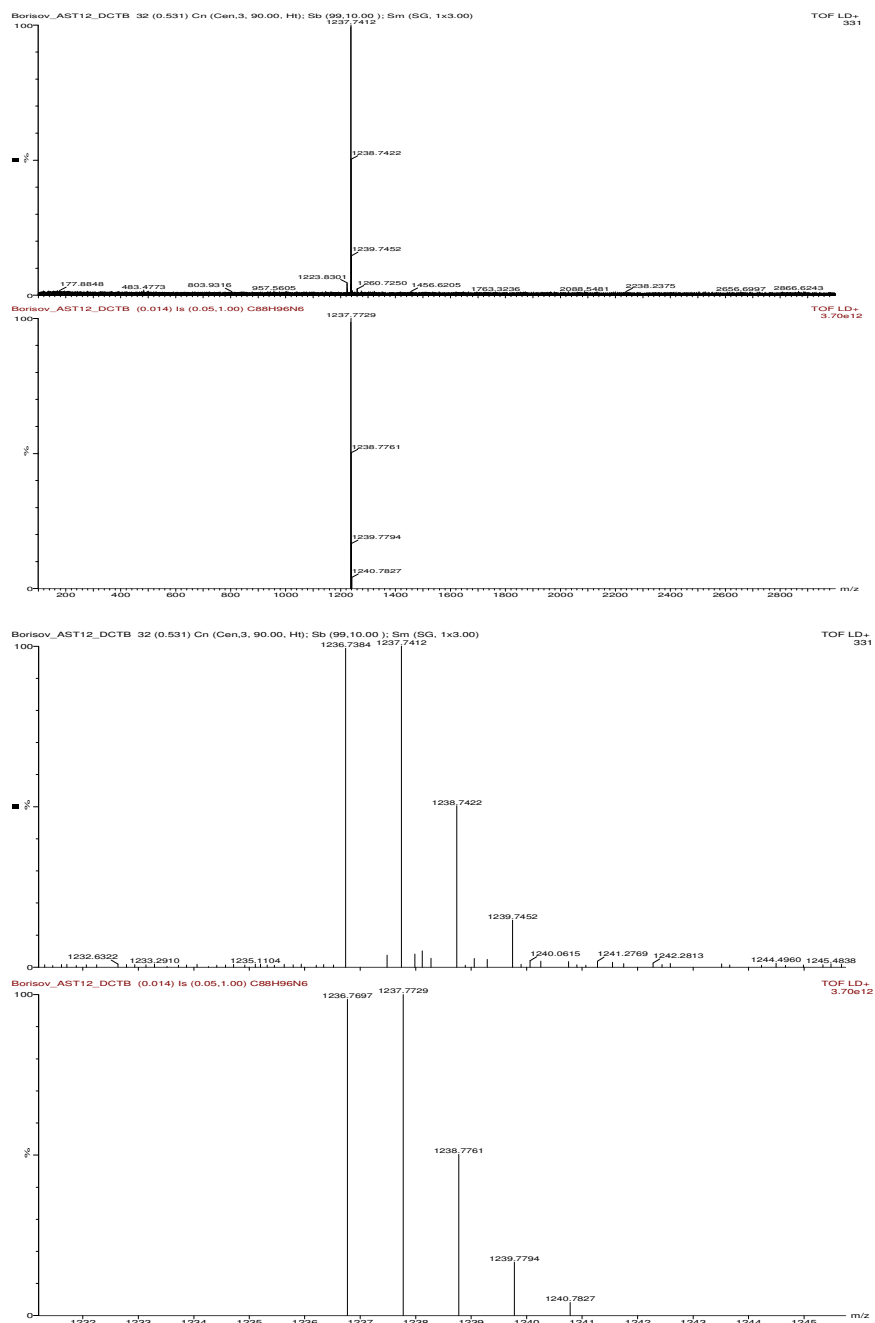
10.2.2 Compound 2

Figure 10.32: MALDI-TOF spectrum of compound **2** in a DCTB matrix and the corresponding isotope pattern.
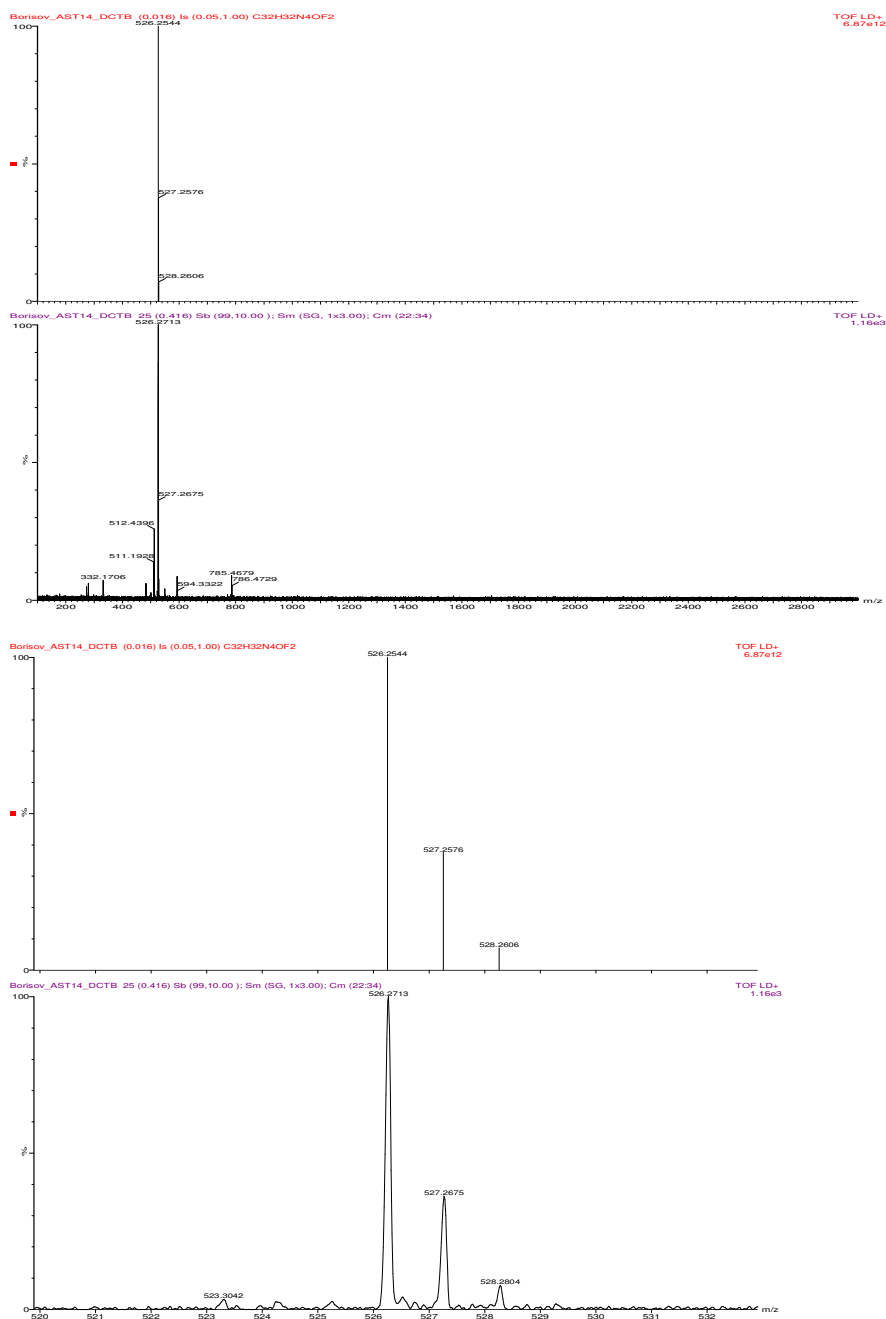
10.2.3 Compound 3

Figure 10.33: MALDI-TOF spectrum of compound **3** in a DCTB matrix and the corresponding isotope pattern.
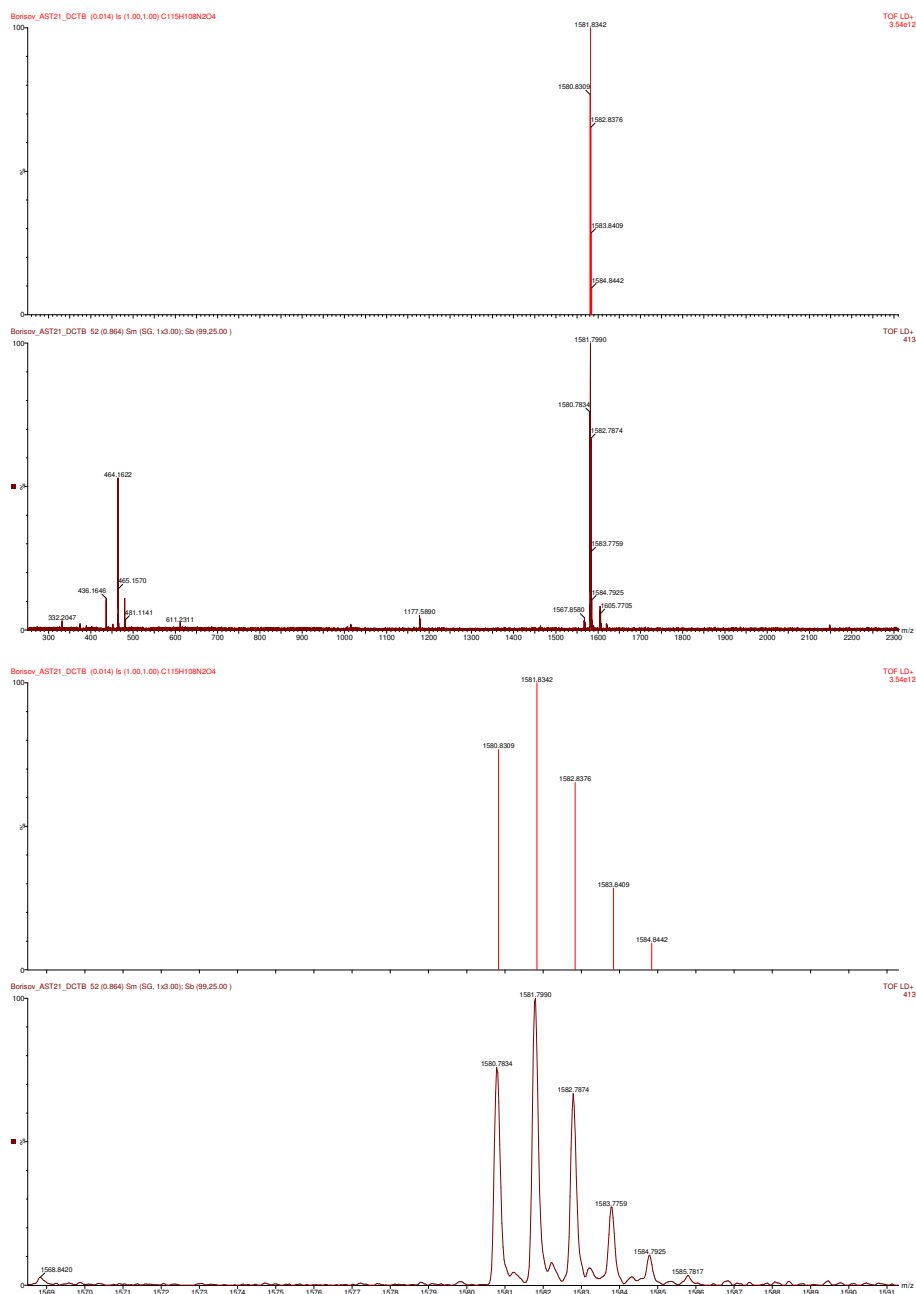
10.2.4 Compound 7

Figure 10.34: MALDI-TOF spectrum of compound **7** in a DCTB matrix and the corresponding isotope pattern.
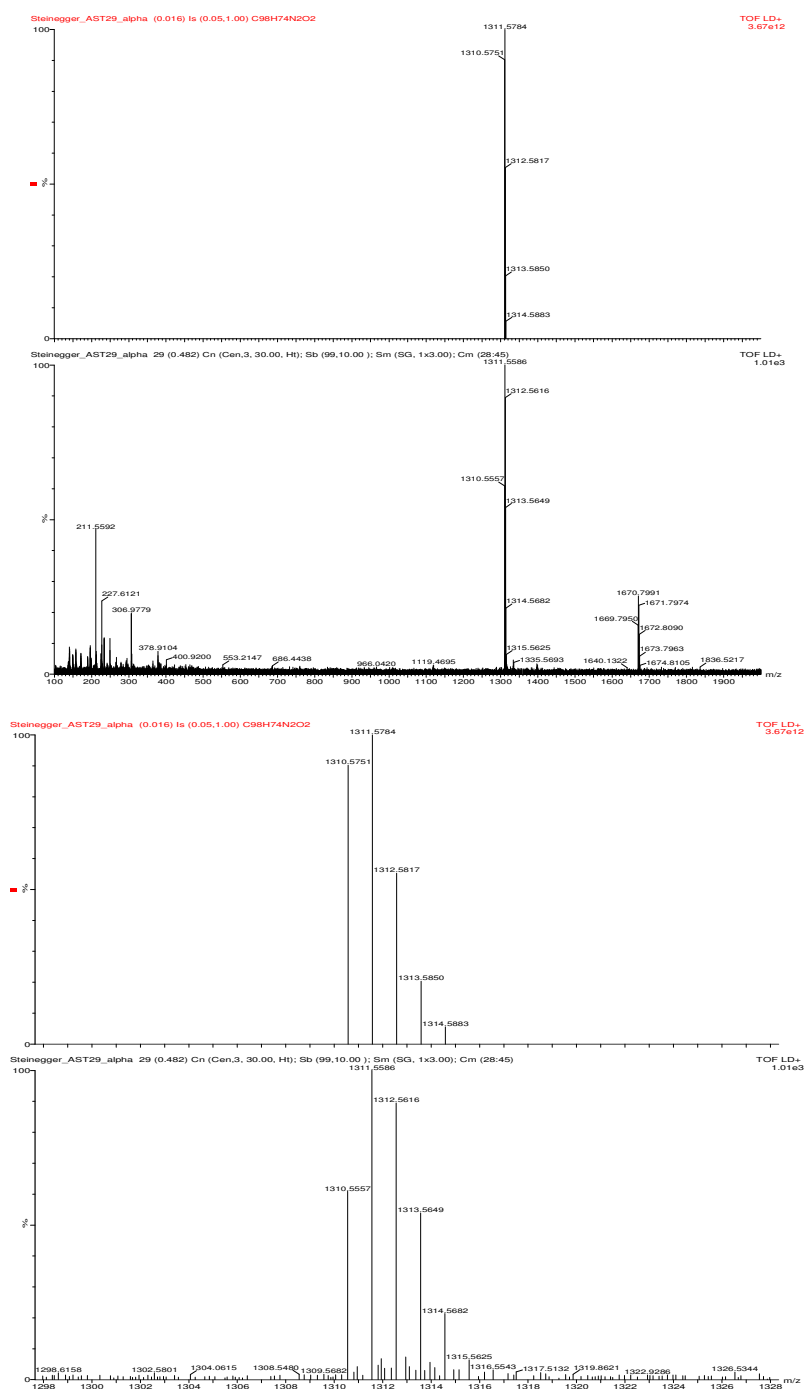
10.2.5 Compound 8

Figure 10.35: MALDI-TOF spectrum of compound **8** in an alpha matrix and the corresponding isotope pattern.
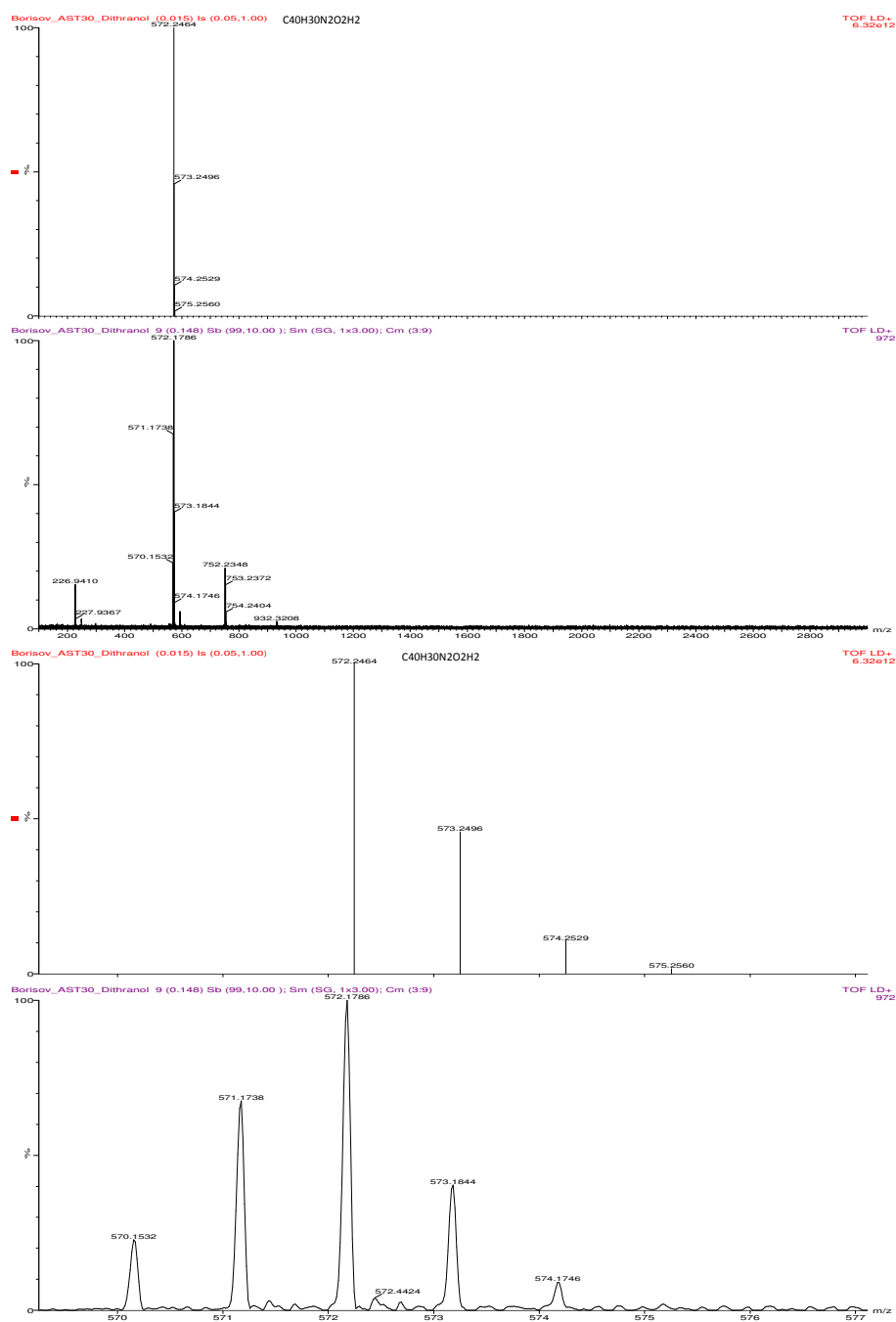
10.2.6 Compound 9

Figure 10.36: MALDI-TOF spectrum of compound **9** in a dithranol matrix and the corresponding isotope pattern.
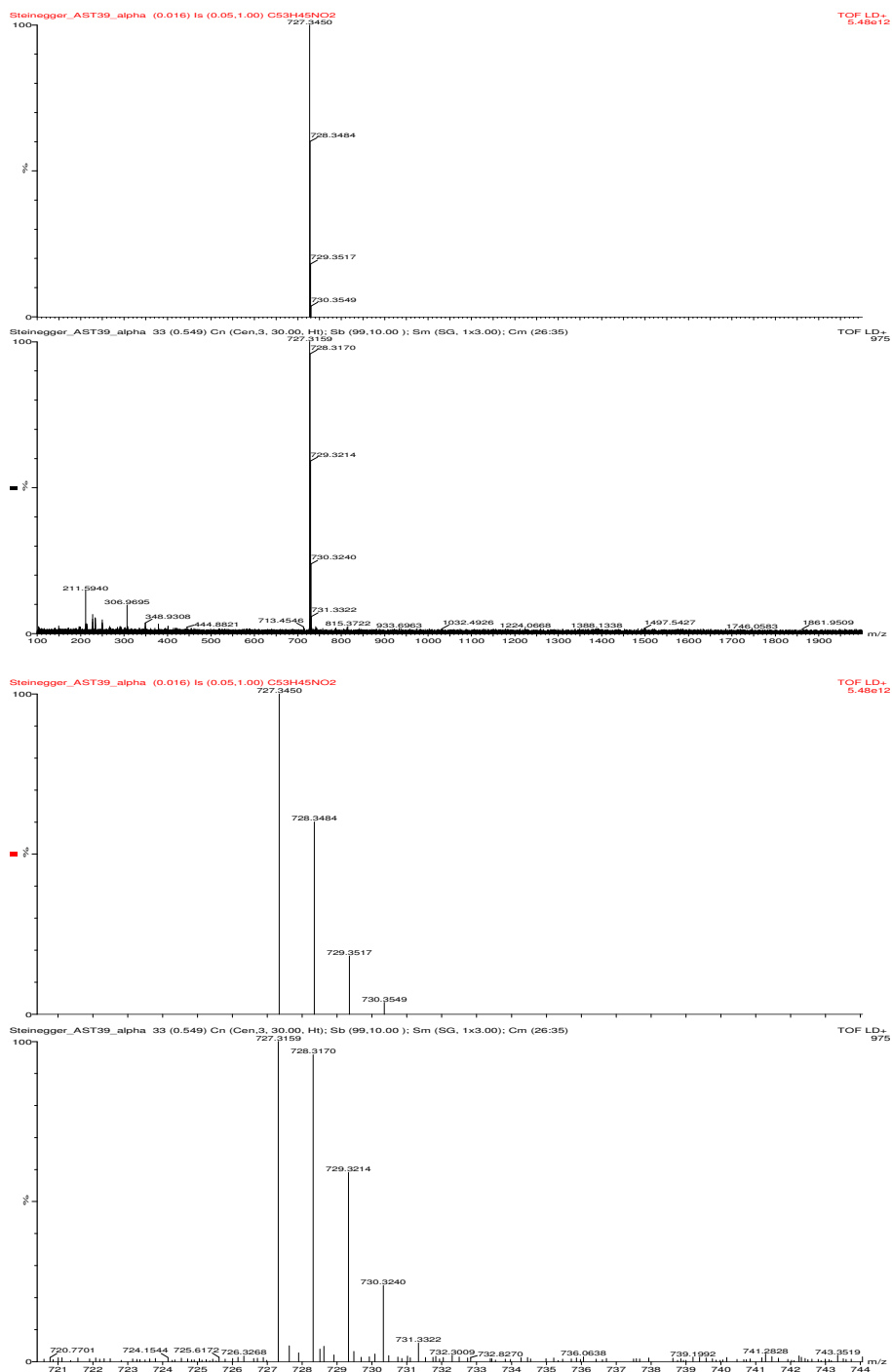
10.2.7 Compound 11

Figure 10.37: MALDI-TOF spectrum of compound **11** in an alpha matrix and the corresponding isotope pattern.
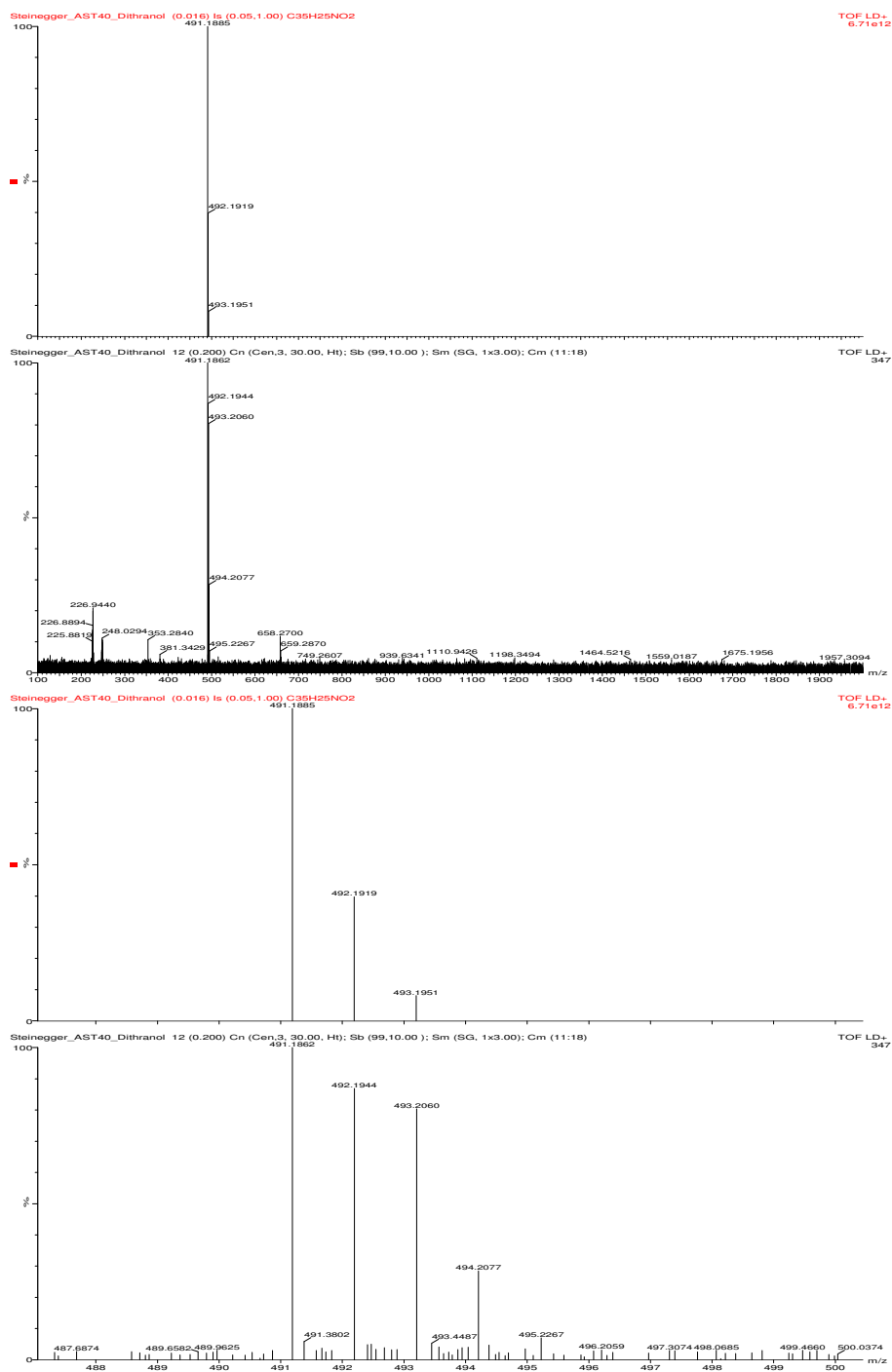
10.2.8 Compound 12

Figure 10.38: MALDI-TOF spectrum of compound **11** in a dithranol matrix and the corresponding isotope pattern.
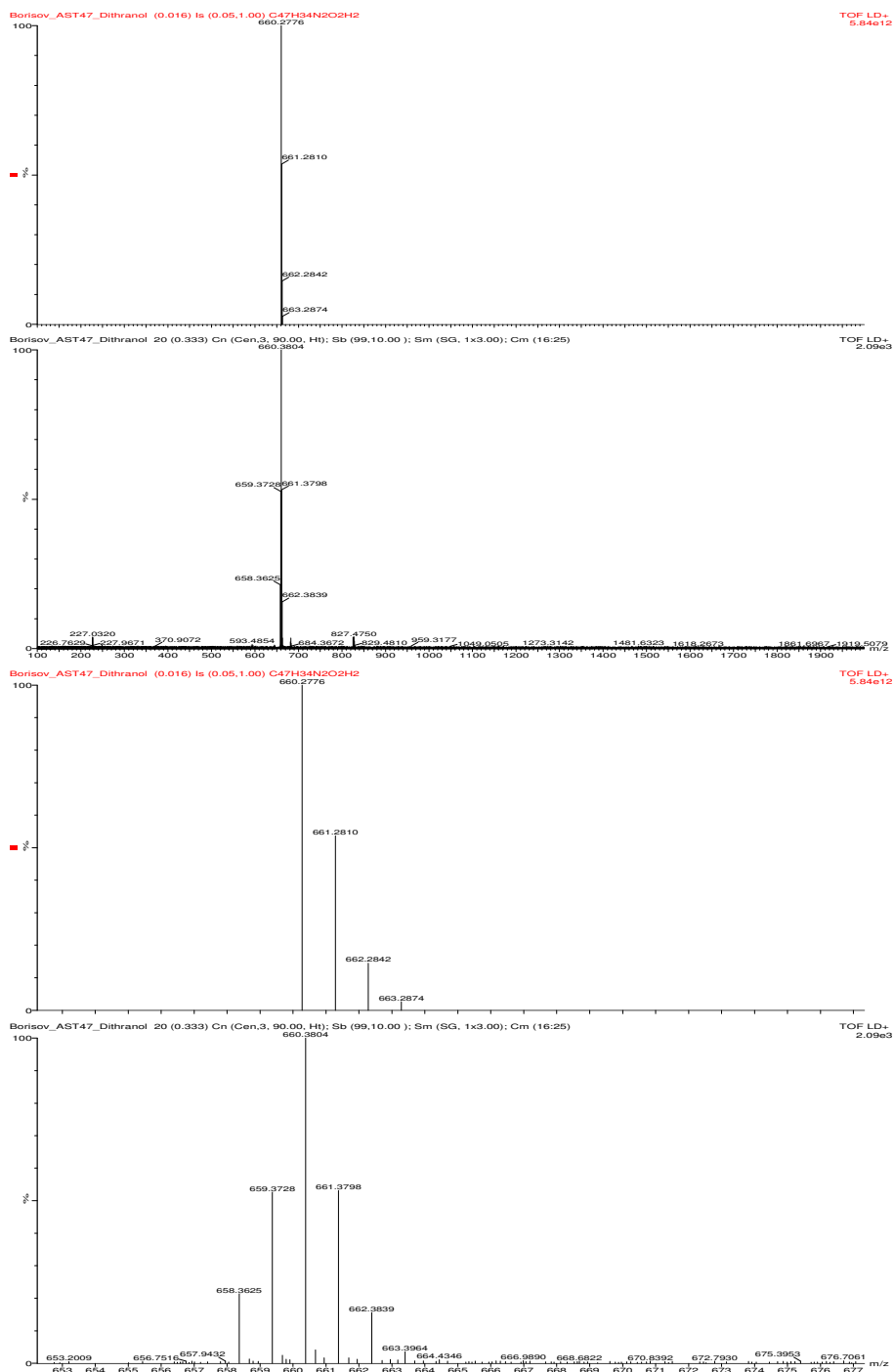
10.2.9 Compound 15

Figure 10.39: MALDI-TOF spectrum of compound **15** in a dithranol matrix and the corresponding isotope pattern.
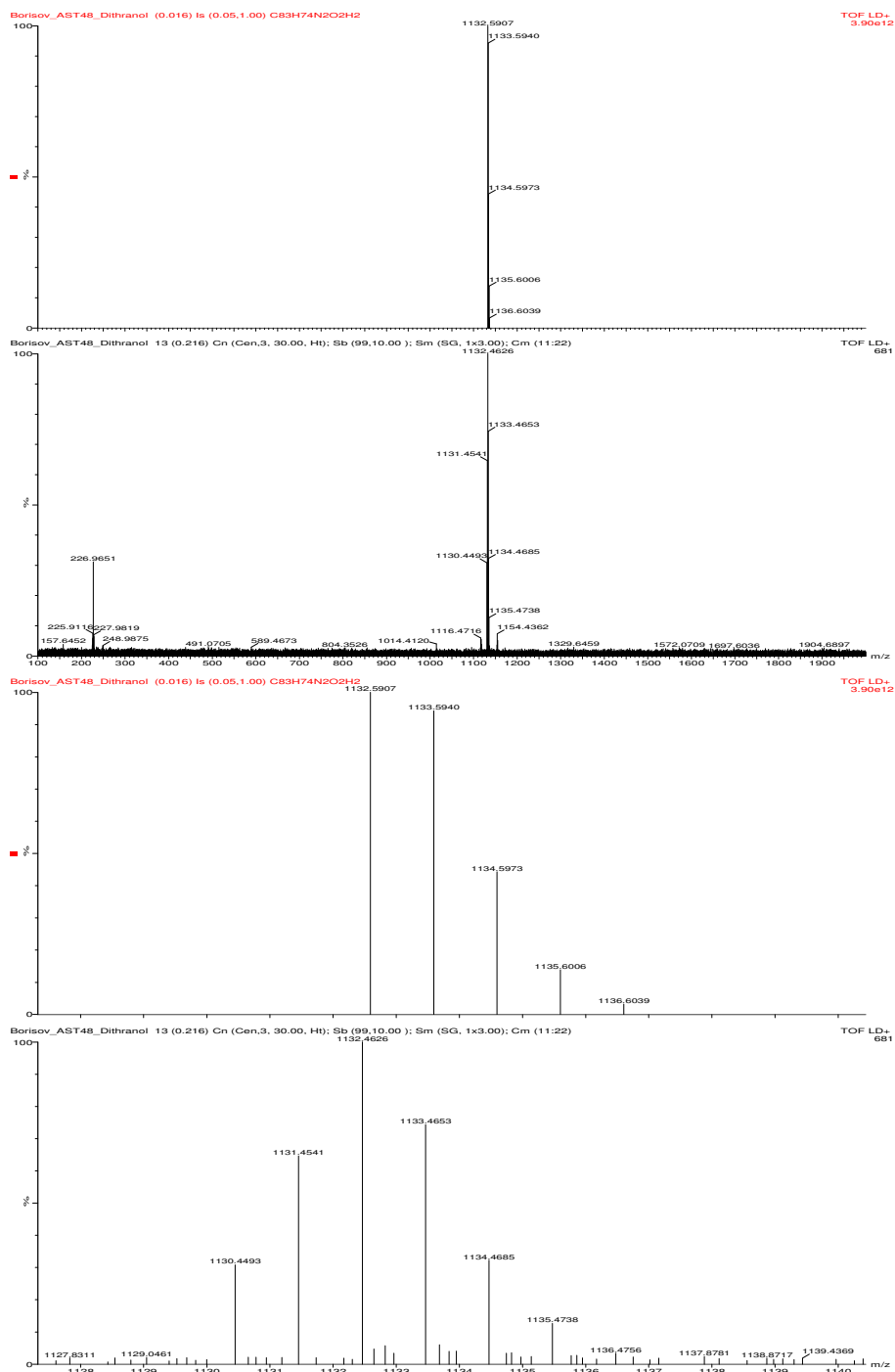
10.2.10 Compound 16

Figure 10.40: MALDI-TOF spectrum of compound **16** in a dithranol matrix and the corresponding isotope pattern.
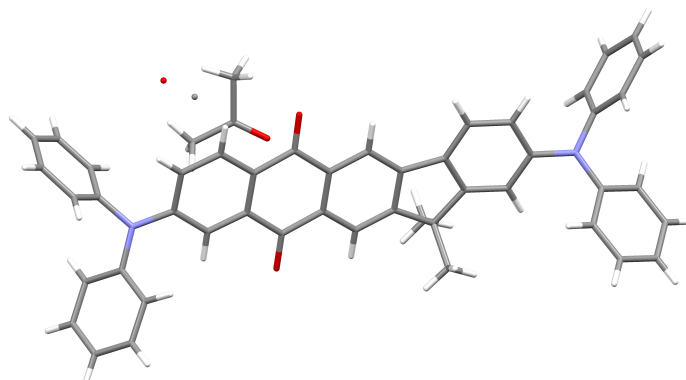
10.3 Crystal Structure and Crystallographic Data

Figure 10.41: Crystal structure of compound **15** with aceton.

Table 10.1: Crystallographic Data for Compound **15**

|	
Empirical Formula	$C_{50}H_{40}N_2O_3$
Formula Weight	716.84
Temperature	100(2) K
Wavelength	0.71073 Å
Crystal System, Space Group	triclinic, P -1
Unit Cell Dimension	a=11.1870(4) Å α=104.235(2) deg.
	b=12.5008(5) Å β=102.058(2) deg.
	c=14.3378(6) Å γ= 94.053(2) deg.
Volume	1884.82 Å^3
Z	4
Absorption Coefficient	0.078 mm^{-1}
F(000)	756
Theta Range for Data Collection	1.694 - 29.0
Limiting Indices	-15<=h<=15; -17<=k<=17; -19<=l<=19
Reflections Collected/ Unique	105926/ 9974 [R(int)=0.0668]
Completeness of Theta=29	99.7 %
Absorption Correction	SHELXL-2014/7
Goodness of Fit on F^2	1.131
Final R Indices (I $> 2\sigma$(I))	R1=0.0543, wR2=0.1279
R Indices (All Data)	R1=0.0888, wR2=0.1381

10.4 Miscellaneous
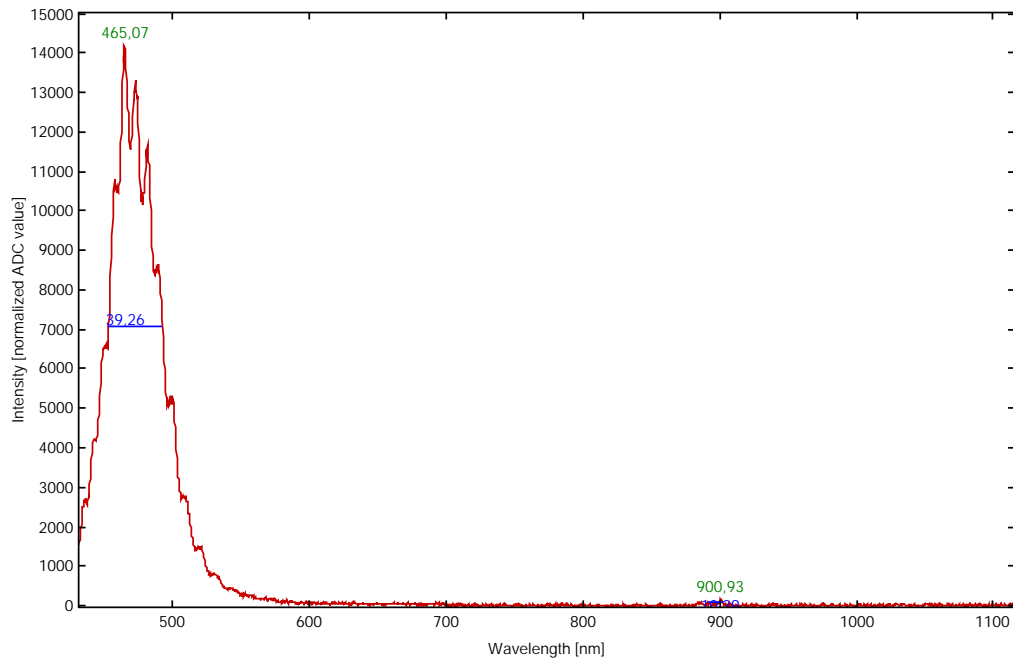
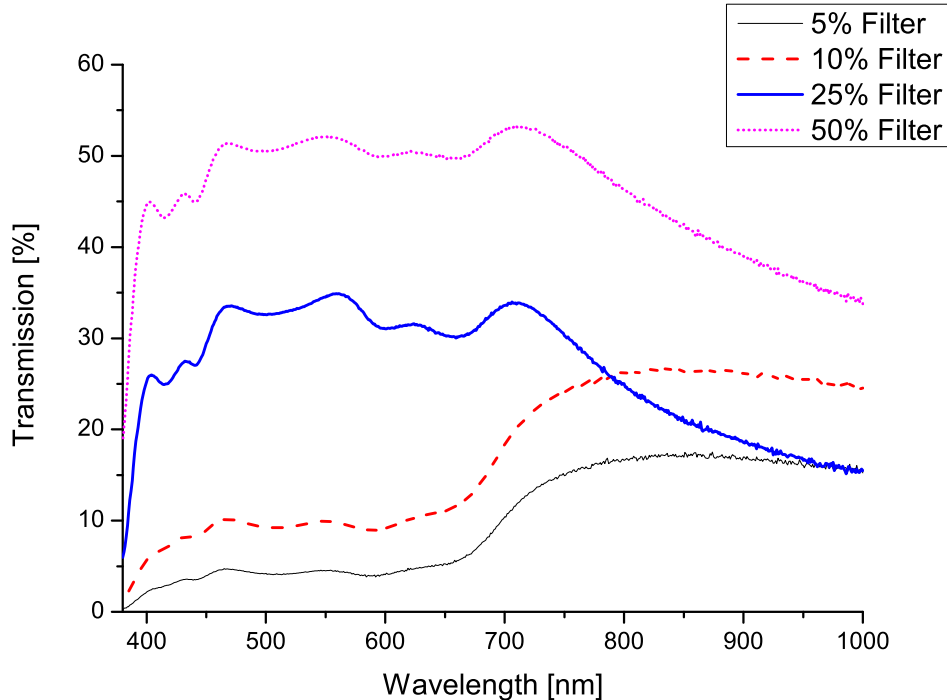**Figure 10.42:** Spectrum of the emitted light of the blue 3 LED array.

Figure 10.43: Transmission of the used neutral density filters.

AST14_PS_calib1teil3
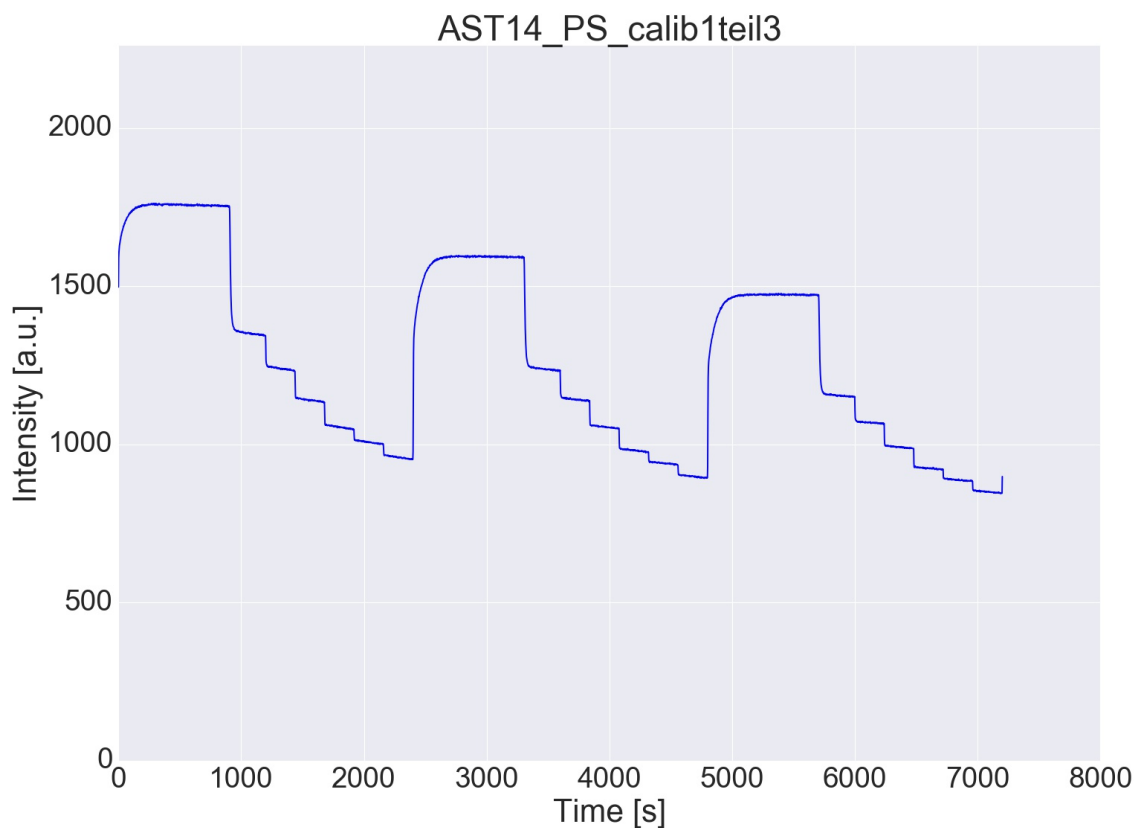
Figure 10.44: Plotted oxygen calibration for **3**.

10.5 Abbreviations

Table 10.2: List of used abbreviations

Φ	Quantum yield
AcOH	Acetic acid
av.	Average
Br-thq	2-(4-Bromophenyl)-5,6,7,8-tetrahydroquinoline
carbac	1-(9*H*-Carbazol-9-yl)-5,5-dimethylhexane-2,4-dione
CAS	Chemical Abstracts Service
CCD	Charge-coupled Device
CH	Cyclohexane
dba	Dibenzylideneacetone
dbpt	4-(4,6-Di(1*H*-indazol-1-yl)-1,3,5-triazin-2-yl)-*N,N*-diethylaniline

DCM	Dichloromethane
DME	Dimethoxyethane
DMF	Dimethylformamide
dpp	4,7-Diphenyl-1,10-phenanthroline
EE	Ethyl acetate
HOMO	Highest occupied molecular orbital
HRMS	High Resolution Mass Spectrometry
IC	Internal conversion
ISC	Intersystem crossing
K_{SV}	Stern-Volmer constant
LUMO	Lowest unoccupied molecular orbital
MALDI	Matrix-assisted laser disorption/ionization
MeOH	Methanol
MIDA	N-methyliminodiacetic acid
MO	Molecular Orbital
MS	Molecular sieve
NIR	Near infrared
NMP	N-Methyl-2-pyrrolidone
NMR	Nuclear Magnetic Resonance
NTC	Negative temperature coefficient
OLED	Organic light emitting diodes
Ormosil	Organically modified silica
PAN	Polyacrylonitrile
PDMS	Polydimethylsiloxane
PEG	Poly(ethylene glycol)
PEPPSI-Ipr cat	[1,3-Bis(2,6-Diisopropylphenyl)imidazol-2-ylidene](3-chloropyridyl)palladium(II) dichloride
PET	Polyethylene terephthalate
PMMA	Poly(methyl metacrylate)
ppy	2-Phenylpyridine
PS	Polystyrene
PTC	Positive temperature coefficient
PtTFPP	Platinum(II) tetrakis(pentafluorophenyl)porphyrin
PtTPTBP	Platinum(II) tetraphenyltetrabenzoporphyrin
PVC	Poly(vinyl chloride)
QY	Quantum yield

R. T.	Room temperature
RISC	Reverse intersystem crossing
TADF	Thermally activated delayed fluorescence
*t*Buacac	2,2,6,6-tetramethyl-3,5-heptanedione
*t*BuOH	*tert*-Butanol
THF	Tetrahydrofuran
TLC	Thin layer chromatography
TOF	Time-of-Flight
Tol	Toluene
TTA	Triplet-triplet annihilation
TTA	3-thenoyltrifluoroacetonate
UV	Ultraviolet
XPhos	2',4',6'-triisopropyl-2-dicyclohexylphosphinobiphenyl